

Department of Physics and Astronomy

University of Heidelberg

Master thesis

in Physics

submitted by

Benedikt Herkommer

born in Mutlangen

2019

Measuring the energy spectra of unknown samples using coherent control of the complex phase of X-rays

This Master thesis has been carried out by
Benedikt Herkommer

at the
Max-Planck Institut for Nuclear Physics, Heidelberg

under the supervision of
apl. Prof. Dr. Jörg Evers

Messung der Energiespektren von unbekanntem Proben durch die kohärente Kontrolle der komplexen Phase von Röntgenstrahlen:

Das Feld der Quantenoptik beschreibt die Wechselwirkung von Materie mit elektromagnetischer Strahlung, wobei beide quantisiert beschrieben werden. Bisher beschränkten sich die verwendeten Frequenzen der Strahlung auf den Arbeitsbereich von Lasern, also von Mikrowellen bis hin zum UV-Bereich. Durch die Verfügbarkeit von neuen Strahlungsquellen wie Synchrotrons, konnte das Feld der Röntgen-Quantenoptik begründet werden. Durch die höhere Energie der Röntgenstrahlen ergeben sich neue Möglichkeiten. Zum Beispiel kann die Wechselwirkung des Kerns eines Atoms mit elektromagnetischer-Strahlung untersucht werden. Aufgrund von verschiedenen Beschränkungen der Strahlungsquellen ist es nicht möglich die Methoden zur Kontrolle und Messung der Wechselwirkung direkt in den höheren Frequenzbereich zu übertragen. Eine Möglichkeit diese Beschränkungen zu umgehen besteht darin, eine zusätzliche Phase bei Nuklearer vorwärts Streuung zu nutzen, welche durch mechanische Bewegung resonanter Proben erzeugt wird. In dieser Arbeit wird das Potential von oszillierenden resonanten Proben theoretisch untersucht. Der Phasen-Offset der Oszillation stellt dabei einen zusätzlichen und kontrollierbarer Freiheitsgrad dar, der die Zeit-, und Energiespektren von gestreuten Wellenpaketen beeinflusst. Ein Problem, welches sich durch die hohe Energie der Strahlung ergibt, sind fehlende Methoden zur Messung der Energiespektren. Um das zu lösen, wird eine neue Methode entwickelt, die den Phasen-Offset nutzt um das Energiespektrum und die komplexe Phase einer Probe zu messen.

Measuring the energy spectra of unknown samples using coherent control of the complex phase of X-rays:

The field of quantum optics describes the interaction of electromagnetic radiation with matter whereby both are described quantum mechanically. So far the used frequencies of the radiation, were restricted to the operation range of lasers, which is between microwave to ultraviolet radiation. With the availability of new radiation sources such as synchrotrons, the field of X-ray quantum optics could be established. The high energy of the X-rays offer new possibilities, such as the examination of the interaction of radiation the nuclei of atoms. Unfortunately, X-ray source limitations still prohibit the direct transfer of control or detection schemes. One approach to overcome such limitations are mechanical motions of resonant absorber, which induces an additional phase at nuclear forward scattering. In this thesis the use of oscillating resonant absorber is examined theoretically. The phase offset of the oscillation offers an additional and controllable degree of freedom, which influences the time and energy spectrum of a scattered wave packet. One problem occurring due to the high energy, is the lack of methods to measure the energy spectrum. To solve this problem, a new approach is developed, using the phase offset to measure the energy spectrum and the complex phase in the energy domain.

Contents

1. Introduction	1
1.1. Motivation	1
1.2. Outline of this Thesis	3
2. Basic Theoretical Background	5
2.1. Nuclear Forward Scattering	6
2.1.1. Classical Derivation	6
2.1.2. Quantum Mechanical Effects	11
2.1.3. Nuclear Forward Scattering in The Time Domain	13
2.1.4. Response of Separated Samples In a Row	14
2.2. Phase Manipulation via Mechanical Motion	17
2.2.1. Basic Principle	17
2.2.2. Mathematical Formalism for an Arbitrary Motion	18
2.2.3. Step Function: Instant Phase Shift	21
2.2.4. Oscillations: Generation of sidebands	23
2.3. Approximation For Thin Foils	26
3. Theoretical Examination of φ_0	27
3.1. Effect of Mechanical Motion in the Time Domain	27
3.1.1. Instant Phase Shift	27
3.1.2. Oscillating foil	31
3.2. Influence of φ_0 in the Energy Domain	33
4. Determination of Energy Spectrum And Phase Using φ_0	37
4.1. Theoretical Model	39
4.1.1. Sensing Head Approximation	43
4.1.2. Single Sideband Approximation	44
4.1.3. Full System	48
4.2. Numerical Implementation	57
4.2.1. Numerical Implementation of the ν -space Filter	58
4.2.2. Spectral Intensity and Phase Reconstruction from the fit algorithm	60
4.3. Example Calculations	65

5. Evaluation Of the Oscillation Drive	71
5.1. Metrics and Averaging Time Intervals	72
5.1.1. Different Metrics for Performance Evaluation	72
5.1.2. Determination of the Average Time Interval	74
5.2. Evaluation for Exemplary Targets	75
5.2.1. Parameter Analysis	75
5.2.2. Special Case: Average Time Interval via Symmetry and Edge Criteria	80
5.2.3. Conclusions from the Parameter Analysis	86
5.3. Comparison of the Oscillation-drive with the Doppler-drive	87
5.3.1. Short Theory of Late Time Integration with Doppler-drive	88
5.3.2. Evaluation Using the Metrics	89
5.4. Theoretical Optimum of the Doppler-drive: Convolution Theorem	95
5.4.1. Comparison with the Oscillation-drive	101
5.5. Evaluation of the Phase	106
5.6. Summary of the Oscillation-drive	107
6. Summary and Outlook	111
A. Additional plots to chapter 5	115
Bibliography	119
Acknowledgment	125

1. Introduction

1.1. Motivation

The interaction of light, or electromagnetic radiation in general, with matter is a wide field in modern physics. To explain the spectrum of blackbody radiation Planck, described electromagnetic radiation as discrete units of energy. The theoretical description of the photoelectric effect by Einstein [1], using light quanta or photons, could explain and describe the observed effects correctly. The investigation of quantized light with matter finally lead to the field of quantum optics [2–4]. This lead to new descriptions of light, like coherent states [5]. They have been used to develop new theories of photon statistic e.g. photon antibunching [3], and further led to the discovery of squeezed light [4]. This was used to theoretical describe new phenomena and prove them experimentally, like electromagnetic induced transparency [6], single photon added coherent states [7] or the “Hanbury Brown - Twiss” effect, which uses photon correlation methods for e.g. astronomical observations [8]. These discoveries have been used for state of the art research. Electromagnetic induced transparency can be used for laser cooling of trapped ions [9], squeezed states can be used to improve interferometric measurements, as needed for the detection of gravitational waves [10].

Quantum optics has tremendously profited from the development of new light sources. Especially the advancement in laser technology, providing highly coherent and monochromatic light, which is necessary for many applications, has enabled much fundamental and technological progress. Common laser sources providing wavelength ranging from microwaves to infrared and the visible light range to ultraviolet. To extend the field of quantum optic to higher energy ranges, light sources with comparable properties like laser light, but with higher energies are needed.

Radiation generated by the actual generation of synchrotron facilities [11], can partially fulfill this need, as it has a high intensity, is highly coherent and collimated. Even though, there has been a lot of progress in developing X-ray sources, they have several disadvantages compared to laser radiation.

The pulse length of a typical synchrotron pulse is on the order of 60 – 100 ps [12], which is quite short compared to the lifetime of typical transitions considered in nuclear quantum optics. Therefore, it is not possible to irradiate samples continuously. An

other consequence of the short light pulse is that the light is quite broad in the energy domain.

To extend the field of quantum optics to hard X-ray domain, the methods and know-how of the lower energy range can not just be ported to the new range which is, inter alia, due to the properties of synchrotron radiation mentioned above. Therefore new methods have been and are still under development to establish the field of X-ray quantum optics [13].

A major difference in the interaction of light with matter of X-rays compared to a lower energy range, is their ability to interact not only with the shell electrons but also with the inner electrons and even with the nuclei of the atoms.

If the interaction of nuclei with X-rays is examined, the “Mössbauer-effect” have to be considered. Discovered by Rudolf Mössbauer [14], it describes the recoilless absorption and emittance of γ -radiations by atomic nuclei bound in a solid. Usually when a nucleus emits or absorbs a γ -photon, it experiences a recoil which normally leads to a broadening of the linewidth of the radiation, due to the Doppler-effect. The Mössbauer effect causes the momentum of the recoil to be delivered to the lattice of a surrounding solid the nucleus is bound to. Due to its heavy mass, the solid can absorb the momentum and the emittance and absorption, respectively, is recoil free, which leads to a narrow linewidth at high frequencies.

This offers a great platform for spectroscopy, because it allows to measure small changes of nuclear transitions, like isomer shifts [15] or magnetic splitting [16]. Further high precision measurements can be made, like the measurement of the gravitational red shift [17–19].

A further usecase of Mössbauer nuclei is that they offer, in combination with synchrotron radiation, a ideal platform for X-ray quantum optics. The most used material for quantum optical experiments with X-rays is the iron isotope ^{57}Fe , which has a transition energy of $\hbar\omega_0 = 14.4 \text{ keV}$ and a linewidth of $\hbar\gamma = 4.7 \text{ neV}$. Examples of successful experiments with using this in a quantum optical context are single photon storage [20], single photon superradiance and the measurement of the collective Lamb-shift [21], realizing electromagnetic induced transparency [22], interferometric phase measurement via fano resonance control [23] or coherent control of the waveform in time domain [24], as well as in frequency domain [25].

Especially the last two are of particular interest in the context of this thesis. Both are using forward scattering of thin foils of ^{57}Fe irradiated by synchrotron radiation [25] or a radioactive source [24]. Both have in common, that they use mechanical movement of the ^{57}Fe -foil, induced by a piezoelectric transducer, to add an additional phase to the forward scattered signal. The movement patterns are either an instantaneous jump (in [25]) or a harmonic oscillation (in [24]). In this thesis the potential of oscillating samples irradiated with synchrotron radiation is examined.

The main presents a solution to an other problem arising from the high energies of X-rays: There is a lack of reliable and flexible methods to measure the energy spectrum of a target. Known instruments from the visible range like gratings can in principle work at such a high energy, however, they are not able to resolve the linewidth of Mössbauer-nuclei. However, there are approaches for the measurement of the spectrum like the use of a narrow banded sources [26, 27] or the use of an analyzer foil with a narrow line width mounted on a Doppler-drive to sample the target [21]. Unfortunately all of these methods have their disadvantages, therefore, the need for precise, flexible and direct methods to measure the energy spectra of a target with a high resolution is still present.

In this thesis, the mechanical oscillations of Mössbauer-nuclei are used to develop a new method to measure the energy spectrum of an unknown target, called the “Oscillation-drive”. An oscillation is a relatively simple realizable moving pattern in an experiment. Moreover, it offers several controllable parameters like the amplitude, the frequency and a phase offset, which can be used to tune the experimental setup. These parameters, in particular the phase offset, offer an additional degree of freedom which is exploited, to get new and so far inaccessible information over an unknown target.

1.2. Outline of this Thesis

This thesis consist of six chapter. The first chapter is this introduction, which is used to give a short motivation to the topic of the thesis and give a short outline of the thesis.

The second chapter gives the theoretical background which is necessary to understand the results of this thesis. There, all relevant formulas are derived or given. The setups considered in this thesis utilize the nuclear forward scattering configuration irradiated by synchrotron radiation. Therefore the first section in this chapter addresses the question of the spectral and temporal response of a Mössbauer-foil after excitation by an incoming pulse from a synchrotron facility. To give intuitive insight to this response, the formula is developed using a simple classical derivation. However, since the scattering process is of quantum mechanical nature, effects arising from this have to be taken into account. Therefore, a short overview of the quantum mechanical effects is given. The so derived formula, describes the response function in the energy domain. To get the temporal response function, it is transformed to the time domain via a Fourier-transformation. The core method of this thesis is the use of additional phases, induced by mechanical motions. To describe the influence of these motions on the spectra, a transformation formula for an arbitrary movement is derived and applied to the motion pattern of an instant jump and an oscillation.

An important parameter of the motions for this thesis, is the amplitude of the jump φ_0 and the offset of the oscillation, denoted by φ_0 as well. The symbol redundancy is chosen on purpose due to the similar effect that these parameters have in the respective cases. The effect of this parameter is studied in the third chapter. An important result of this is that it has an influence in both, in time and in the energy domain. Moreover, the influence on the spectra in both domains can be understood. Since φ_0 can be chosen in an experiment, it can be used as an additional, controllable degree of freedom, which is able to influence the response of the foil in the energy and the time domain.

In the fourth chapter, the theoretical insight of chapter three is used to develop the “oscillation-drive”. With the setup of two foils in a row, the first mounted on an oscillating piezo, the second mounted on a Doppler-drive, it is possible to use, the phase offset φ_0 and the oscillation frequency of the piezo ω_p to measure the energy spectrum of the foil on the Doppler drive. Moreover, not only the spectrum, but also the complex phase of the foil can be measured. The principle of the Oscillation-drive is the following. The oscillation of the first foil leads to a generation of sidebands of the absorption line of the first foil. The energy of the sidebands can be changed by the variation of the oscillation frequency ω_p of the piezo. This leads to an overlap of the first sideband and the energy spectrum of the second foil in energy space. The signal of this overlap is used now to reconstruct the phase and the energy spectrum of the second foil.

In the fifth chapter the quality of the reconstruction of the Oscillation-drive are analyzed with respect to the robustness in the choice of the parameters. Further it is compared with an other, well established and in experiments commonly used method.

The sixth chapter is used to give a short summary of the thesis and to provide an outlook. In particular it is pointed out, where possible improvements can be made, especially with regard to future experiments. Further a spin of project is proposed, which can be used to increase the accuracy of the method.

2. Basic Theoretical Background

This chapter gives an outline of the basic theoretical background to understand the formalism used in this thesis. The fundamental of this thesis is the interaction of nuclei with electromagnetic radiation. In this context, Mössbauer nuclei are of particular interest, because they offer very narrow linewidth at high resonance energies, due to the recoilless absorption and emission of photons [14].

The radiation which is assumed throughout this thesis are hard X-rays pulses, with a narrow linewidth and a short pulse duration, as typically produced by a synchrotron facility. The geometrically simplest setup of an experiment is to put the source, the sample and the detector all in a row. Consequently, the radiation which penetrates the sample, is scattered in forward direction and is measured at a detector. Therefore, this setup is called *nuclear forward scattering* (NFS) [28].

In the first section the basic formulae to describe NFS are derived. To provide a simple and intuitive access to this field, the section starts with a classical description. This is used to derive a formula, to describe the response function of a target in the energy domain irradiated by X-rays. The result of this derivation is a formula which correctly describes the dependency of the forward scattering of the radiation with respect to the frequency of the incident radiation. However, since the classical approach does not take into account the quantum mechanical nature of the core transitions, the corrections originating from quantum effects are sketched. This leads to the same formula but with a corrected factor.

Since measurements in nuclear forward scattering are mostly performed in the time domain, it is necessary to have a formula to describe the response of a target in the time domain. Therefore, the derived formula in the energy domain is transformed to the time domain using a Fourier transformation.

The core method of this thesis, is to apply mechanical motion to the sample to manipulate the spectral response function of the nuclei. Therefore in the second section, an intuitive explanation of this principle, as well as a mathematical formulation is given. Especially the case of an oscillating sample plays an important role in this thesis. Therefore, the influence of the different parameters, such as the oscillation amplitude p , the frequency ω_p and the phase offset of the oscillation of the sample φ_0 is explained in more detail. For this thesis the most important parameter is the phase offset φ_0 .

In the last chapter, a method to approximate the time response function is presented, which is useful to solve some problems where no exact solutions exist for the exact equations.

2.1. Nuclear Forward Scattering

The problem of deriving a formula describing the nuclear forward scattering can be approached using different theoretical frameworks. In the literature, possible derivations can be found using classical electrodynamics [29], quantum dynamics [30] or quantum electrodynamics [28, 31–33]. In this section a formula is derived using the classical Lorentz-Model. Even though the model is rather simple, it is used quite often to describe optical effects [34, 35]. Even more complicated effects like vacuum Rabi splitting [36], or, like in this thesis, nuclear forward scattering can be described by this model.

The derived formula has the correct dependencies of the frequency and the linewidth of the transition. This is quite impressive, because it does not take into account any quantum mechanical effects. However, a quantum mechanical description reveals, that a factor within the classically derived formula needs to be corrected. To demonstrate the origin of this correction, the quantum mechanical derivation is sketched briefly, and the corrected factor is presented.

As the derivation is based on the index of refraction, which depends on the frequency, the results from both, the classical and the quantum mechanical derivation, are intrinsically bound to the frequency space. In order to describe the scattering process in time, the derived formula is transformed to the time domain using a Fourier transformation.

2.1.1. Classical Derivation

In this section a classical dipole model is used to derive the transmission function of a sample in rest, irradiated by X-rays, in the energy domain. Starting point are Maxwell's equations. First in vacuum and later in homogeneous and isotropic media. Using this background, the Lorentz model is used to derive the frequency dependent index of refraction. With this, the propagation of a wave packet through the sample can be calculated, which yields the response function.

Basics of Electrodynamics

In Vacuum Fundamental starting point for electrodynamics are Maxwell's equations. In vacuum they are [37],

$$\nabla E = 0, \quad (2.1)$$

$$\nabla H = 0, \quad (2.2)$$

$$\nabla \times E = -\mu_0 \frac{\partial H}{\partial t}, \quad (2.3)$$

$$\nabla \times H = \epsilon_0 \frac{\partial E}{\partial t}, \quad (2.4)$$

with the electrical field E , the magnetic field H , the vacuum permittivity ϵ_0 , and the vacuum permeability μ_0 . By applying a further rotation on (2.3), using the vector identity $\nabla \times (\nabla \times E) = \nabla(\nabla E) - \nabla^2 E$, while $\nabla E = 0$ according to (2.1), and inserting (2.4), the wave equation can be obtained, which reads

$$\left(\nabla^2 - \frac{1}{c_0^2} \frac{\partial^2}{\partial t^2} \right) E = 0. \quad (2.5)$$

Here $c_0 = \frac{1}{\sqrt{\epsilon_0 \mu_0}}$ denotes the speed of light in vacuum. A set of solutions of this equation are plane waves, here written in the complex form in one dimension,

$$E(t, z) = e^{i(k_0 z - \omega t)} + c.c. . \quad (2.6)$$

Here, ω denotes the frequency of the wave, and $k_0 = \frac{\omega}{c_0}$ the corresponding wavenumber in vacuum.

In Homogeneous and Isotropic Media In a homogeneous, isotropic, and source-free medium, Maxwell's equations are modified to [37],

$$\nabla D = 0, \quad (2.7)$$

$$\nabla B = 0, \quad (2.8)$$

$$\nabla \times E = -\mu \frac{\partial H}{\partial t}, \quad (2.9)$$

$$\nabla \times H = \epsilon \frac{\partial E}{\partial t}. \quad (2.10)$$

D denotes the electric flux density and B the magnetic flux density. They are related to their respective fields via,

$$D = \epsilon E \quad (2.11)$$

$$B = \mu H. \quad (2.12)$$

2. Basic Theoretical Background

The electric permittivity ϵ and the magnetic permeability μ describe, how the material reacts to the presence of an electromagnetic field.

An electric field induces electric dipoles in a material. The strength of the dipoles is given by the polarization P ,

$$P = \epsilon_0 \chi E. \quad (2.13)$$

Here, χ denotes the electric susceptibility and is material parameter. For anisotropic, inhomogeneous materials, it is a tensor. In the one dimensional-case considered here, it reduces to a scalar. For dispersive materials it depends on the frequency of the electromagnetic field.

In materials, the electric flux can be described equally by $D = \epsilon_0 E + P$ and therefore,

$$D = \epsilon_0 E + \epsilon_0 \chi E = \underbrace{\epsilon_0(1 + \chi)}_{\epsilon} E. \quad (2.14)$$

Substituting in Maxwell's equations now D and B by (2.11) and (2.12), they become equal to the vacuum case, except ϵ and μ replace ϵ_0 and μ_0 , respectively. Therefore, the wave equation also takes the same form, except for the difference that c_0 is replaced by $c = \frac{1}{\sqrt{\epsilon\mu}}$. This defines the index of refraction n , for which follows, $n = \frac{c_0}{c} = \sqrt{\frac{\epsilon\mu}{\epsilon_0\mu_0}}$. For the most materials, $\mu = \mu_0$. Therefore the index of refraction becomes,

$$n = \sqrt{\frac{\epsilon}{\epsilon_0}} = \sqrt{1 + \chi}. \quad (2.15)$$

Finally, the plane waves become,

$$E(z, t) = e^{i(kz - \omega t)} + c.c. , \quad (2.16)$$

with the wave vector $k = \frac{\omega n}{c_0}$.

Lorentz Model

Assuming a resonant medium, the time dependent relation between the polarization P and an incident electric field can be described by [37],

$$\frac{\partial^2 P(t)}{\partial t^2} + \gamma \frac{\partial P(t)}{\partial t} + \omega_0^2 P(t) = \omega_0^2 \epsilon_0 \chi_0 E(t). \quad (2.17)$$

Here, γ denotes the damping constant, which is equal to the spectral width of the atomic transition, ω_0 is the resonance frequency, χ_0 a constant and ϵ_0 the vacuum permittivity. This equation can be derived, by describing the atoms in the medium as harmonic

oscillators, displacing a charge q , with the elastic restoring force κ . Starting from a harmonic oscillator [38], the displacement $x(t)$ of the atoms in a medium can be described by,

$$\frac{\partial^2 x(t)}{\partial t^2} + \gamma \frac{\partial x(t)}{\partial t} + \omega_0^2 x(t) = \frac{F(t)}{m}, \quad (2.18)$$

where m is the mass of the oscillator, and F an external driving force. The dipole moment of each atom is described as $d = q \cdot x$. Therefore the polarization of the material becomes $P = N \cdot d$, where N is the number of atoms in a unit volume of the material. This leads to a total polarization of $P(t) = Nqx(t)$. The driving force is caused by an electrical field and is given by $F(t) = q \cdot E(t)$. By comparing of equations (2.17) and (2.18) the value of χ_0 becomes,

$$\chi_0 = \frac{Nq^2}{m\omega_0^2\epsilon_0}. \quad (2.19)$$

To solve equation (2.17), it is transformed to frequency space, using the property of Fourier transform $\mathcal{F}[f'(t)] = i\omega\mathcal{F}[f(t)]$ [39]. In the following, a hat on a symbol will denote that it refers to the corresponding value in Fourier space, e.g. $\hat{f}(\omega) = \mathcal{F}[f(t)]$. The transformation yields,

$$\hat{P}(\omega) \cdot (-\omega^2 - i\gamma\omega + \omega_0^2) = \omega_0^2\epsilon_0\chi_0\hat{E}(\omega), \quad (2.20)$$

which can be solved for $\hat{P}(\omega)$,

$$\hat{P}(\omega) = \frac{\omega_0^2\epsilon_0\chi_0E(\omega)}{\omega_0^2 - \omega^2 - i\gamma\omega}. \quad (2.21)$$

Using (2.13), it is possible to get a expression for the susceptibility,

$$\chi(\omega) = \frac{\omega_0^2\chi_0}{\omega_0^2 - \omega^2 - i\gamma\omega}. \quad (2.22)$$

To simplify this expression the denominator is rewritten as $\omega_0^2 - \omega^2 = (\omega_0 - \omega)(\omega_0 + \omega) \approx (\omega_0 - \omega)(2\omega_0)$. This approximation is justified because of the significantly larger value of ω_0 compared to the range ω varies: For ^{57}Fe $\omega_0 = 14.4$ keV, while the variation range of ω is on the order of 100 neV; therefore $\omega/\omega_0 \approx 1$. With this, the susceptibility reads,

$$\chi(\omega) \approx \frac{\omega_0^2\chi_0}{(\omega_0 - \omega)(2\omega_0) - i\gamma} \quad (2.23)$$

$$= \frac{\omega_0^2\chi_0 \frac{1}{2\omega_0}}{\omega_0 - \omega - i\frac{\gamma}{2} \frac{\omega}{\omega_0}} \quad (2.24)$$

$$\approx \frac{\frac{1}{2}\omega_0\chi_0}{\omega_0 - \omega - i\frac{\gamma}{2}} \quad (2.25)$$

$$= \frac{\frac{Nq^2}{2m\omega_0\epsilon_0}}{\omega_0 - \omega - i\frac{\gamma}{2}}. \quad (2.26)$$

2. Basic Theoretical Background

The index of refraction is related to the susceptibility via equation (2.15), therefore it is given by,

$$n = \sqrt{1 + \chi(\omega)} \approx 1 + \frac{\chi(\omega)}{2} \approx 1 + \frac{\frac{Nq^2}{4m\omega_0\epsilon_0}}{\omega_0 - \omega - i\frac{\gamma}{2}}. \quad (2.27)$$

The refractive index depends on the frequency, which ties it intrinsically to the frequency space. The propagation of the electromagnetic wave through the medium can be described by a wave packet propagating in z -direction [40],

$$E(t, z) = \frac{1}{\sqrt{2\pi}} \int \hat{E}_0(\omega) e^{i(k(\omega)z - \omega t)} d\omega. \quad (2.28)$$

Using the dispersion relation $k = \frac{\omega}{c_0} n$, and inserting equation (2.27) for n , the wave packet becomes,

$$\begin{aligned} E(t, z) &= \frac{1}{\sqrt{2\pi}} \int \hat{E}_0(\omega) e^{i\left(\frac{\omega}{c_0}nz - \omega t\right)} d\omega \\ &= \frac{1}{\sqrt{2\pi}} \int \hat{E}_0(\omega) e^{i\left(\frac{Nq^2}{4m\epsilon_0c_0} \frac{\omega}{\omega_0 - \omega - i\frac{\gamma}{2}} z\right)} e^{-i\omega\left(t - \frac{z}{c_0}\right)} d\omega \end{aligned} \quad (2.29)$$

$$\approx \frac{1}{\sqrt{2\pi}} \int \hat{E}_0(\omega) \underbrace{e^{\frac{-ib(z)}{\omega - \omega_0 + i\frac{\gamma}{2}}}}_{\hat{R}(\omega)} e^{-i\omega t} d\omega. \quad (2.30)$$

From equation (2.29) to (2.30), the approximation $\omega/\omega_0 \approx 1$ has been used again. In equation (2.30), the abbreviation $b(z) = \frac{Nq^2z}{4m\epsilon_0c_0}$ has been used. Further, z describes the thickness of the foil. Usually, the foils in experiments using NFS have a thickness on the order of a few μm , which implies that the value of $z \ll c_0$. Therefore it is possible to set $z/c_0 \approx 0$. It is important to note that this approximation is not the same as the thin foil approximation which is derived in section 2.3.

Equation (2.30) is equal to a Fourier transformation of two functions: $\hat{E}_0(\omega)$ describes the spectral distribution of the light pulse irradiating the foil. The exponential function therefore describes the spectral response $\hat{R}(\omega)$ of the foil.

So far, the classical theory of harmonic oscillators has been used to derive a frequency dependent response function of a sample which is irradiated by electromagnetic radiation. The dependency of $\hat{R}(\omega)$ on ω , ω_0 and γ , agrees with other derivations taking into account quantum mechanical effects [30–33]. It is a quite astonishing result that it is possible to derive the right behavior from a simple, classical theory. This offers an intuitive access to the scattering process and to the dependencies of the response function on the different parameters. However not all effects are taken into account, since the quantum nature of the nuclear transitions was replaced by a classical oscillator picture. The main consequence is that the factor b has to be adjusted appropriately. In the following section to the adjustments compared to the classical derivation are summarized.

2.1.2. Quantum Mechanical Effects

To provide a full description of the scattering process, quantum mechanical effects have to be taken into account. However, this is still semi-classical, since the incident light is treated as a classical electromagnetic field. Finally, this leads to a modified factor b . Necessary effects will be summarized in the following. For a general description, a scattering matrix formalism can be used. It is described in detail in [33]. Here, a short summary is given, presenting the idea but sparing out derivations and intermediate steps.

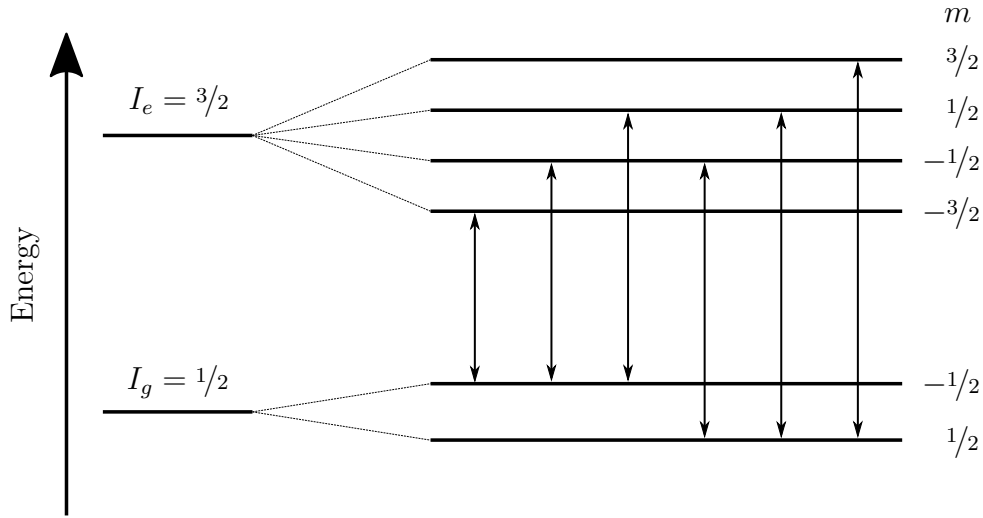


Figure 2.1.: Energy levels scheme of the core transition of ^{57}Fe . Due to the electrons there is a strong magnetic field at the position of the nucleus, leading to hyperfine splitting. For calculating the response function of nuclear scattering, the different transitions have to be taken into account. The allowed transitions are indicated. For the calculation of the response function, each is weighted by the Clebsch-Gordan coefficient, measuring its relative strength.

Again, the main idea is to use the index of refraction, to describe the scattering process. In the most general way it can be written as [41],

$$\mathbf{n} = 1 + \frac{2\pi}{k_0^2} \sum_i \rho_i \mathbf{M}_i. \quad (2.31)$$

Here, k_0 denotes the wavenumber of the radiation. The sum accounts for all atoms in the sample, where ρ_i is the number density of the atoms and \mathbf{M}_i the scattering length of the i -th atom. The bold letters indicate, that the values are matrices. This is necessary because in general, the index of refraction depends on the direction of the incidence of the radiation on the sample.

2. Basic Theoretical Background

For this derivation the sample is assumed to be homogeneous. As a consequence, the matrices simplify to scalars. The scattering length can be split into an electronic, $E(\omega)$, and a nuclear part $N(\omega)$. Within the scope of this thesis, the electronic part is not of interest, and therefore it is denoted by $\delta + i\beta$. With this the index of refraction reads,

$$n = 1 + \delta + i\beta + \rho N(\omega). \quad (2.32)$$

For $N(\omega)$ the energy levels of the core have to be considered. In this thesis the configuration of ^{57}Fe is taken exemplary which is sketched in figure 2.1. The transition from core spin $I_g = \frac{1}{2}$ to $I_e = \frac{3}{2}$ has a energy of 14.4 keV. Due to the electrons, there is a strong magnetic field at the position of the nucleus. This leads to a hyperfine splitting, due to the Zeeman-effect [42]. An expression for $N(\omega)$ can be derived from quantum scattering theory [43]. The principal steps and dependencies of the formula are described in the following briefly.

- For a dipole, the sum over all allowed transitions is taken. Each transition is weighted with a spherical harmonic and the Clebsch-Gordon coefficient. The coefficients are used to take the relative strength of each transition into account.
- The whole sum is weighted with the Lamb-Mössbauer factor f_{LM} . It describes the ratio of recoil-free transitions to the total number of transitions in a Mössbauer nucleus.
- Another important factor is the internal conversion α . It describes the transfer of energy from the nucleus in an excited state to an shell electron. This is possible due to the nonzero probability to find an electron within the nucleus.

For the special case of ^{57}Fe in a stainless steel foil only one transition is driven. In this case, the index of refraction becomes [21, 33, 44, 45],

$$n = 1 - \delta + i\beta - 2\pi \frac{\rho_N}{k_0^3} \frac{f_{\text{LM}}}{2(\alpha + 1)} \frac{2I_e + 1}{2I_g + 1} \frac{\gamma}{2} \frac{1}{\omega - \omega_0 + i\frac{\gamma}{2}}, \quad (2.33)$$

with nuclear density $\rho_N = 83.18 \text{ nm}^{-3}$, the wave vector of the transition $k_0 = 73.039 \frac{1}{\text{nm}}$, the Lamb-Mössbauer factor $f_{\text{LM}} \approx 0.8$, the factor of internal conversion $\alpha = 8.56$, $I_e = \frac{3}{2}$, $I_g = \frac{1}{2}$ are the spin of the excited and ground state, respectively, the transition width $\gamma = \frac{4.7}{\hbar} \text{ neV}$ and the transition energy $\omega_0 = \frac{14.4}{\hbar} \text{ keV}$. δ and β describe the contribution of the electrons to the index of refraction. To obtain a formula describing exclusively the interaction of the X-rays with the cores, the electronic contributions are neglected in the following. In reality the electronic contribution leads to a small amount of absorption [25].

Inserting equation (2.33) now in (2.28) yields,

$$\hat{R}(\Delta) = \exp\left(\frac{-ib(z)}{\Delta + \frac{i\gamma}{2}}\right), \quad (2.34)$$

with,

$$b(z) = \frac{\pi \rho_N f_{LM} \gamma z}{k_0^2 (\alpha + 1)}. \quad (2.35)$$

$\hat{R}(\Delta)$ describes the spectral response of a target to a broad banded excitation. $b(z)$ is a number, depending on the material and the driven transitions and on the thickness z of the target. For this $k_0 = \frac{\omega_0}{c_0}$ and the approximation that $\frac{\omega}{\omega_0} \approx 1$ have been used. Here the detuning $\Delta = \omega - \omega_0$ has been introduced. This notation will be used in the rest of the thesis for all expressions in the energy domain.

Equation (2.34) is plotted in figure 2.2a in dependence of different values of γ and b . The energy axis is scaled in units of the linewidth of ^{57}Fe which is $\gamma = 4.7$ neV. This scaling will be used for all other plots in the energy domain in this thesis. $b(z)$ depends on the material of the sample, but in particular on the thickness of the material. Therefore, assuming the same material, b describes the thickness of the material. In the energy domain it has two influences. First, it describes the absorption strength. If the absorption exceeds the point where the intensity becomes zero, it leads to a broadening of the dip and an increasing range of zero intensity. $1/\gamma$ describes the lifetime of the state. In the energy domain γ determines the linewidth of the absorption dip.

2.1.3. Nuclear Forward Scattering in The Time Domain

To determine the time response of a single line resonance foil, equation (2.34) has to be transformed to the time domain by calculating the inverse Fourier transformation. Therefore the integral which has to be calculated is,

$$R(t) = \frac{1}{\sqrt{2\pi}} \int_{-\infty}^{\infty} e^{\frac{-ib}{\omega - \omega_0 + \frac{i\gamma}{2}}} e^{-i\omega t} d\omega. \quad (2.36)$$

This is not solvable directly, therefore some intermediate steps have to be performed. First, the exponential function is written in its series representation, and the first summand is separated,

$$\begin{aligned} R(t) &= \frac{1}{\sqrt{2\pi}} \int_{-\infty}^{\infty} \sum_{n=0}^{\infty} \frac{1}{n!} \left(\frac{-ib}{\omega - \omega_0 + \frac{i\gamma}{2}} \right)^n e^{-i\omega t} d\omega \\ &= \frac{1}{\sqrt{2\pi}} \int_{-\infty}^{\infty} \left[1 + \sum_{n=1}^{\infty} \frac{1}{n!} \left(\frac{-ib}{\omega - \omega_0 + \frac{i\gamma}{2}} \right)^n \right] e^{-i\omega t} d\omega \\ &= \frac{1}{\sqrt{2\pi}} \int_{-\infty}^{\infty} 1 e^{-i\omega t} d\omega + \frac{1}{\sqrt{2\pi}} \sum_{n=1}^{\infty} \frac{(-ib)^n}{n!} \int_{-\infty}^{\infty} \frac{e^{-i\omega t}}{\left(\omega - \omega_0 + \frac{i\gamma}{2} \right)^n} d\omega. \end{aligned} \quad (2.37)$$

The first part is simply the integral representation of the δ -function. Therefore its result is $\sqrt{2\pi}\delta(t)$. The integral in the second part can be calculated using Cauchy's integral formula [46]. For this, the integral has to be expanded to the complex plane. There, a path integral in the lower half plane is performed, such that the pole is enclosed. This allows to use,

$$\oint_C \frac{f(z)}{(z - z_0)^n} dz = \frac{-2\pi i}{(n - 1)!} f^{(n-1)}(z_0). \quad (2.38)$$

Here $f(z) \hat{=} e^{i\omega t}$, $z \hat{=} \omega$ and therefore $z_0 \hat{=} \omega_0 - \frac{i\gamma}{2}$. The parenthesis with $(n - 1)$ in the exponent of f denote the $(n - 1)$ th derivation. With the n -th derivative, $f^{(n)} = (-it)^n e^{-i\omega t}$, the second part of equation (2.37) becomes,

$$\begin{aligned} & \frac{1}{\sqrt{2\pi}} \sum_{n=1}^{\infty} \frac{(-ib)^n - 2\pi i (-it)^{n-1}}{n! (n-1)!} e^{-(\omega_0 - i\frac{\gamma}{2})t} \theta(t) \\ &= -\sqrt{2\pi} \sum_{n=0}^{\infty} \frac{(-1)^n}{n!(n+1)!} \left(\frac{2\sqrt{bt}}{2} \right)^{2n+1} \frac{b}{\sqrt{tb}} e^{-i\omega_0 t} \theta(t) e^{-\frac{\gamma}{2}t}. \end{aligned} \quad (2.39)$$

The second line was written so as to be able to use the first-order Bessel function of the first kind,

$$J_1(x) = \sum_{n=0}^{\infty} \frac{(-1)^n}{n!(n+1)!} \left(\frac{x}{2} \right)^{2n+1}. \quad (2.40)$$

Using this, the whole integral (2.37) becomes,

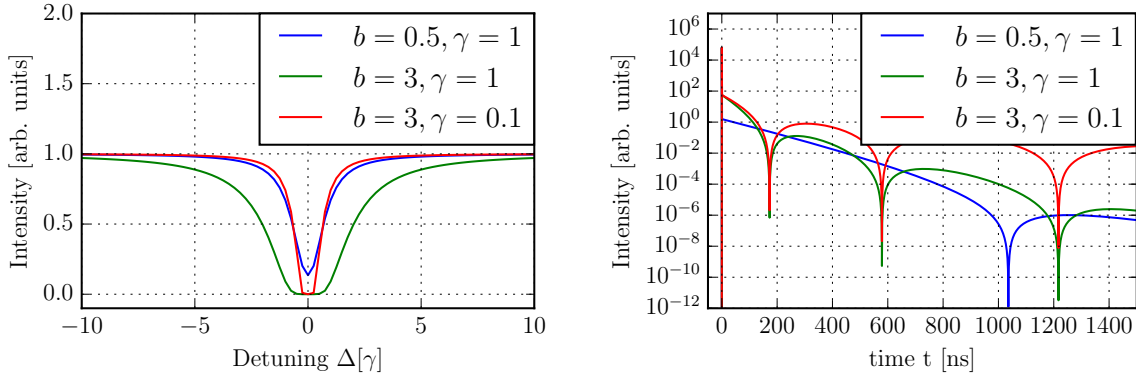
$$R(t) = \sqrt{2\pi}\delta(t) - \sqrt{\frac{2\pi b}{t}} J_1(2\sqrt{bt}) \theta(t) e^{-i\omega_0 t} e^{-\frac{\gamma}{2}t} \quad (2.41)$$

This is a quite interesting result. The physical interpretation of this is that the radiation scattered by the sample is split into two parts. The first part penetrates the sample without resonant scattering at the nuclei, which is represented by the δ -function. This will be called the prompt part in the following. The second part scatters resonantly with the nuclei which leads to a delay in time.

Equation (2.41) is plotted in figure 2.2b in dependence of different values of γ and b . The position of the minima depends on b and therefore on the thickness of the foil. The rate with which the signal intensity decreases depends on γ .

2.1.4. Response of Separated Samples In a Row

So far the response function of one sample has been calculated. In the following the analysis will be extended to a linear sequential arrangement of two foils.



(a) Energy spectrum of a single resonance line foil with different parameters. γ refers to the linewidth of ^{57}Fe , i.e. $\hbar\gamma = 4.7$ neV. (b) Time spectrum of a single line resonance line for different values of b and γ .

Figure 2.2.: Energy and time spectrum for a single resonance line foil for different values of b and γ . The parameter b depends on the material and especially on the thickness of the foil. Therefore, assuming the same material, b represents the thickness. In the energy domain it has two influences. First it describes the absorption strength. If it exceeds the point where the intensity becomes zero, it leads to a broadening and an increasing interval of zero intensity (compare with the green curve). In the time domain, b determines the position of the minima. γ , describes the lifetime of the transition. Therefore, in the energy domain, it determines the width of the dip. In the time domain, it is responsible for the rate with which the signal decreases.

Furthermore, in this section, short analysis of the temporal sequence of the scattering process will be carried out. This is important to obtain a better understanding and intuition of processes explained later, such as the influence of the phase induced by mechanical motion.

For two samples in a linear arrangement, their responses in the time domain are described by,

$$R_i(t) = \delta(t) + R_i^S(t), \quad i = 1, 2. \quad (2.42)$$

This is the same form as the response function (2.41) derived in section 2.1.3. $R_i^S(t)$ describes the resonantly scattered part. The time response of both targets is then cal-

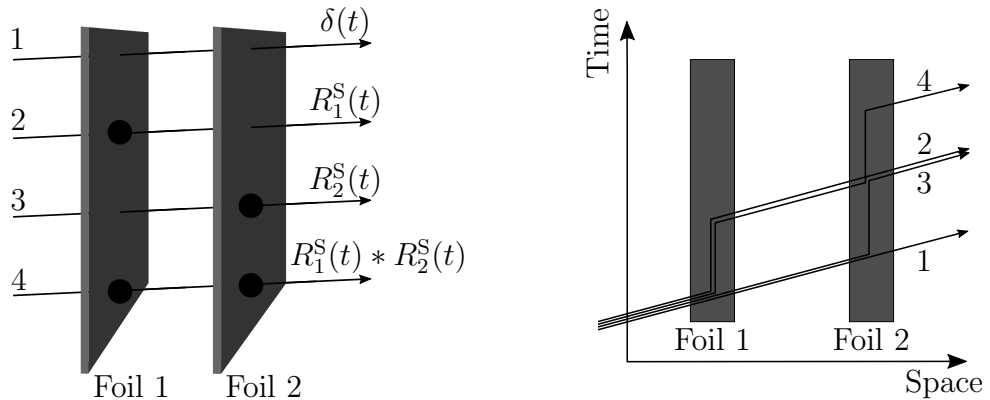
2. Basic Theoretical Background

culated via a convolution of both contributions [28],

$$\begin{aligned}
 R^{\text{tot}}(t) &= \int_0^\infty R_1(\tau)R_2(t - \tau)d\tau \\
 &= \int_0^\infty [\delta(\tau) + R_1^{\text{S}}(\tau)] [\delta(t - \tau) + R_1^{\text{S}}(t - \tau)] d\tau \\
 &= \delta(t) + R_1(t) + R_2(t) + \int_0^\infty R_1^{\text{S}}(\tau)R_2^{\text{S}}(t - \tau)d\tau.
 \end{aligned} \tag{2.43}$$

The physical interpretation of this is, that there are four different scattering paths. They are depicted in figure 2.3. The first path, referring to the δ -function, describes the part, which has not been scattered resonantly at neither the first nor the second sample. The next two parts describe the radiation scattered at only one of the samples. The last part, represented by the convolution integral, describes the radiative coupling of both samples. Each scattering process delays the photon by a certain amount of time.

Often, the calculation of the convolution is quite difficult. Therefore, one make use of the convolution theorem [39], stating that the convolution in the time domain turns to a simple multiplication in the energy space.



(a) Different scattering paths of the single parts in equation (2.43). The dots on the foils indicate resonant scattering. (b) Sketched space-time diagram of the different scattering paths. The scattered photons are delayed by a certain time amount

Figure 2.3.: Depicted scattering paths of two foils. The formulae refer to equation (2.43). In (a) is depicted which path scatters at which foil. In (b) the different paths in a space-time diagram are sketched. Each scattering process delays the photon by a certain amount of time. If the radiation scatters at both foils, it is called radiatively coupled. The signal is resulting from the sum of all paths. This picture can be found similar in [28].

For the derivation of function (2.34) and (2.41), for the incident X-Rays, the assumption has been made that the incident X-rays are δ -peaks in the time domain and therefore unity in the energy domain. This is due to the convolution theorem.

2.2. Phase Manipulation via Mechanical Motion

In the past the effects on moving targets have been studied experimentally and theoretically. By performing an almost instant displacement of the target it is possible to generate a radiation burst in the time domain, called “gamma echo” [47], as well as in the energy domain [25]. By oscillations of the target, it is possible to perturb nuclear excitons [48], to radiatively couple and decouple the targets [49] or to control the waveform in the time domain [24].

There have been several examples how to calculate the transmission of a moving foil, e.g. [24, 25, 50]. Furthermore, a general framework has been developed for calculating the response spectra of arbitrarily moving targets after interacting with X-ray radiation [51].

In this section a general formula will be derived describing the response of a target moving with an arbitrary motion $\Delta z(t)$ for the interaction with a synchrotron X-ray pulse.

First, an intuitive explanation of the principle of the phase manipulation via mechanical motion is given. This is supported by a mathematical formula which is derived. After this, the formula is used to calculate two motion patterns, which will be important for the rest of the thesis.

2.2.1. Basic Principle

At the beginning, the incoming X-ray pulse of the synchrotron is analyzed. This is important, for the later analysis in order to be able to describe the incoming X-rays. Using high resolution monochromators, the energy of the beam is tuned to the resonance energy of the material [52] which is supposed to be analyzed. For the case of analyzing ^{57}Fe , which is the archetype Mössbauer nucleus, the beam has the following properties. At Petra III, the energy of the beam is at 14.41 keV with an width of 1 meV. Compared to the linewidth $\hbar\gamma = 4.7$ neV of ^{57}Fe , the spectral bandwidth of the synchrotron pulse is very large. Therefore the input spectra can be approximately described as unity across the spectral region of the linewidth of the core transition.

In the time domain, the pulse duration of a synchrotron pulse is around 60 – 100 ps [12]. Compared to the life time of the core transition in ^{57}Fe , which is 141 ns, it is very short. Therefore, the incoming pulse can be described approximately as a δ -function in time and thus as unity in the energy domain.

In this section a intuitive explanation of the main principle of the phase manipulation via mechanical motion is given. For this, the temporal sequence of a scattering process without any external influence is analyzed first. For each X-Ray pulse irradiating a target, there are photons which are scattered resonantly, but the most are not. This is illustrated in figure 2.3a, considering only the first foil and therefore path one and two. Further, all resonantly scattered photons are delayed by a certain amount of time, compare with 2.3b.

This dynamical property of the scattering is used to add a phase shift to the scattered radiation. For this, the foil is displaced by Δz right after the excitation. As the non-resonant part has already passed the foil, the resonantly scattered part undergoes a phase shift of $\varphi_0 = k_0 \Delta z$. Using the notation of section 2.1.4, this can be written as,

$$R^{\varphi_0}(t) = \delta(t) + e^{i\varphi_0} R^S(t) \quad (2.44)$$

It is important to emphasize the importance of the additional phase φ_0 , which can modify the interference between the δ -pulse and the resonantly scattered part from destructive to constructive interference. At first glance this sounds quite counterintuitive, because, as depicted in figure 2.3b, the δ - pulse and the scattered radiation are separated in space and time. However, there is still a certain probability to find a scattered photon at time $t = 0$ as well. This can be seen quite clearly by taking the absolute square of the response function,

$$|R^{\varphi_0}(t)|^2 = |\delta(t)|^2 + |e^{i\varphi_0} R^S(t)|^2 + \underbrace{2\text{Re}(\delta(t)e^{i\varphi_0} R^S(t))}_{\text{Interference part}}. \quad (2.45)$$

Thus, the interference between the delta pulse and the resonantly scattered part is non-vanishing, however weak, because it is restricted to the time interval of the δ -function. Therefore, the absolute square of a time response of a single foil, does not change by an additional phase.

This looks different in energy space. By performing a Fourier-transform, the time variable is transformed into a frequency variable. Therefore there is no temporal separation of the different terms. As a consequence the additional phase can have an influence on all frequencies. Thus, in the energy space, a big influence of the phase is observable.

2.2.2. Mathematical Formalism for an Arbitrary Motion

The response function of a moving target can be calculated using a coordinate transformation, from the lab frame to the moving frame of the target and back. All values in the moving frame will be indicated by a prime e.g. $E'_0(t)$ whereas all symbols in the lab frame are written without a prime. In general the coordinate transformation can be performed by the following 3 steps:

1. First, it is necessary to transform the incoming pulse into the moving frame of the target: $E_{\text{in}}(t) \rightarrow E'_{\text{in}}(t)$.
2. In this moving system, the target is at rest, and can be convoluted with the transformed input in the time domain or multiplied in the energy domain, respectively: $R'_{\text{moving}}(t) = E'_{\text{in}}(t) * R(t)$, or $R'_{\text{moving}}(t) = \mathcal{F}^{-1} [\mathcal{F}(E'_{\text{in}}(t)) \cdot \mathcal{F}(R(t))]$
3. The calculated response function has to be transformed back to the lab frame: $R'_{\text{moving}} \rightarrow R_{\text{moving}}$.

First step For the first step it is necessary to formulate the transformation. The beam propagates in z -direction, and the movement of the target is also in z -direction. Therefore, the relation between the laboratory and the moving frame is,

$$z' = z - \Delta z(t), \quad (2.46)$$

where $\Delta z(t)$ describes the movement of the target. The incoming radiation pulse can be described by a wave packet [40],

$$E_{\text{in}}(t, z) = \frac{1}{\sqrt{2\pi}} \int E_0(k) e^{i(kz - \omega(k)t)} dk, \quad (2.47)$$

where k denotes the wave vector, $E_0(k)$ denotes the amplitude distribution in k -space, and $\omega(k)$ the dispersion relation. Due to the wave packet propagating in vacuum or air, it can be written as [37],

$$\omega(k) = \frac{c_0}{n(\omega)} k \approx c_0 k, \quad (2.48)$$

with $n(\omega)$ the index of refraction and c_0 the speed of light in vacuum. Since the index of refraction is equal to one in vacuum and approximately equal to one in air [38], this approximation holds, because the radiation travels only in air and vacuum. To transform the wave packet into the moving frame, the spatial coordinate z has to be substituted with z' ,

$$E'_{\text{in}}(t, z') = \frac{1}{\sqrt{2\pi}} \int E_0(k) e^{i(k \overbrace{(z - \Delta z(t))}^{z'} - c_0 kt)} dk \quad (2.49)$$

$$= \frac{1}{\sqrt{2\pi}} \int E_0(k) e^{i(kz) - c_0 kt} e^{-ikm(t)} dk. \quad (2.50)$$

Now, the properties of typical synchrotron radiation have to be taken into account. The energy of the radiation is typically on the order of several keV. Due to the use of high resolution monochromators (HRM) it is possible to have a bandwidth on the order of

2. Basic Theoretical Background

meV [12, 52, 53]. For instance at the P01 beamline of PETRA III, the radiation has a bandwidth of 1 meV at a photon energy of $\hbar\omega_0 = 14.41$ keV. This corresponds to a wavelength of,

$$\lambda = \frac{2\pi c_0 \hbar}{(14.41 \cdot 10^3 \pm 1 \cdot 10^{-3}) \text{ eV}}, \quad (2.51)$$

with the reduced Plank constant \hbar and the speed of light in vacuum c_0 . Therefore the wavenumber $k = \frac{2\pi}{\lambda}$ is,

$$\begin{aligned} k &= \frac{1}{\hbar c_0} (14.41 \cdot 10^3 \pm 1 \cdot 10^{-3}) \text{ eV} \\ &= 9.63 \cdot 10^8 \text{ s}^{-1} \pm 5.07 \cdot 10^3 \text{ s}^{-1} \end{aligned} \quad (2.52)$$

$$= k_0 \pm \Delta k. \quad (2.53)$$

This means that the deviation from k_0 by Δk is approximately $5.2 \cdot 10^{-4}$ %. Therefore in equation (2.50), it is justified to approximate k by k_0 in the last exponential function. This means, that the whole signal undergoes approximately the same phase shift because the spectral width of the transition is so small, that the variation of k in this range is negligible. As a consequence the transformed input can be written as,

$$E'_{\text{in}}(z', t) = e^{-ik_0 \Delta z(t)} \frac{1}{\sqrt{2\pi}} \int E_0(k) e^{i(kz) - c_0 kt} dk \quad (2.54)$$

$$= e^{-ik \Delta z(t)} E_{\text{in}}(z, t). \quad (2.55)$$

Second step The second step is to calculate the response of the target within the moving frame. Because the target is at rest in this frame, it is possible to use a response function at rest, too. Furthermore, in this case, there is no dispersion, due to the constant index of refraction. This means that the wave packet stays in its original shape at every point z . Taking further into account, that all optical elements and foils stay at the same place, it is possible to omit the spatial coordinate z at this point. A further property of the synchrotron radiation helps to simplify the upcoming calculations: Due to its very short duration in the time domain, the electric field of the input can be described using a δ -function [28],

$$E_{\text{in}}(t) = \delta(t) \quad (2.56)$$

Therefore the input function in the moving frame reduces to $E'_{\text{in}}(t) = \delta(t) \cdot e^{-ik_0 \Delta z(0)}$. In the general case, the input function has to be convoluted with the response function $R(t)$ of the target in the time domain. However, a convolution of any function with a δ -function is the function itself again. Therefore the response in the moving frame becomes,

$$R'_{\text{in}}(t) = e^{-ik_0 \Delta z(0)} R(t). \quad (2.57)$$

Because equation (2.57) describes the response of a moving target, the m in the subscript stands for moving. Note that for a general input field, the calculation of (2.57) is more complex. Due to the convolution being often quite difficult to calculate, the Fourier convolution theorem [39] is mostly used, to calculate it by transforming the equations to Fourier-space.

Third step As a third step is to the back transformation to the lab frame have to be performed. In principal it is possible to write equation (2.57) as a sum of plane waves, what is basically a Fourier-transformation, as well. Therefore it is possible to use the same formalism than for the transformation into the moving frame. Yet the sign of the phase shift changes from minus to plus. Consequently, the response function of a moving target in the lab-frame reads,

$$R_m(t) = e^{ik_0[\Delta z(t) - \Delta z(0)]} R(t). \quad (2.58)$$

In all cases of this thesis, $R(t)$ can be written as $R(t) = \delta(t) + R^S(t)$. Hence, the response function is,

$$R_m(t) = \delta(t) + e^{ik_0[\Delta z(t) - \Delta z(0)]} R^S(t). \quad (2.59)$$

This formula can be used for a general response function as well as for a arbitrary movement in z -direction, for the case of nuclear forward scattering with synchrotron radiation.

2.2.3. Step Function: Instant Phase Shift

An interesting pattern of movement is an instant step of the piezo at $t = 0$,

$$\Delta z(t) = A \cdot \theta(t). \quad (2.60)$$

Note that for an experiment an instant step is not possible. Here, A describes the amplitude of the step, $\theta(t)$ describes the Heaviside step function. Applying this to a single line resonance foil, which is described by equation (2.41), the response function reads,

$$\begin{aligned} R_m(t) &= \sqrt{2\pi} \delta(t) - e^{ik_0 A (\theta(t) - \theta(0))} \sqrt{2\pi} \theta(t) e^{-\frac{\gamma}{2}t - i\omega_0 t} \sqrt{\frac{2\pi b}{t}} J_1(2\sqrt{bt}) \\ &= \sqrt{2\pi} \delta(t) - e^{ik_0 A \theta(t)} e^{-\frac{\gamma}{2}t - i\omega_0 t} \sqrt{\frac{2\pi b}{t}} J_1(2\sqrt{bt}). \end{aligned} \quad (2.61)$$

In dependence of the amplitude A the product in the exponent can be taken together as a phase shift $\varphi_0 = k_0 A$.

2. Basic Theoretical Background

In the time domain the response function, does not depend on the phase shift φ_0 . However, it does in the energy domain. For transforming equation (2.61), it is rewritten as,

$$\begin{aligned} R_m(t) &= \sqrt{2\pi}\delta(t) + e^{i\varphi_0} \left[\sqrt{2\pi}\delta(t) - \theta(t)e^{-\frac{\gamma}{2}t-i\omega_0 t} \sqrt{\frac{2\pi b}{t}} J_1(2\sqrt{bt}) \delta(t) - \sqrt{2\pi}\delta(t) \right] \\ &= \sqrt{2\pi}\delta(t) + e^{i\varphi_0} \left[R(t) - \sqrt{2\pi}\delta(t) \right] \end{aligned} \quad (2.62)$$

The Fourier transform of $R(t)$ is known, equation (2.34) from chapter 2.1.3 and the Fourier transform of $\sqrt{2\pi}\delta(t)$ is one. Therefore the solution is,

$$\hat{R}_m(\Delta) = 1 + e^{i\varphi_0} \left(e^{\frac{-ib}{\Delta-i\gamma/2}} - 1 \right). \quad (2.63)$$

In figure 2.4, the absolute square of equation (2.63) is plotted for different values of φ_0 .

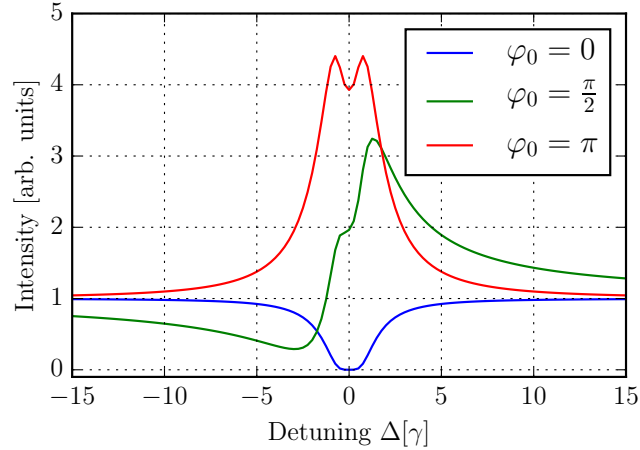


Figure 2.4.: Energy spectrum of a single line resonance foil ($b = 2$, $\gamma = 1$) with an instant phaseshift φ_0 . For $\varphi_0 = \pi/2$ the spectrum has a Fano-like shape. For $\varphi_0 = \pi$, the dip of the spectrum without phaseshift turns to a peak. This can be explained by turning destructive interference to constructive interference, using the phaseshift φ_0 . The Detuning is in units of γ , where γ refers to the linewidth of ^{57}Fe , $\hbar\gamma = 4.7$ neV.

For $\varphi_0 = \pi/2$, the spectrum has a Fano-like shape. For $\varphi_0 = \pi$, the dip at resonance has turned to a peak. This phenomena has been investigated theoretically as well as experimentally in [25]. The explanation is the change from destructive to constructive interference between the non-resonant and the resonant scattered parts of the radiation, as explained in section 2.2.1.

2.2.4. Oscillations: Generation of sidebands

Another motion pattern are harmonic oscillations of the piezo. Therefore, the displacement of the piezo can be described by,

$$\Delta z(t) = A \cdot \sin(\omega_p t + \varphi_0). \quad (2.64)$$

Here, A , describes the amplitude and φ_0 the elongation of the piezo in the moment, the X-ray pulse hits the target. This movement has been studied in [24], using an radioactive source, and in e.g. [50, 54], using synchrotron radiation as a source.

In the following there will be a short derivation of the energy spectrum for a vibrating single line resonance foil, irradiated by a synchrotron pulse. Starting point is equation (2.59). Substituting $R(t)$ with equation (2.41), and $\Delta z(t)$ with (2.64) yields,

$$R_{\text{osc}}(t) = \sqrt{2\pi} \delta(t) - e^{ip[\sin(\omega_p t + \varphi_0) - \sin(\varphi_0)]} \theta(t) e^{-\frac{\gamma}{2}t - i\omega_0 t} \sqrt{\frac{2\pi b}{t}} J_1(2\sqrt{bt}). \quad (2.65)$$

Here $p = A \cdot k_0$ is a dimensionless value of the oscillation amplitude. If the time spectra of this is measured, there will be no difference to a foil in rest, because the additional phase drops out again, while taking the absolute square of the electric field at the detector.

However, in the energy spectrum, the phase has a big influence again. To perform the Fourier transformation the time dependent phase has to be expanded using the Jakobi-Anger relationship,

$$e^{ip \sin(x + \varphi_0)} = \sum_{n=-\infty}^{\infty} J_n(p) e^{in(x + \varphi_0)}. \quad (2.66)$$

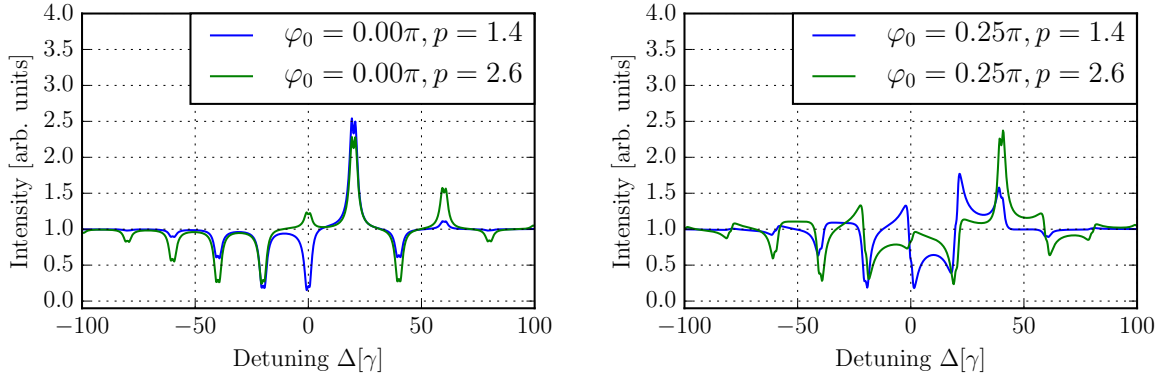
Inserting this in equation in (2.65), the response function reads,

$$\begin{aligned} R_{\text{osc}}(t) &= \sqrt{2\pi} \delta(t) - \sum_{n=-\infty}^{\infty} J_n(p) e^{-ip \sin(\varphi_0) + in\varphi_0} \theta(t) e^{-\frac{\gamma}{2}t} e^{-i(\omega_0 - \omega_p)t} \sqrt{\frac{2\pi b}{t}} J_1(2\sqrt{bt}) \\ &= \sqrt{2\pi} \delta(t) - \\ &\quad \sum_{n=-\infty}^{\infty} J_n(p) e^{-ip \sin(\varphi_0) + in\varphi_0} \cdot \left[\right. \\ &\quad \left. \sqrt{2\pi} \delta(t) - J_n(p) \theta(t) e^{-\frac{\gamma}{2}t} e^{-i(\omega_0 - \omega_p)t} \sqrt{\frac{2\pi b}{t}} J_1(2\sqrt{bt}) - \sqrt{2\pi} \delta(t) \right]. \end{aligned} \quad (2.67)$$

This can be transformed to the energy domain using the results from section 2.1.3. Therefore it yields,

$$\hat{R}_{\text{osc}}(\Delta) = 1 - \sum_{n=-\infty}^{\infty} J_n(p) e^{in\varphi_0 - ip \sin(\varphi_0)} \left(\exp \left(\frac{-ib}{\Delta - \omega_p + \frac{i\gamma}{2}} \right) - 1 \right). \quad (2.68)$$

2. Basic Theoretical Background



- (a) Energy spectrum with $\varphi_0 = 0$ and different values of p . The influence of p can be seen quite good comparing the different amplitudes of the individual sidebands.
- (b) Energy spectrum with $\varphi_0 = 0$ and different values of p . φ_0 has a big influence on the shape of the individual sidebands.

Figure 2.5.: Energy spectra for an oscillating single resonance foil ($\omega_p = 20$, $\gamma = 1$, $b = 2$). The oscillation generates sidebands. Each sideband n is weighted with $J_n(p)$. Therefore, the value of p has a big influence on the amplitude of the peaks. This can be seen quite good in (a). It is interesting to see that for a positive detuning, the sidebands are alternating peaks and dips. This is due to a phaseshift of π originating from the property (2.69) of the Bessel functions. Furthermore there is a big influence of the offset φ_0 on the individual sidebands. For values $\varphi_0 \neq m\pi$, $m \in \mathbb{N}$, the sidebands are shaped Fano-like.

This equation is plotted in figure 2.5 for different values of p and φ_0 . These results are important for the further results of this thesis. Especially the dependency on the offset φ_0 will become important. In the following the features of the spectra and the influence of the different parameters will be discussed. The main influence of the oscillation is causing the emergence of sidebands. Looking at equation (2.68), each n of the sum stands for one sideband, whereas the sidebands referring to positive n are left hand of the resonance (negative Δ) and vice versa. The sideband with $n = \pm 1$ are next to resonance, the absolute of n is increasing whilst moving to the edge of the spectra. The spectral distance of each sideband is exactly ω_p , and therefore the distance of the n -th sideband to resonance is equal to $n \cdot \omega_p$. Further, each sideband n is weighted with the Bessel function $J_n(p)$. Therefore p influences on how the spectra look like. In figure, 2.6, the first five orders of the Bessel-function of the first kind are plotted. As one can see there, for $p = 2.6$, the 0th order Bessel function becomes small and, which is important, negative. Therefore the 0th sideband becomes a peak instead a dip. Furthermore $J_1(2.6) \approx J_2(2.6)$, which means that the first and the second sideband have the same amplitude, which can be seen in the figure as well. Furthermore, the sidebands

at positive detuning are alternating peaks and dips. This is due to the property,

$$J_{-n}(p) = (-1)^n J_n(p), \quad (2.69)$$

which leads to alternating signs for the amplitude of those sidebands. For even n , the sidebands remain as dips, however, for odd n , the minus sign is equal to a instant phase shift of π which turns them into peaks.

A really important property is the dependence of the parameter φ_0 , which describes the elongation of the oscillation at the moment, the radiation hits the target. For values of $\varphi_0 \neq m\pi$, $m \in \mathbb{N}$, the sidebands are shaped Fano-like. Therefore, φ_0 has the same influence than it has in the case of an instant jump. At first glance this can be confusing, because in the case of an instant phase shift, φ_0 is proportional to the amplitude of the jump, the piezo performs.

However, for an oscillation, p is proportional to the amplitude of the oscillation, what could lead to the assumption that p would overtake the effect of φ_0 . However, this is only true partially. To answer this question, it is important to think about the mechanism behind this effect. In formula (2.68), the additional phase coming from the oscillation can be split into a time dependent ($e^{ip \sin(\omega_p t + \varphi_0)}$) and a constant ($e^{-ip \sin(\varphi_0)}$) part. At $t = 0$, they add to zero. This means, that the non resonant part, which hits the target at $t = 0$ does not have any additional phase. However, all resonant scattered parts are delayed and therefore have this additional phase $e^{ip \sin(\omega_p t + \varphi_0) - ip \sin(\varphi_0)}$, consisting of the time dependent and the time independent part.

In the case of a instant phase shift, there happens the same mechanism, however, with the difference that the whole additional phase is constant for $t > 0$. Comparing these two mechanism, it turns out that for oscillations the part constant in time, id est $-p \sin(\varphi_0)$, overtakes the part of φ_0 in the case of an instant jump.

This can be seen in figure 2.5b as well. For the spectra of the same color plotted in (a) and (b), the same values for p have been used but different values for φ_0 . This results in a different shape of the spectra in (a) and (b).

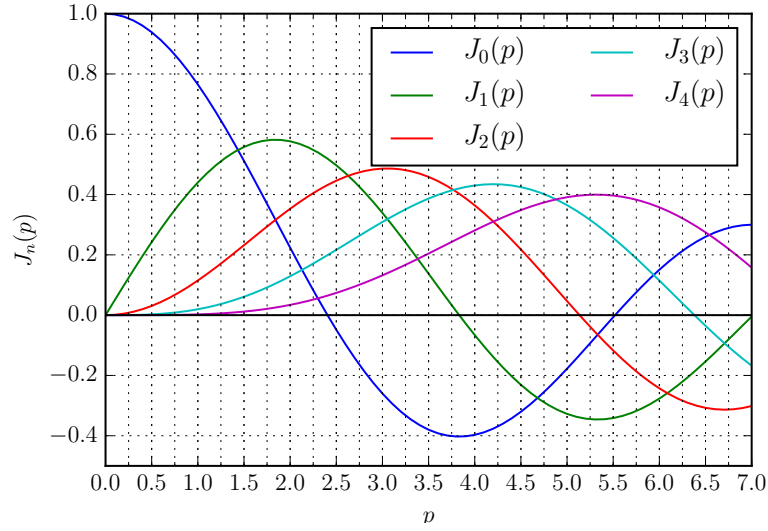


Figure 2.6.: The first 5 orders of the Bessel-functions of the first kind in dependency of a real parameter p . They are important for oscillating foils, because they weight each sideband.

2.3. Approximation For Thin Foils

It is possible to find a approximation for the Bessel function in equation (2.41) [55]. For this the Bessel function including the square root is expanded in a taylor series,

$$\frac{J_1(2\sqrt{bt})}{\sqrt{bt}} \approx 1 - \frac{bt}{2} + \frac{b^2t^2}{12} + \dots \quad (2.70)$$

It is compared with the expansion of an exponential function with argument $-\frac{b}{2}t$,

$$e^{-\frac{b}{2}t} \approx 1 - \frac{bt}{2} + \frac{b^2t^2}{8} + \dots \quad (2.71)$$

There is a good agreement in the leading orders. The approximation is valid if $t < \frac{4}{b}$ which is approximately the first minimum of $\frac{J_1(2\sqrt{bt})}{\sqrt{bt}}$. Therefore the approximation holds for thick targets or short times. Applying it to equation (2.41), the approximation reads,

$$R(t) \approx \sqrt{2\pi}\delta(t) - \sqrt{2\pi}be^{-i\omega_0t}e^{-\frac{\gamma+b}{2}t}\theta(t). \quad (2.72)$$

This can be transformed quite easily to the Energy domain,

$$\hat{R}(\Delta) \approx 1 - \frac{ib}{\Delta + i\frac{\gamma+b}{2}}. \quad (2.73)$$

3. Theoretical Examination of φ_0

3.1. Effect of Mechanical Motion in the Time Domain

In section 2.2, the response function of a moving target have been calculated. One result that have been found, is that in a measured time spectrum, the influence of the phase can't be measured. This is because of the fact, that only the absolute square of the electric field can be measured. Since the movement results in an additional complex phase for the scattered part (compare with equation (2.59)), it drops out for all times $t \neq 0$.

Measurements in experiments with synchrotron radiation are mostly done in time domain, using time resolved single photon detectors. Therefore it would be desirable to measure the influence of the motion in time domain, too.

This can be done by placing a second foil after the first foil, which is moved by a piezo. The reason for this can be understood intuitively by looking at figure 2.3b. Path two and four do resonantly scatter at the first foil. Now, if the first foil is moved by an piezo, these two paths, undergo a phase shift. Path 3, does not scatter resonantly at the first foil, but scatters at the second foil. Therefore, it is delayed due to the scattering process. As a consequence the radiation of path number two and three will have approximately the same space time coordinate, after the second foil and can interfere. Hence, even by looking at this simplified picture, it can be explained that there is interference at least between path two and three. This interference explains why now an influence of the motion in time domain can be measured.

The question arises, how the time spectrum changes if an additional phase is applied to the target. To answer this question, in this case the following setup is used. There are two foils in a row. The first one is mounted on a piezo foil, which can perform an arbitrary movement. The second one is mounted on a Mössbauer drive, moving with constant velocity v_D . As a result, the resonance frequency is shifted by $S = \omega_0 \frac{v_D}{c_0}$.

3.1.1. Instant Phase Shift

First, an instantaneous jump of the piezo is considered. As already mentioned in section 2.2, the motion can be described via $\Delta z(t) = A\theta(t)$. This leads to an instant phase shift

3. Theoretical Examination of φ_0

of $\varphi_0 = k_0 A$, which acts on the resonantly scattered part of the first foil. Therefore, it can be described by,

$$\hat{R}_1(\Delta) = 1 + e^{i\varphi_0} \left(\exp \left(\frac{-ib_1}{\Delta + \frac{i\gamma_1}{2}} \right) - 1 \right). \quad (3.1)$$

The second foil is mounted on a Doppler-drive. This results in a shift of its resonance frequency by S . Therefore, the response function of the second foil reads,

$$\hat{R}_2(\Delta) = \exp \left(\frac{-ib_2}{\Delta - S + \frac{i\gamma_2}{2}} \right). \quad (3.2)$$

In the energy space the response function of two foils in a row can simply multiplied. Therefore, the electric field measured at the detector reads,

$$\hat{E}(\Delta) = \exp \left(\frac{-ib_2}{\Delta - S + \frac{i\gamma_2}{2}} \right) + e^{i\varphi_0} \left(\exp \left(\frac{-ib_1}{\Delta + \frac{i\gamma_1}{2}} \right) - 1 \right) \cdot \exp \left(\frac{-ib_2}{\Delta - S + \frac{i\gamma_2}{2}} \right). \quad (3.3)$$

Since the question of this section asks for the influence in the time domain, this expression have to be transformed to the time domain. Unfortunately, there does not exist a closed analytical Fourier transformation for this function. Therefore the approximation for thin films, introduced in 2.3, is used to simplify the terms. The simplified formulae are,

$$\hat{R}_1(\Delta) \approx 1 - \frac{e^{i\varphi_0} ib_1}{\Delta + i \frac{\gamma_1 + b_1}{2}}, \quad (3.4)$$

$$\hat{R}_2(\Delta) \approx 1 - \frac{ib_2}{\Delta - S + i \frac{\gamma_2 + b_2}{2}}. \quad (3.5)$$

It is important to note, that each formula consists of a Lorentzian shaped peak subtracted from unity. The one describe the prompt δ -pulse in time domain. The Lorentzian describes the resonant scattered radiation. As before, the product of the two terms gives the electric field in the time domain

$$\hat{E}(\Delta) \approx 1 - \frac{e^{i\varphi_0} ib_1}{\Delta + i \frac{\gamma_1 + b_1}{2}} - \frac{ib_2}{\Delta - S + i \frac{\gamma_2 + b_2}{2}} + \frac{e^{i\varphi_0} ib_1}{\Delta + i \frac{b_1 + \gamma_1}{2}} \cdot \frac{ib_2}{\Delta - S + i \frac{b_2 + \gamma_2}{2}}. \quad (3.6)$$

The fourth part in the equation describes the scattering path number four in figure 2.3b. This term can be neglected for the following reason. The probability, that a photon scatters resonantly with a foil is the highest at its resonance frequency. Off resonance, the probability decreases quickly to almost zero. Due to the Doppler-drive, the resonances are separated from each other by the distance S . Therefore, the high probability at resonance of foil one is multiplied with the almost zero off resonance

probability at foil 2 and vice versa. Hence, the whole term becomes approximately zero. Applying this approximation, one obtains,

$$\hat{E}(\Delta) \approx 1 - \frac{e^{i\varphi_0} i b_1}{\Delta + i \frac{\gamma_1 + b_1}{2}} - \frac{i b_2}{\Delta - S + i \frac{\gamma_2 + b_2}{2}}. \quad (3.7)$$

For all parts of this expression the Fourier transformations are known. Hence, in the time domain, it becomes,

$$E(t) \approx \sqrt{2\pi} \delta(t) - e^{i\varphi_0} b_1 e^{-i\omega_0 t - \Gamma_1 t} \theta(t) b_2 e^{-i(\omega_0 + S)t - \Gamma_2 t} \theta(t). \quad (3.8)$$

Here the acronym $\Gamma_{1/2} = \frac{b_{1/2} + \gamma_{1/2}}{2}$ has been used.

To calculate the corresponding intensity, it is necessary to take the absolute square of the above electric field. In the process, all terms containing the δ -function are disregarded, because they give only a contribution at $t = 0$ and therefore do not contribute to the dynamics at $t > 0$. The absolute square then reads,

$$|E(t)|^2 \approx \theta(t) b_1^2 e^{-\Gamma_1 t} + \theta(t) b_2^2 e^{-\Gamma_2 t} + 2b_1 b_2 e^{-(\Gamma_1 + \Gamma_2)t} \theta(t) \cos(\varphi_0 + St). \quad (3.9)$$

The first two terms decay exponentially, but do not have any other dependencies of the time. The third term shows oscillations in time domain. For a possible measurement, it is possible to predict to have a exponential decaying envelope, due to the first two terms. The cosine will result in equidistant minima. Their position depend on the value of φ_0 .

To give a short summary, it is possible to measure an influence of a moving foil at the time spectra, if two foils are placed in a row. The calculation, using the approximation of thin foils, predicts that there will be equidistant minima in the time spectra. Their distance depends on S and the absolute position of the minima on φ_0 . Those equidistant minima, which depend on the distance of two peaks in the energy domain, are known in the literature as quantum beats, see e.g. [28, 50, 54, 55].

To check the predictions of the approximation, the whole system is implemented and simulated numerically. For the simulation, the following values have been used: $b_1 = b_2 = \gamma_1 = \gamma_2 = 1$ and $S = 80$. The result is plotted in figure 3.1.

The qualitative predictions of the approximated formula (3.9) match the simulation well: Due to the cosine term, periodically and equidistant extrema are expected. This can be seen clearly in figure 3.1. The time T between the extrema can be calculated. For this, note, that the scaling of the energy axis is in units of the linewidth of ^{57}Fe , which is $\gamma_{\text{Fe}} = 4.7$ neV. Therefore the expected time between of the extrema is,

$$T = \frac{2\pi\hbar}{\gamma_{\text{Fe}} S} = \frac{1}{S} \cdot 879 \cdot 10^{-9} \text{ s} = 10.99 \text{ ns} . \quad (3.10)$$

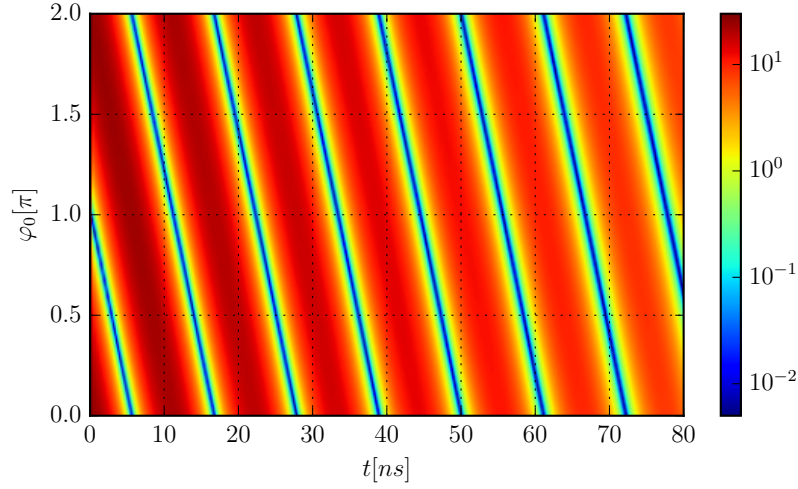


Figure 3.1.: Intensity of two foils in a row. The first is mounted on a piezo and the second on a Doppler Drive. The first is phase manipulated with an instant phaseshift of φ_0 , which is plotted on the y-axis. The second foil is mounted on a Doppler-drive which shifts its resonance frequency by S . An approximated calculation of the intensity is given in (3.9), which predicts a time domain separation of the minima of $T = 10.99$ ns which matches the result of this figure, which was obtained by a numerical simulation without any approximations. Furthermore, the calculation predicts that for $\varphi_0 = \pi$ the first minimum is at $t = 0$ and that the position of the minima depend linearly on φ_0 , which also matches. The exponential decay predicted in (3.9) can be seen as well. On the left hand side the intensity of red is much higher than it is at the right hand side. The values of the parameters chosen here are $b_1 = b_2 = \gamma_1 = \gamma_2 = 1$ and $S = 80$.

This value is in agreement with the simulation. The linear shift of the minima as a function of φ_0 matches, too.

The conclusions of this section are the following. The radiative coupling between two foils in a row lead to equidistant extrema, which are known in the literature as quantum beats. The time distance between the extrema depends on the difference of the resonance frequencies in the energy domain. Applying a phase shift of φ_0 to the resonant scattered part of the first foil, it is possible to control the position of the extrema. This is a really interesting result because it offers the possibility to use φ_0 as an additional, controllable degree of freedom. A more thorough analysis of the implications and possible applications of this result is given at the end of the next section (3.1.2), after considering an oscillatory motion pattern, too.

3.1.2. Oscillating foil

The case discussed in the previous section, raises the question, of what happens if the first foil is moved with a oscillatory motion pattern than a instantaneous jump. The setup is the same as before, the first foil is mounted on a piezo, the second is mounted on a Doppler drive. Only the motion of the piezo changes. It can now be described by,

$$\Delta z(t) = A \sin(\omega_p t + \varphi_0). \quad (3.11)$$

The principal of how to calculate the electric field at the detector remains the same, however, the response function of the foil mounted on the piezo changes to equation (2.68). The resulting expression contains a multiplication of two response functions as again. As before, it is not possible to transform the exact equation to time domain. The single steps of the calculation of the electric field at the detector remain the same. Therefore, the electric field at the detector it is given directly using the thin foil approximation,

$$\hat{E}(\Delta) \approx 1 - \sum_{n=-\infty}^{\infty} \underbrace{J_n(p) e^{-ip \sin(\varphi_0) e^{-in\varphi_0}}}_{\alpha_n} \left(\frac{-ib_1}{\Delta + n\omega_p + i\Gamma_1} \right) - \frac{ib_2}{\Delta - S + i\Gamma_2}. \quad (3.12)$$

The same abbreviations as before have been used, that is $\Gamma_m = \frac{b_m + \gamma_m}{2}$ and $p = k_0 A$. In the time domain, the above equation reads,

$$E(t) \approx \sqrt{2\pi} \delta(t) - \sum_{n=-\infty}^{\infty} \alpha_n b_1 e^{-i(\omega_0 + n\omega_p)t} e^{-\Gamma_1 t} \theta(t) - b_2 e^{-i\omega_0 t} e^{-\Gamma_2 t} \theta(t). \quad (3.13)$$

For comparing it with a possible measurement, the absolute square is calculated. Here, all terms containing the δ -function are dropped, such that,

$$\begin{aligned} |E(t)|^2 = & b_1^2 e^{-2\Gamma_1 t} \theta(t) \cdot \left| \sum_{n=-\infty}^{\infty} \alpha_n e^{-in\omega_p t} \right|^2 + b_2^2 \theta(t) e^{-2\Gamma_2 t} \\ & + 2b_1 b_2 e^{-(\Gamma_1 + \Gamma_2)t} \text{Re} \left[\sum_{n=-\infty}^{\infty} J_n(p) e^{-i(p \sin(\varphi_0) + n\varphi_0 + St)} \right]. \end{aligned} \quad (3.14)$$

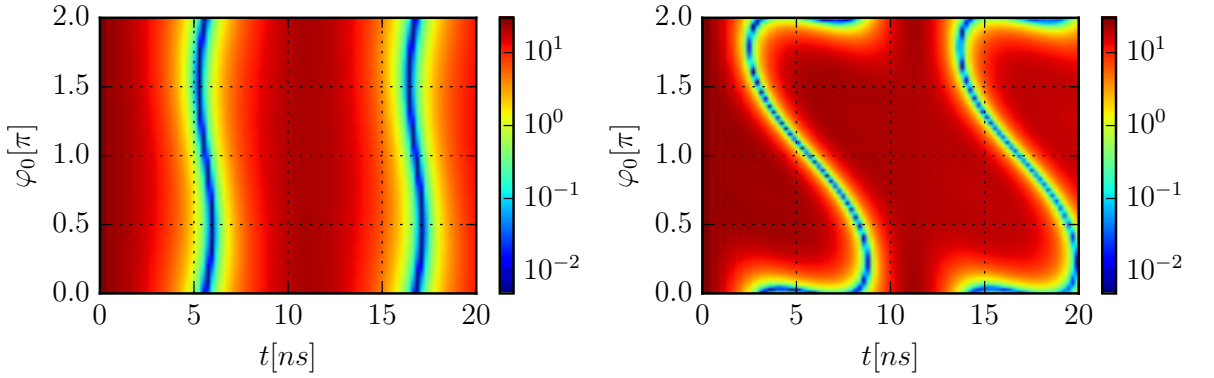
This equation is more complex, especially due to the sum. Each part of the sum describes one sideband, created by the oscillation. It is possible to simplify it by the right choice of the parameters of the motion pattern. To understand this, the impact of each of the parameters on the energy spectra of the foil have to be understood. In 2.2 they have been discussed in detail. Hence, here only a short recap is given. The parameter p weights each sideband n with $J_n(p)$. ω_p is equal to the distance between two sidebands, while φ_0 shapes their form. Therefore, to simplify the sum, p has to be chosen in a way that only a few, or in the ideal case, just one part of the sum remains. Looking at the

3. Theoretical Examination of φ_0

plotted Bessel function in figure 2.6, this is indeed the case for small p . There, all Bessel functions, except for $J_0(p)$ converge to zero, whilst $J_0(p)$ converges to one. Therefore, only the part of the sum with $n = 0$ remains in the sum and the electric field becomes,

$$|E(t)|^2 \approx b_1^2 e^{-2\Gamma_1 t} \theta(t) \underbrace{|\alpha_0|^2}_{=J_0(p) \approx 1} + b_2^2 \theta(t) e^{-\Gamma_2 t} + 2b_1 b_2 e^{-(\Gamma_1 + \Gamma_2)t} \underbrace{J_0(p)}_{\approx 1} \cos [St - p \sin(\varphi_0)]. \quad (3.15)$$

Again, to check the predictions of the approximation, the system has been simulated with the parameters $b_1 = b_2 = \gamma_1 = \gamma_2 = 1$ and $S = \omega_p = 80$. The results are given in figure 3.2. In 3.2a, the case for $p = 0.1$ is plotted, which is small enough for the approximation



(a) The amplitude of oscillation is $p = 0.1$, which is small enough for the small p approximation to apply. (b) The amplitude of oscillation is $p = 1.4$. The approximation for small p breaks down, as the change of the position of the minima with respect to φ_0 is no longer periodic.

Figure 3.2.: Intensity of two foils in a row, the first oscillates with frequency $\omega_p = 80$ on a piezo, the second is mounted on a Doppler drive which shifts its resonance frequency by $S = 80$. The offset of the oscillation φ_0 is plotted on the y -axis. These plots have been generated by simulation. In equation (3.15), an approximation of the system is given, which is used to make an analytical prediction of the shape of the waveforms. For its derivation a small value of p have been assumed, therefore it approximates the case in (a). In this case it predicts equidistant extrema with a time spacing of $T = 10.99$ ns. Furthermore, the position of the extrema is modulated with $p \sin(\varphi_0)$, which matches the results shown in (a). In the case of larger p the approximation breaks down and the intensity is described by equation (3.14). The chosen values for the parameters are $b_1 = b_2 = \gamma_1 = \gamma_2 = 1$.

to hold. The distance of the extrema in time is predicted to be the same as in the previous

case, i.e. $T = 10.99$ ns. This matches with the simulation. Furthermore, for small p , the absolute position of the minima is predicted to be modulated with $p \sin(\varphi_0)$, what holds as well. For $\varphi_0 = 0$ the position of the first minimum should be at $t = T/2 \approx 5.5$ ns, because at this value the cosine in equation 3.15 becomes zero. For small p this is indeed the case, as can be seen in figure 3.2a. If p increases, the approximation breaks down. An example in such a parameter regime is plotted in 3.2b. The reason for this can be seen using equation (3.14). The sums in these terms arise from the sidebands, which are created by the oscillation. This means that the part n stands for the n -th sideband. Due to this additional parts, which can be neglected for small p , the pattern in the time domain becomes more complex. This will not be evaluated further at this point. To do so, a more complex model would be necessary.

However, the question of the beginning, if a dependency of φ_0 in the time domain can be measured, could be answered even with this simple model.

Short summary A short summary of the results of the last two section is made in the following. If two foils are placed in a row, it is possible to measure an influence of an additional phase induced by mechanical motion at one foil, in time domain. Furthermore, for the case of an instant displacement, φ_0 can be used as a parameter to control the position of the minima. In the case of oscillations it can be used to change the shape of the waveform in the time domain. The potential of this result can be used considering the following. In section 2.2 it turned out, that φ_0 manipulates the shape of the spectra in the energy domain. Considering the setup, of two foils in a row, the shape of the energy spectrum has an influence on the time domain as well. However, the fact that the shape in the energy domain is *controllable* by φ_0 makes this result important. Because this offers the possibility to use φ_0 as an additional, controllable degree of freedom, which influences the spectrum in the energy and in the time domain. And since the effect of φ_0 is measurable in time domain, it potentially allows to make a statement about the shape of a target in the energy domain via a measurement in time domain. In chapter 4, this controllable degree of freedom is going to be used to develop a new method to determine the spectrum and the phase of a target in the energy domain.

3.2. Influence of φ_0 in the Energy Domain

In the previous chapter, it was found that φ_0 can be used as a controllable degree of freedom, which influences the spectrum in the energy and the time domain. It has the potential that it is possible to get information of shape of the energy spectrum by a measurement in the time domain. Motivated by this, the impact of φ_0 to the energy spectrum is investigated more thoroughly in this chapter.

3. Theoretical Examination of φ_0

In chapter 2, the influence of φ_0 in the case of an instant jump, on the absolute square of the response function in the energy domain have been investigated. The result was plotted in figure 2.4. There it could be seen that depending on the value of φ_0 the shape of the response function changed to a Fano-like shape for $\varphi_0 = \frac{\pi}{2}$ to a peak for $\varphi_0 = \pi$.

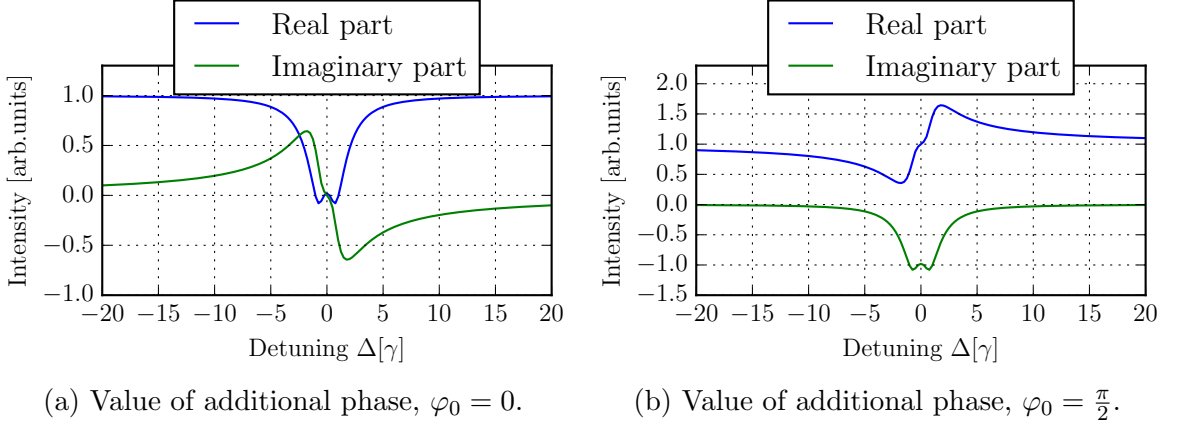


Figure 3.3.: Real and imaginary part of a single resonance line absorber with an additional phase of φ_0 . For a value of $\varphi_0 = \frac{\pi}{2}$ the real and imaginary part change, such that the real part become the imaginary part, and vice versa, except for the baseline of the real part which is independent of φ_0 . Because of this baseline, the real part contributes stronger if the absolute square is taken.

For this equation (3.1) is split into its real and imaginary part,

$$\begin{aligned} \hat{R}(\Delta, \varphi_0) = & 1 + e^{\frac{-b\frac{\gamma}{2}}{\Delta^2 + \frac{\gamma^2}{4}}} \cos\left(\frac{b\Delta}{\Delta^2 + \frac{\gamma^2}{4}} + \varphi_0\right) - \cos(\varphi_0) \\ & - i \left[e^{\frac{-b\frac{\gamma}{2}}{\Delta^2 + \frac{\gamma^2}{4}}} \sin\left(\frac{b\Delta}{\Delta^2 + \frac{\gamma^2}{4}} - \varphi_0\right) + \sin(\varphi_0) \right]. \end{aligned} \quad (3.16)$$

As one can see, the real and imaginary part depend on the value of φ_0 . For $\varphi_0 = 0$, the real and imaginary part read,

$$\text{Re}\left(\hat{R}(\Delta, 0)\right) = e^{\frac{-b\frac{\gamma}{2}}{\Delta^2 + \frac{\gamma^2}{4}}} \cos\left(\frac{b\Delta}{\Delta^2 + \frac{\gamma^2}{4}}\right), \quad (3.17)$$

$$\text{Im}\left(\hat{R}(\Delta, 0)\right) = -e^{\frac{-b\frac{\gamma}{2}}{\Delta^2 + \frac{\gamma^2}{4}}} \sin\left(\frac{b\Delta}{\Delta^2 + \frac{\gamma^2}{4}}\right). \quad (3.18)$$

If the phase jump changes now to a value of $\varphi_0 = \frac{\pi}{2}$ they become,

$$\begin{aligned} \operatorname{Re}\left(\hat{R}(\Delta, \pi/2)\right) &= 1 - e^{\frac{-b\frac{\gamma}{2}}{\Delta^2 + \frac{\gamma^2}{4}}} \sin\left(\frac{b\Delta}{\Delta^2 + \frac{\gamma^2}{4}}\right) \\ &= 1 - \operatorname{Im}\left(\hat{R}(-\Delta, 0)\right), \end{aligned} \quad (3.19)$$

$$\begin{aligned} \operatorname{Im}\left(\hat{R}(\Delta, \pi/2)\right) &= e^{\frac{-b\frac{\gamma}{2}}{\Delta^2 + \frac{\gamma^2}{4}}} \cos\left(\frac{b\Delta}{\Delta^2 + \frac{\gamma^2}{4}}\right) - 1 \\ &= \operatorname{Re}\left(\hat{R}(\Delta, 0)\right) - 1. \end{aligned} \quad (3.20)$$

Here have been used that $\cos(x + \frac{\pi}{2}) = -\sin(x)$ and $\sin(x - \frac{\pi}{2}) = -\cos(x)$.

This means, that for an additional phase of $\varphi_0 = \frac{\pi}{2}$ the realpart turns into the imaginary part and vice versa, except for the baseline within the realpart, which is constant with respect to φ_0 . This is illustrated in figure 3.3. If the absolute square of this signal is taken, the real part contributes stronger due to the baseline. This can be seen as well in figure 2.4. For a phase of $\varphi_0 = \frac{\pi}{2}$, the absolute square has a similar shape as the real part in figure 3.3b.

The analysis could be made similar for the case of an oscillatory movement pattern. The calculations become more complicated, however, the key message remains the same.

The result of this is that it is possible to get information about the real and the imaginary part of the spectrum, even if only the absolute square of the spectrum in the energy domain is known.

4. Determination of Energy Spectrum And Phase Using φ_0

A major challenge for all experiments using highly energetic radiation with very small transition energies, such as for Mössbauer Nuclei, is the measurement of the energy spectrum. For example, the resonance frequency ω_0 of the nuclear transition of Iron-57 from state $I = 3/2$ to $I = 1/2$ is at $\hbar\omega_0 = 14.4$ keV, whereas the linewidth γ of the transition is 12 orders of magnitudes smaller, $\hbar\gamma = 4.7$ neV [28]. Such a small resolution of γ at frequency of ω_0 can not be achieved by grating or prism-based spectrometers, known from the optical range.

This can be demonstrated with a short calculation. The equation describing the diffraction is $d \sin(\theta) = m\lambda$, with the slit distance d , the order of diffraction m and the diffracted angle θ . To find the resolution, the differential is taken, $m\Delta\lambda = d \cos(\theta)\Delta\theta$, where $\Delta\lambda$ is the required resolution in wavelength and $\Delta\theta$ the corresponding angle. Substituting d in the equation for the resolution with the expression of the diffraction yields,

$$\Delta\theta = \frac{\Delta\lambda}{\lambda} \tan(\theta). \quad (4.1)$$

The fraction of $\frac{\Delta\lambda}{\lambda}$ can be expressed using the energies $\hbar\omega_0$ and $\hbar\gamma$ as well: $\frac{\Delta\lambda}{\lambda} = \frac{\gamma}{\omega_0 + \gamma} \approx \frac{\gamma}{\omega_0}$. For the case of ^{57}Fe , with $\hbar\omega_0 = 14.4$ keV and $\hbar\gamma = 4.7$ neV, and assuming an angle of diffraction of $\theta = 30^\circ$ the angle which have to be resolved is,

$$\Delta\theta \approx 1.88 \cdot 10^{-13}. \quad (4.2)$$

To resolve such a small angle on a screen, a screen distance in the order of 10^9 m would be needed, what is obviously not possible.

To overcome the limitation of grating-based spectrometers, several alternative approaches have been proposed.

One approach to measure the spectrum is to use a radioactive source, the most used example being ^{57}Co , which decays to an excited state of ^{57}Fe [24, 27]. During de-excitation, this state emits a photon with an energy of $\hbar\omega_0 = 14.4$ keV and a linewidth

of $\hbar\gamma = 4.7$ neV. By moving this source on a Doppler-drive, this leads to tunable, small banded source.

Another possibility is to use a narrow band, tunable radiation source, such as the “Synchrotron-Mössbauer-Source”(SMS) [26]. It provides radiation within a bandwidth of 15 neV, tunable in a range of ± 0.6 μeV at an energy of 14.4 keV. Due to the small bandwidth and the possibility to tune the frequency, this source, can be used to sample an unknown target.

Another possibility is to use a method called late-time integration with a Doppler-drive. For this method a narrow-band analyzer mounted on a Doppler-drive is used to sample the target. The used radiation are x-ray pulses originating from a synchrotron, which can be described as unity in the energy domain. The spectral response function of the analyzer is a narrow-banded absorption dip. This is in some sense the inverse to the SMS. In order to reconstruct the energy spectrum using this setup, the conventional method is to integrate the measured time spectrum over a time interval at late times. This method is well established in nuclear spectroscopy and has been successfully used in several experiments, e.g. [21, 56].

However, despite their individual advantages, each of them also suffers from certain disadvantages.

A radioactive source has a low intensity and therefore it requires long measuring times. Furthermore, the beam is not collimated, which excludes this method to measure the spectrum of e.g. a cavity.

The SMS is technically challenging to produce, furthermore, the X-ray pulse is much longer than X-rays originating directly from a synchrotron. Therefore, they can not be described as a δ -function anymore. This excludes the SMS for some experiments, where the δ -pulse is needed .

The late-time integration method can be used only if the linewidth of the target is much larger than the one of the analyzer. Furthermore, there is no theory of how the time interval has to be chosen. Therefore it requires a guess of the time interval, more based on experience rather than on quantitative arguments.

Therefore, the need for a precise, flexible and reliable methods to measure the energy spectra of a target with a high resolution is still present, and both experimental and theoretical effort is required overcome the current limitations.

In the following a new method for this problem is presented. It will be called “Oscillation-drive” in the following. The Oscillation-drive has an outstanding advantage compared with all other methods mentioned above: it is able to reconstruct not only the energy spectrum of a target but in addition to that, the spectral phase of the target as well. This is achieved by a new approach, to use a single line resonance foil, such as stainless steel enriched in ^{57}Fe , which is attached to an oscillating piezo. The oscillation leads to the generation of sidebands. One of the sidebands is now used as an analyzer, similarly

to the late-time integration method, which uses an analyzer on a Doppler-drive. The crucial advantage, of the Oscillation-drive method is the access and controllability of the oscillation offset φ_0 of the piezo movement (see formula (2.64)). In chapter 3 it has been shown that φ_0 can be used as an additional, controllable degree of freedom which can control the shape of the waveform in the time as well as in the energy domain.

This is exploited in the Oscillation-drive method, which results in the advantage to reconstruct the energy spectrum *plus* the spectral phase of the target.

In the following, a theoretical model for the Oscillation-drive is developed. In the first section, the starting point will be an approximation, which is already known from eg. the late-time integration method, but here utilized in a novel way. For the theoretical model, at first a simplified system is used to learn the basic principle of the Oscillation-drive. Based on this, the full system is considered in the next section. This leads to perturbing contributions to the desired signals. This problem is solved by a frequency-based filtering method, which finally gives the same result as for the simplified system. To confirm the theoretical predictions, the numerical implementation of the Oscillation-drive is presented. This is used in the last section, where two example simulations are presented.

4.1. Theoretical Model

In this section a theoretical model for the Oscillation-drive is developed. It starts with a general description of the setup, followed by the introduction of the fundamental approximation the Oscillation-drive is based on. This is followed by a first model using a simplified system. The obtained knowledge is then used to derive a model for the full system.

The setup of the Oscillation-drive is depicted in figure 4.1. The incoming X-ray pulse first hits the analyzer foil, mounted on an oscillating piezo. After this, the scattered pulse hits the target. The latter is mounted on a Doppler-Drive, which shifts its resonance frequency by S . After passing both foils, the signal is detected by an avalanche photo diode (APD). In the following chapter, all formulas with a hat (e.g. $\hat{R}(\Delta)$) will denote a quantity in the energy space, whereas all formulas without a hat (e.g. $R(t)$) will denote a quantity in the time space.

The incident radiation considered in this derivation are hard X-rays, originating from a synchrotron facility. The electrical field of the incoming pulse will be denoted as $E_0(t)$. Due to the very short pulse duration of synchrotron radiation (for example 44 ps at PETRA III), the pulse envelope can be described as a δ -function [28].

The analyzer foil is a single line resonance foil, (e.g. a stainless steel foil enriched with ^{57}Fe), which is mounted on an oscillating piezo. Its spectral response function $\hat{R}_{\text{Osc}}(\Delta)$

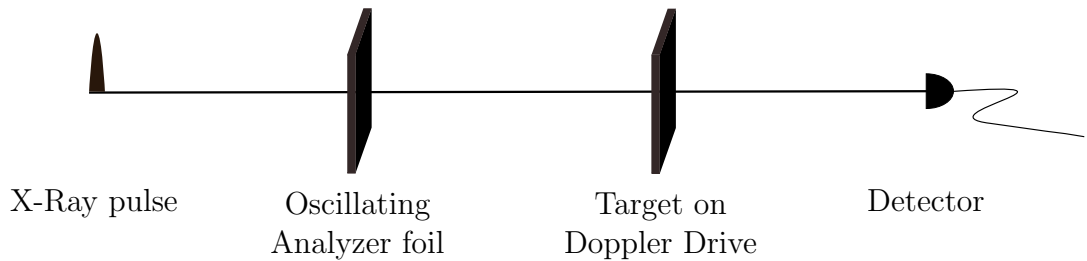


Figure 4.1.: Schematic setup used for the developed method. The envelope of the X-Ray pulse can be described as a δ -pulse in time. It first hits the analyzer foil, which is mounted on a piezo oscillating with the frequency ω_p . Next the target, which is to be examined, is mounted on a Doppler-Drive shifting the resonance by the value S . After passing those two foils, the signal is detected by an avalanche-photo diode (APD).

has been derived in chapter 2.2, see equation (2.68).

The target foil is mounted on a Doppler-drive, which moves with a constant velocity v_D . This results in a constant shift of the resonance frequency, described by $S = \hbar\omega_0 \frac{v_D}{c}$, where c denotes the speed of light in vacuum and \hbar the reduced Planck constant. The spectral response of the target will be denoted as $\hat{R}_T(\Delta)$. Finally, the signal is measured by avalanche photo diodes (APD) as a function of time. Furthermore, the oscillation frequency of the piezo ω_p and the offset of the oscillation φ_0 are recorded (compare with equation (2.64)).

In figure 4.2, the energy spectra of the analyzer and of the target are plotted. The resonance frequency of the target is shifted by S relative to the resonance frequency of the analyzer. The latter is equal to the frequency of the zeroth order sideband. However, in the figure the detuning is shifted such, that it is zero at the resonance frequency of the analyzer. This is equal to the case where the analyzer is shifted by S instead of the target. In the following, the reason for this behavior is explained.

In the theoretical model, it is not possible to give an expression for the for spectral response function of the target. This is obvious, since the target is unknown. Hence for the target there is no formula, the shift could be added to. At first glance, the solution would be to add it simply to the argument of the target, i.e. $\hat{R}_T(\Delta - S)$. However, this would lead to a wrong prediction of the behavior, because it is known, that two resonance dips which have the distance S in the energy domain, lead to oscillations in the time domain, as described by e^{iSt} . And if the shift would be added to the argument, this oscillation would not occur within the formula. The reason why the setup in figure 4.1, is not designed directly in a way that the analyzer is shifted by S , is that the experimental realization of such an arrangement would be significantly more complicated.

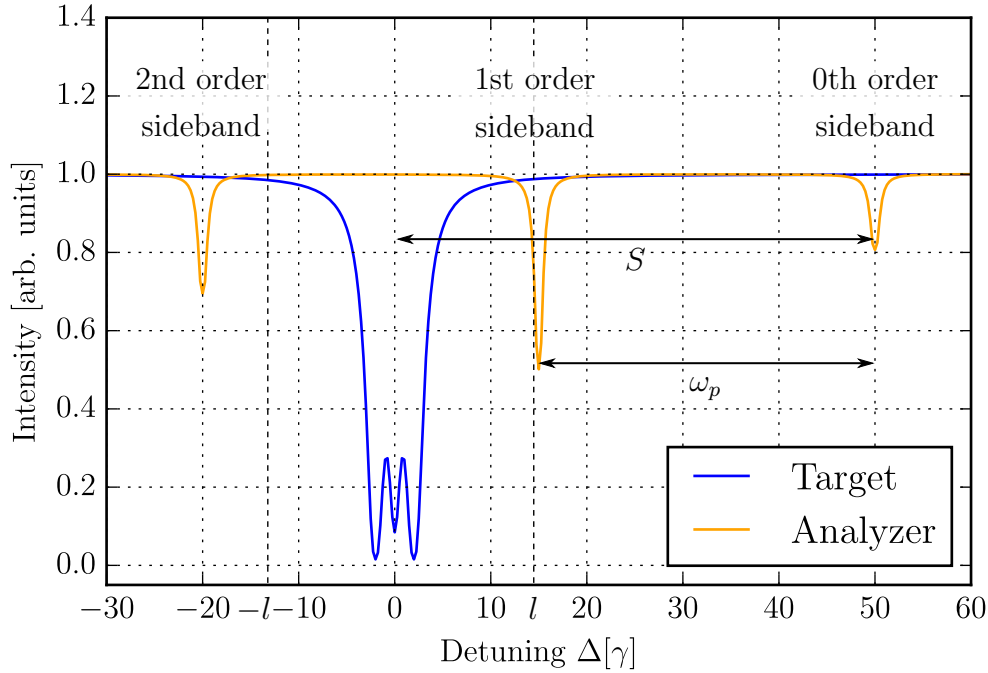


Figure 4.2.: Spectra of the two foils in the energy domain. The resonance frequency of the target is shifted by S , relatively to the zeroth order sideband of the analyzer. For the theoretical model it is necessary that the detuning axis is zero at the resonance frequency of the target. Therefore, the axis is shifted such the analyzer is shifted by S instead of the target. All sidebands, except for the zeroth order, are changing its positions with the variation of the piezos oscillation frequency ω_p . Hence, the first order sideband can be used to scan the target. The range where the spectral response of the target is unequal to one, is described as $-l$ to l . Based on this, the value of S have to be chosen. If the value of S is too small, the second order sideband would scan the sample at the same time but on the wrong side of the resonance, which would prevent the reconstruction.

The position of all sidebands of order $n \geq 1$ depends on ω_p in the following way. Their distance to the resonance frequency of the analyzer is equal to $n\omega_p$.

An important parameter to describe the target is the parameter l , which describes the range where the absolute square of the transmission function of the target is unequal to zero,

$$|\hat{R}_T|^2 = \begin{cases} \neq 1, & \text{for } -l \leq \Delta \leq l \\ 1, & \text{otherwise} \end{cases}. \quad (4.3)$$

S and ω_p are chosen such that the first order sideband scans the target by changing its spectral position via ω_p . This means, that the first sideband has to move over the whole range from l to $-l$.

Therefore the range ω_p has to cover is $\omega_p \in [S - l, S + l]$. Furthermore, S has to be large enough to ensure, that for small values of ω_p the second and the first order sideband scan the target at the same time, that is $S - 2\omega_p < -l$ for all values of ω_p .

With these considerations, the main principle of the Oscillation-drive can be explained. The sideband of the first order is moved in the range of $-l$ to l by variation of ω_p . The signal is measured by the APDs as a function of the time t and ω_p . For every value of ω_p , a time spectrum is measured now. So far this is similar to the principle of the late time integration. The difference is, that the signal is measured in dependence of φ_0 . This three dimensional data can be used to reconstruct the energy spectrum as well as the phase in the energy domain. The details of this method will be derived in the following.

The electrical field at the detector can now be described by a multiplication of the electrical field of the input, and the responses of the oscillating and the target foil. Bringing this now together, using the equation (2.68) from section 2.2, the electrical field at the detector reads,

$$\begin{aligned} \hat{E}_D &= \hat{E}_0(\Delta) \cdot \hat{R}_{\text{Osc}}(\Delta) \cdot \hat{R}_T(\Delta) \\ &= \hat{R}_T(\Delta) - \sum_{n=-\infty}^{\infty} \underbrace{J_n(p) e^{in\varphi_0 - ip \sin(\varphi_0)}}_{\alpha_n} \underbrace{\left(1 - e^{\frac{-ib_A}{\Delta - S + n\omega_p + i\frac{\gamma_A}{2}}} \right)}_{\hat{R}_A^n(\Delta, \omega_p)} \cdot \hat{R}_T(\Delta). \end{aligned} \quad (4.4)$$

Here, b_A and γ_A denote the values of b and γ for the analyzer. Remember that $E_0(\Delta) \approx 1$, since the incoming pulse can be described as a δ -function in the time domain. The abbreviations α_n and $\hat{R}_A^n(\Delta)$ will often be used in the following, wherefore they have been introduced here. $\hat{R}_T(\Delta)$ is unknown. Here it is possible to see, that the shift S is added to the formula of the analyzer as described above. This equation is the starting point of the theoretical model.

So far, the setup of the Oscillation-drive has been described. In figure 4.2, the main principal of this method could be seen. By variation of ω_p , the first sideband is moved over the relevant range of the target to be measured ($-l$ to l). Furthermore, it have to be ensured that the first and the second sideband are not within this range at the same time. Otherwise, they would sample the target, at the same time, what would destroy the reconstructions. For every value of ω_p , the APDs measure a time spectrum. Furthermore, the value of φ_0 is measured. This results in a three dimensional data grid (t, ω_p, φ_0) which can be used to reconstruct the energy spectrum as well as the spectral phase of the target. The details on how to obtain this information from merely measuring the time spectrum and the phase offset φ_0 will be derived in the following.

4.1.1. Sensing Head Approximation

The method of the Oscillation-drive is based on the approximation, which will be introduced in this section. It allows to make a cross-link between the energy spectrum of the target and the measured signal in the time domain. The approximation performed in the following is well known, e.g. from [45].

As a starting point, one summand, of the sum in equation (4.4) is considered, which reads,

$$\alpha_n \underbrace{\left(1 - e^{\frac{-ib_A}{\Delta - S + n\omega_p + i\frac{1-\gamma_A}{2}}} \right)}_{\hat{R}_A(\Delta, \omega_p)} \cdot \hat{R}_T(\Delta). \quad (4.5)$$

As a short reminder, in section 2.2 has been found, that each n stands for one sideband. This means that the equation above, describes the multiplication of the n -th sideband with the spectrum of the target.

However, this has to be specified in more detail: $\hat{R}_A(\Delta, \omega_p)$, is not exactly the n th sideband, since the unity term in front of the sum is missing. To understand what \hat{R}_A describes instead, a closer look is taken on equation (2.68). The unity term creates a baseline, which is independent of Δ . The expression $\exp \frac{-ib_A}{\Delta - S + n\omega_p + i\frac{1-\gamma_A}{2}}$ represents a narrow peak, which is converted into a dip by subtracting it from the baseline. These dips constitute what has been called sidebands so far. Therefore $\hat{R}_A^n(\Delta, \omega_p)$ describes a narrow peak at $\Delta = S - n\omega_p$ and converges quickly to zero around that value. Therefore the product of $\hat{R}_A^n(\Delta, \omega_p)$ and $\hat{R}_T(\Delta)$ in equation (4.5), can only be nonzero around $\Delta \approx S - \omega_p$. This is used now to expand $\hat{R}_T(\Delta)$ around $\Delta \approx S - \omega_p$. However, the phase of the target has to be treated more thoroughly because of two reasons. The first is, that it changes fast. The second is, that the phase of a complex value carries more information whilst doing a Fourier-transformation [57]. Therefore, the phase is expanded up to the first order [45]. The whole approximation then reads,

$$\hat{R}_T(\Delta) \approx \hat{R}_T(S - \omega_p) e^{i\tau(\Delta - S + \omega_p)}, \quad (4.6)$$

$$\text{with } \tau = \left. \frac{\partial \arg(\hat{R}_T(\tau))}{\partial \Delta} \right|_{\Delta=S-\omega_p}. \quad (4.7)$$

Inserting this into equation (4.4), it is now possible to do a Fourier-transformation. The transformation is analogous to the transformation in 2.1.3 and [45]. The outcome

reads,

$$E_D(t) \approx R_T(t) + \sum_{n=-\infty}^{\infty} \alpha_n \hat{R}_T(S - n\omega_p) e^{-i(S - n\omega_p)t} \underbrace{(-1) \cdot \sqrt{\frac{2\pi b}{t - \tau}} e^{-\frac{\gamma}{2}(t - \tau)} J_1\left(2\sqrt{b(t - \tau)}\right) \theta(t - \tau)}_{A(t, \tau)}. \quad (4.8)$$

This is a very useful expression now, because it describes the dynamic in the time domain but regardless of that $\hat{R}_T(S - n\omega_p)$ is the complex energy spectrum at $(S - n\omega_p)$. Therefore this expression gives a first hint at how it is possible to reconstruct the energy spectrum using a measurement made in the time domain. A physical interpretation of the approximation is the following. In the energy domain, each part n of the sum describes a sideband multiplied with the target spectrum. This means that the multiplication of the sideband with the target is like the sideband samples the target. In other words, each peak of the sideband works as a sensing head for the target. It returns the complex spectrum of the target at the position of the sideband. Therefore the sidebands can scan the target. In the following the summarized expression $A(t, \tau)$ will be used. It describes the response of the resonantly scattered part, i.e. the part without the δ -function in equation (2.41), of the analyzer foil in the time domain but delayed by τ .

4.1.2. Single Sideband Approximation

The previous section ended with formula (4.8) which approximates the electric field at the detector in the time domain. The special feature of this approximation is that it can be understood, like the sidebands scanning the target.

The setup is designed in a way that the first sideband scans the relevant range of the target. All other sidebands give additional contributions, which make the signal more complicated. To gain an insight how the system behaves in principle, in this section only the sideband with $n = 1$ is taken into account and all other sidebands are neglected. Therefore, equation (4.8) reduces to a single term.

The APDs used for nuclear forward scattering only measure the intensity of the signal, which is proportional to the absolute square of the electric field at the detector,

$$|E_D(t)|^2 = |R_T(t)|^2 + \underbrace{|A(t, \tau)|^2 |\alpha_1 \hat{R}_T(S - \omega_p)|^2}_{E_{Sq}(t)} + 2 \operatorname{Re} \left(\underbrace{A(t, \tau) \alpha_1^* \hat{R}_T^*(S - \omega_p) e^{i(S - \omega_p)t} R_T(t)}_{E_R(t)} \right). \quad (4.9)$$

As already mentioned the idea to use a analyzer foil to sample the target foil is not new. It has been employed for the late time integration method as well. The difference there is, that the resonance frequency of the analyzer foil is shifted by using a Doppler-drive. Th Oscillation-drive uses the first sideband, which is shifted by the oscillation frequency ω_p of the piezo.

Those oscillations however, offer an additional degree of freedom, the offset of the oscillation φ_0 . As already shown in chapter 2.2 and 3, φ_0 offers the possibility to control the waveform in time and energy domain simultaneously. Furthermore, in section 3.2 φ_0 causes an exchange of the real and the imaginary of the response function in the energy domain.

This feature is used for the Oscillation-drive, to extract the desired information from the time spectrum.

A further finding of chapter 3 was, that the intensity varies periodically with respect to φ_0 . This makes it predesignated to be analyzed using a Fourier transformation. Therefore, in the following a Fourier transformation with respect to φ_0 will be performed. The frequency that φ_0 oscillates with will be denoted by f .

In the following the transformation of the individual terms of equation (4.9) are performed.

$|R_T(t)|^2$ has no dependency on φ_0 , therefore it can be treated as a constant in the Fourier transformation what leads to,

$$\mathcal{F}(|R_T(t)|^2; \varphi_0, f) = \sqrt{2\pi}\delta(f)|R_T(t)|^2. \quad (4.10)$$

The only part in $E_{Sq}(t)$ which has a dependency on φ_0 is α_1 . Taking the absolute square of it, it becomes, $\alpha_1\alpha_1^* = J_1^2(p)e^{i\varphi_0-ip\sin(\varphi_0)}e^{-i\varphi_0+ip\sin(\varphi_0)} = J_1^2(p)$, which is independent of φ_0 as well. Therefore its Fourier transform is,

$$\mathcal{F}(|E_{Sq}(t)|^2; \varphi_0, f) = \sqrt{2\pi}\delta(f)|E_{Sq}(t)|^2. \quad (4.11)$$

For $E_R(t)$ the Fourier transform becomes more complicated. First the real part is rewritten, using the notation for any complex number z , that $\text{Re}(z) = \frac{1}{2}(z + z^*)$. Furthermore, the Jakobi-Anger relation (2.66) is used to rewrite it as,

$$E_R(t) = A(t, \tau)J_1(p)\frac{1}{2} \sum_{m=-\infty}^{\infty} J_m(p) \cdot \left[e^{i\varphi_0-im\varphi_0+i(S-\omega_p)t} \hat{R}_T^*(S - \omega_p)R_T(t) + c.c. \right]. \quad (4.12)$$

In this form the Fourier transformation can be calculated,

$$\begin{aligned} \mathcal{F}(E_R(t); \varphi_0; f) = & J_1(p)A(t, \tau) \sum_{m=-\infty}^{\infty} J_m(p)\sqrt{2\pi} \\ & \cdot \left[e^{i(S-\omega_p)t} \hat{R}_T^*(S - \omega_p) R_T(t) \delta(f - m + 1) \right. \\ & \left. + e^{-i(S-\omega_p)t} \hat{R}_T(S - \omega_p) R_T^*(t) \delta(f + m - 1) \right]. \end{aligned} \quad (4.13)$$

Inspecting now all parts of the Fourier transformation, it can be seen that only (4.13) contributes to the Fourier spectrum for $f \neq 0$. It is important to note, that the Fourier transform actually consists of a sum of δ -functions, each weighted with a prefactor. Therefore, the spectrum has only contributions if f is an integer. Hence the Fourier transformation can be used as a filter, to filter out $E_R(t)$ from the rest of the signal. This is done by setting everything except for the part $f = \pm 1$ to zero and performing the inverse transformation. This gives,

$$\begin{aligned} |\tilde{E}_D(t)|^2 = & \tilde{E}_R(t) \\ = & J_1(p)A(t, \tau) \left[e^{-i(S-\omega_p)t} \hat{R}_T(S - \omega_p) R_T^*(t) (J_0(p)e^{-i\varphi_0} + J_2(p)e^{i\varphi_0}) + c.c. \right]. \end{aligned} \quad (4.14)$$

The tilde over $\tilde{E}_D(t)$ and $\tilde{E}_R(t)$ denote that the equations have been truncated in Fourier space. Truncated means here, that all terms which were not desired have been set to zero.

The expansion of the real-part is now inverted.

Furthermore, parts within the real part can be rewritten as $R_T(t) = |R_T(t)|e^{i\theta(t)}$ and $\hat{R}_T(S - \omega_p) = |\hat{R}_T(S - \omega_p)|e^{i\hat{\theta}(S - \omega_p)}$. This is used to extract the absolute values from the real part,

$$\begin{aligned} |\tilde{E}_D(t)|^2 = & 2J_1(p)A(t, \tau)|R_T(t)| \cdot \\ & |\hat{R}_T(S - \omega_p)| \cdot \text{Re} \left[e^{i(\hat{\theta}(S - \omega_p) - \theta(t) - (S - \omega_p)t)} \cdot (J_0(p)e^{-i\varphi_0} + J_2(p)e^{i\varphi_0}) \right]. \end{aligned} \quad (4.15)$$

At this point, it is not possible to simplify the equation in a useful way. However, it is possible to use a trick. Fortunately, p is a parameter, which can be chosen in an experiment. Hence, we set $p = p_0 = 2.4$ which implies that $J_0(2.4) \approx 0$. This helps to simplify the equation again,

$$\begin{aligned} |\tilde{E}_D(t)|^2 = & 2J_1(p_0)J_2(p_0)A(t, \tau)|R_T(t)| \cdot |\hat{R}_T(S - \omega_p)| \cdot \\ & \cos \left(\varphi_0 + \hat{\theta}(S - \omega_p) - \theta(t) - (S - \omega_p)t \right). \end{aligned} \quad (4.16)$$

Introducing the shortcuts,

$$B(t, \tau, p) = 2J_2(p_0)J_1(p_0)A(t, \tau) \cdot |E_T(t)|, \quad (4.17)$$

$$C(\omega_p) = |\hat{R}_T(S - \omega_p)|, \quad (4.18)$$

$$a(t, \omega_p) = \hat{\theta}(S - \omega_p) - \theta(t) - (S - \omega_p)t, \quad (4.19)$$

the equation can be rewritten as,

$$|\tilde{E}_D(t, \omega_p, \varphi_0)|^2 = B(t, \tau, p_0) \cdot C(\omega_p) \cdot \cos(\varphi_0 + a(\omega_p, t)). \quad (4.20)$$

This is a useful result. The edited signal of the measurement is now a function which depends on the absolute value of the target spectrum as well as on the spectral phase of the target. Now a method is needed to extract both values from this equation.

A big advantage of equation (4.20) is that the phase and the absolute value are separated into the amplitude and to the offset of the cosine. Therefore, this can be used to extract them separately from the equation. The dependency on ω_p , t and φ_0 in equation (4.20) is explicitly given there on purpose, to indicate, that the recorded data has those three dimensions. If t and ω_p are fixed in this equation, the resulting function is a pure cosine which is weighted by the amplitude $B(t, \tau, p_0)C(\omega_p)$, oscillates with φ_0 and has the offset $a(t, \omega_p) = \hat{\theta}(S - \omega_p) - \theta(t) - (S - \omega_p)t$. For each pair of ω_p and t , a function with of the shape $f(\varphi_0) = D \cos(\varphi_0 + a)$ is fitted to the data. This can be done for each pair of ω_p and t of the measurement. This is illustrated in figure 4.3. Here, an advantage of the Oscillation-drive becomes clear. Due to the φ_0 dependency, it is possible to get access to the amplitude $D(t_1, \omega_p^1)$. If the variation in φ_0 direction would not be there, it would be possible to access the intensity at $\varphi_0 = 0$, only. This value is depicted in the figure as $I(\varphi_0 = 0)$. Note, that in the figure I is indicated as a negative value. However, in a measurement, the absolute of I would be the measured value. Moreover, $a(t, \omega_p)$ would not be accessible as well. Therefore this provides an intuitive picture, of how it is possible to extract more information by exploiting φ_0 .

The amplitude D of the fit is equal to $D = B(t, \tau, p_0)C(\omega_p)$. At a first glance, it looks like D is proportional to the absolute value of the energy spectrum at ω_p , with a proportionality factor, which depends on t, τ and p_0 , which are all constant for one fit. However, looking at equation (4.7), one can see, that τ depends on ω_p as well. The dependence of τ on ω_p is small, however, such that this effect can be neglected.

This means, that performing this fit procedure for a fixed time and all values of ω_p at this time, one should get a signal which is proportional to the absolute value of the energy spectra \hat{R}_T .

The offset a of the fit is directly equal to $a(t, \omega_p) = \hat{\theta}(S - \omega_p) - \theta(t) - (S - \omega_p)t$. At a fixed time t_0 , this is a function which depends on the spectral phase at $S - \omega_p$ but with an linear increase of $\omega_p t_0$ and some constant offset like $-S t_0$ and $\theta(t_0)$. Fortunately S

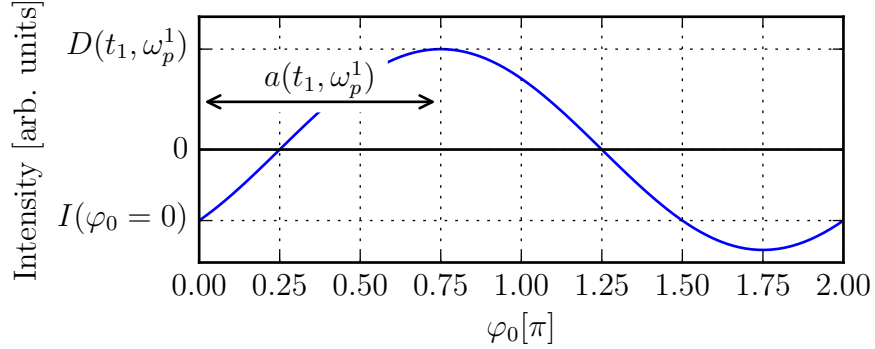


Figure 4.3.: Exemplary illustration of the data as a function of φ_0 . For each combination of t and ω_p , the final data describes a harmonic oscillation in φ_0 direction. By fitting a function $f(\varphi_0) = D \cos(\varphi_0 + a)$ to the data, it is possible to extract the numerical values of $a(t_1, \omega_p^1)$ and $D(t_1, \omega_p^1)$ from the data. The advantage of φ_0 as an extra degree of freedom becomes visible. Without the additional information in φ_0 direction, it would be possible to determine only $|I(\varphi_0 = 0)|$.

and ω_p are values which are known, therefore they can be subtracted. The remaining signal is $\hat{\theta}(S - \omega_p) - \theta(t_0)$, which is the spectral phase with a constant offset.

To sum this up, the starting point at the beginning of this section, was equation (4.8) resulting from the sensing head approximation. To learn how the system works in principle, equation (4.8) was reduced to a single line analyzer. After applying a frequency filter with respect to φ_0 using a Fourier transformation and the choice of $p = p_0 = 2.4$ the result was a cosine, oscillating with φ_0 . The offset and the amplitude can be determined via a fit, which provides the possibility to reconstruct the absolute of the energy spectrum and the phase of the energy spectrum.

4.1.3. Full System

In the previous section a theory to determine the phase and the absolute value of the spectrum in the energy domain for a system have been developed. For this only the $n = 1$ sideband have been taken into account. The method uses different frequency dependencies on φ_0 to extract the desired term out of the rest of the signal.

Practically, however, the oscillation of the analyzer foil creates a multiple of sidebands. Hence, the question arises, if this can be generalized to the full system, dropping the restriction of taking into account only one sideband. The additional sidebands lead to a much more complex signal with contributions which are not as straightforward to separate in the same way as before. However, it is possible to use a second filtering method,

to finally end up with the same signal as in the single line case. The methods to do so are presented in this section.

The first method to filter the signal is the same as before, that is doing a Fourier transformation with respect to φ_0 and filter out all contributions except for $f = \pm 1$. Even though the method is the same, the analytic calculation become more complicated due to the different contributions.

The second method to filter the signal is to use different frequency dependencies of the individual sidebands in time. Therefore it will be called t -filter. By use of another Fourier transformation it is possible to filter out the desired contribution. The remaining part is, equal to equation (4.20) and can be evaluated with the same methods as before.

These single steps are summed up in a flow chart diagram in figure 4.4. The single steps in the case of the full system as well as for the single line approximation are depicted there. For the case of the single line approximation, the dashed arrows have to be followed, the solid lines stand for the steps using the full system. Furthermore, the principle of the filter are indicated, as well as the principle of the final reconstruction.

φ_0 -filter: Fourier Transformation and Truncation With Respect to φ_0

Starting point is again equation (4.8). Taking the absolute square of it yields,

$$\begin{aligned}
 |E_D(t)|^2 = & |R_T(t)|^2 + \\
 & \underbrace{|A(t, \tau)|^2 \left| \sum_{n=-\infty}^{\infty} \alpha_n e^{-i(S-n\omega_p)t} \hat{R}_T(S-n\omega_p) \right|^2}_{E_{Sq}} + \\
 & \underbrace{2 \operatorname{Re} \left[R_T(t) \sum_{n=-\infty}^{\infty} \alpha_n^* e^{i(S-n\omega_p)t} \hat{R}_T^*(S-n\omega_p) A(t, \tau) \right]}_{E_R}.
 \end{aligned} \tag{4.21}$$

As in the single line case, as a first step the Fourier transform with respect to φ_0 is performed. The first summand, $|R_T(t)|^2$ remains the same as in the simplified case and can be found in equation (4.10). The other two parts have to be treated more thoroughly. The only parts in E_{Sq} and E_R which depend on φ_0 are the combinations of α_n .

The start makes E_{Sq} . An expansion of the sum in E_{Sq} leads to $\alpha_m^* \alpha_n$ or its complex conjugate. To calculate the Fourier transform of E_{Sq} it is sufficient to calculate the Fourier transform of $\alpha_m^* \alpha_n$, since the rest is constant with respect to φ_0 . Hence, the Fourier transform of these terms is performed, which reads,

$$\mathcal{F}(\alpha_m^* \alpha_n; \varphi_0, f) = \sqrt{2\pi} J_n(p) J_m(p) \cdot \delta(n - m + f). \tag{4.22}$$

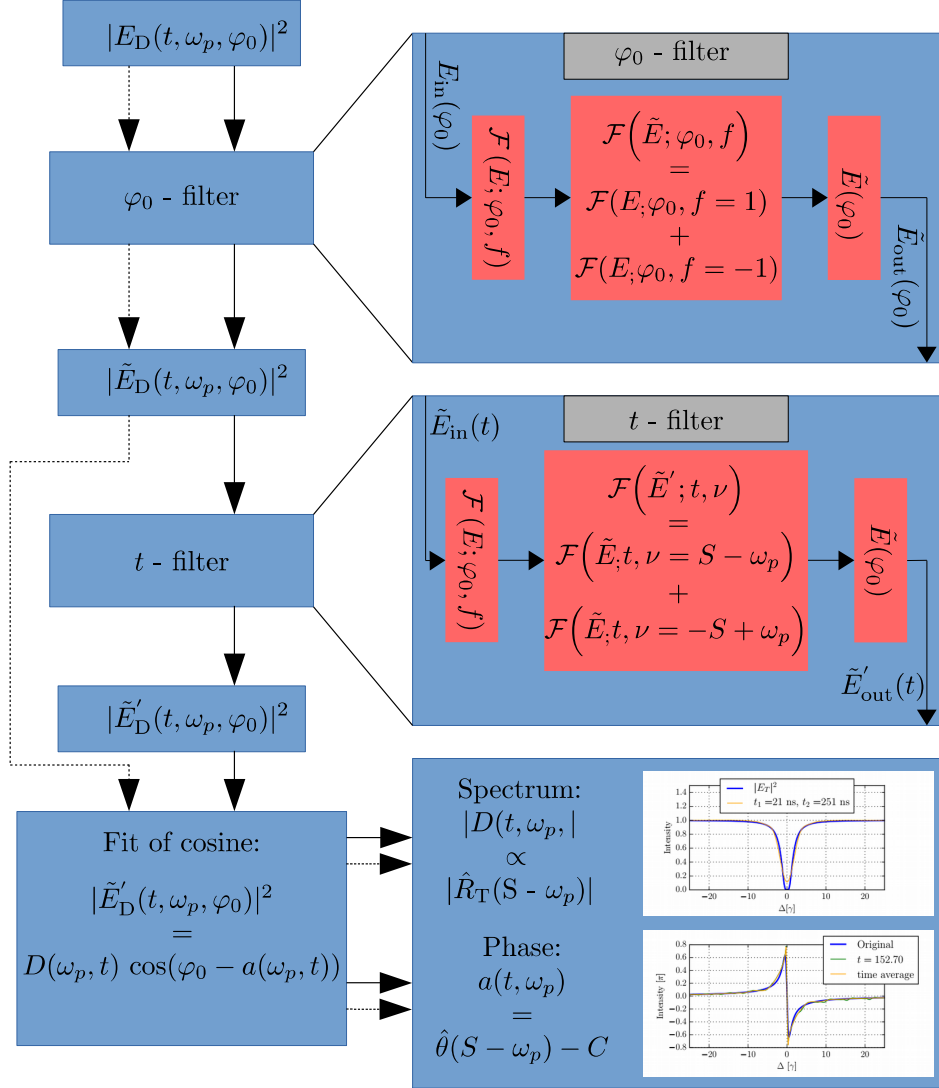


Figure 4.4.: Flow chart diagram of the Oscillation drive. Starting point are the measured data at the detector, which are proportional to the absolute square of the electric field. The arrows with the dashed line represent the steps of the single sideband approximation. The solid lines represent the steps of the full system. For the approximated case, the t -filter is not necessary. After the data of the full system has passed the t -filter, both systems can be described with exactly the same formula (in the text (4.39)). The first filter splits the data into their frequency components with respect to φ_0 . Next, the contributions of the frequencies $f = \pm 1$ are summed up and transformed back. This is indicated by the tilde. The t -filter has the same working principle. However, it uses the frequencies with respect to the time t . In the frequency space, the contributions of $\nu = \pm(S - \omega_p)$ are summed up and transformed back. This truncated data is indicated by a prime. To this data, a cosine, with respect to φ_0 is fitted. The fit amplitude D is used to reconstruct the spectrum, the offset a to reconstruct the complex phase.

This can be used to perform the Fourier transform of ES_q, which reads

$$\begin{aligned} \mathcal{F}(E_{\text{Sq}}; \varphi_0, f) = \sqrt{2\pi} \sum_{m=-\infty}^{\infty} \sum_{n=-\infty}^{\infty} J_n(p) J_m(p) |A(t, \tau)|^2 \hat{R}_{\text{T}}(S - n\omega_p) \\ \times \hat{R}_{\text{T}}^*(S - m\omega_p) e^{i\omega_p(n-m)t} \delta(n - m + f). \end{aligned} \quad (4.23)$$

The double sum in this equation, originates from the calculation of the absolute square.

For the real part, E_{R} , the only parts which depends on φ_0 are α_n and α_n^* , respectively. Hence, to calculate the corresponding Fourier transform of E_{R} , the Fourier transformation of α_n is needed. For this, alike, as in the single line case the Jakobi-Anger relation (2.66) is used. The resulting Fourier transform then reads

$$\mathcal{F}(\alpha_n; \varphi_0, f) = J_n(p) \sqrt{2\pi} \sum_{m=-\infty}^{\infty} J_m(p) \delta(f + n - m). \quad (4.24)$$

Now the real part in E_{R} is rewritten as $\text{Re}(z) = \frac{1}{2}(z + z^*)$. Using this and equation (4.24), the Fourier transform of E_{R} becomes,

$$\begin{aligned} \mathcal{F}(E_{\text{R}}; \varphi_0, f) = A(t, \tau) \sqrt{2\pi} \sum_{n=-\infty}^{\infty} \left[\right. \\ \hat{R}_{\text{T}}^*(S - n\omega_p) e^{+i(S-n\omega_p)t} R_{\text{T}}(t) J_n(p) \sum_{m=-\infty}^{\infty} J_m(p) \delta(f - n + m) + \\ \left. \hat{R}_{\text{T}}(S - n\omega_p) e^{-i(S-n\omega_p)t} R_{\text{T}}^*(t) J_n(p) \sum_{m=-\infty}^{\infty} J_m(p) \delta(f + n - m) \right]. \end{aligned} \quad (4.25)$$

Now, all parts of equation (4.21) are transformed with respect to φ_0 . Equivalent to the single-line approximation, the transformations are restricted to the contribution of $f = \pm 1$. This ensures, that the same term which leads to the result of the single line analysis is obtained, together with some additional contributions. The selection of the frequency $f = \pm 1$ can be done by expressing m through n . For this the constraints that, $n - m = \pm 1$ and $-n + m = \pm 1$, respectively, are used. The tilde in the following equations denotes that they have been restricted to $f = \pm 1$. This means that only the frequency of $f = \pm 1$ contributes. The reduced restricted equations read,

$$\mathcal{F}(|\tilde{E}_{\text{T}}|^2; \varphi_0, f) = 0, \quad (4.26)$$

$$\begin{aligned}
 \mathcal{F}(\tilde{E}_{\text{Sq}}; \varphi_0, f) = & \sqrt{2\pi} |A(t, \tau)|^2 \sum_{n=-\infty}^{\infty} J_n(p) J_{n-1}(p) \hat{R}_{\text{T}}(S - n\omega_p) \hat{R}_{\text{T}}^*(S - (n-1)\omega_p) \cdot \\
 & e^{+i\omega_p t} \delta(+1 + f) + \\
 & \sqrt{2\pi} |A(t, \tau)|^2 \sum_{n=-\infty}^{\infty} J_n(p) J_{n+1}(p) \hat{R}_{\text{T}}(S - n\omega_p) \hat{R}_{\text{T}}^*(S - (n+1)\omega_p) \cdot \\
 & e^{-i\omega_p t} \delta(-1 + f),
 \end{aligned} \tag{4.27}$$

$$\begin{aligned}
 \mathcal{F}(\tilde{E}_{\text{R}}; \varphi_0, f) = & A(t, \tau) \sqrt{2\pi} \sum_{n=-\infty}^{\infty} \left[\right. \\
 & \hat{R}_{\text{T}}^*(S - n\omega_p) e^{-i(S-n\omega_p)t} R_{\text{T}}(t) J_n(p) J_{n-1}(p) \delta(f-1) + \\
 & \hat{R}_{\text{T}}^*(S - n\omega_p) e^{-i(S-n\omega_p)t} R_{\text{T}}(t) J_n(p) J_{n+1}(p) \delta(f+1) + \\
 & \hat{R}_{\text{T}}(S - n\omega_p) e^{-i(S-n\omega_p)t} R_{\text{T}}^*(t) J_n(p) J_{n+1}(p) \delta(f-1) + \\
 & \left. \hat{R}_{\text{T}}(S - n\omega_p) e^{-i(S-n\omega_p)t} R_{\text{T}}^*(t) J_n(p) J_{n-1}(p) \delta(f+1) \right].
 \end{aligned} \tag{4.28}$$

The revers transformation can be performed straightforwardly, since the functions with respect to φ_0 are limited to δ -functions. Hence it can be done by replacing $\delta(f \pm 1)$ by $e^{\mp i\varphi_0}$ and removing the factor $\sqrt{2\pi}$. Doing so, the terms read,

$$\begin{aligned}
 \tilde{E}_{\text{Sq}}(t) = & |A(t, \tau)|^2 \cdot \\
 & \sum_{n=-\infty}^{\infty} \left[J_n(p) J_{n-1}(p) \hat{R}_{\text{T}}^*(S - n\omega_p) \hat{R}_{\text{T}}(S - (n-1)\omega_p) e^{i\omega_p t} e^{i\varphi_0} + \right. \\
 & \left. J_n(p) J_{n+1}(p) \hat{R}_{\text{T}}^*(S - n\omega_p) \hat{R}_{\text{T}}(S - (n+1)\omega_p) e^{-i\omega_p t} e^{-i\varphi_0} \right]
 \end{aligned} \tag{4.29}$$

and

$$\begin{aligned}
 \tilde{E}_{\text{R}}(t) = & \sum_{n=-\infty}^{\infty} \left[\hat{R}_{\text{T}}^*(S - n\omega_p) e^{i(S-n\omega_p)t} A(t, \tau) R_{\text{T}}(t) J_n(p) \right. \\
 & \left. [J_{n-1}(p) e^{-i\varphi_0} + J_{n+1}(p) e^{i\varphi_0}] + c.c. \right].
 \end{aligned} \tag{4.30}$$

In both sums, n can be interpreted as a variable numbering the sidebands. This means, if we want to describe an analyzer with all sidebands up to order N , we have to truncate

the sum such that it runs from $-N$ to N . Therefore the total edited signal is,

$$\tilde{E}_D(t) = \tilde{E}_{\text{Sq}}(t) + \tilde{E}_R(t). \quad (4.31)$$

Comparing this result with the one of the simplified system, the additional terms arising from the other sidebands can be seen. It is not possible to reduce this equations to a cosine like before. The reasons for this is that $\tilde{E}_{\text{Sq}}(t)$ is not zero anymore and that $\tilde{E}_R(t)$ is now a sum over all sidebands. The aim in the following is to find a way to isolate the term with $n = 1$ in equation (4.30).

t*- Filter: Fourier Transformation with Respect to *t

One thing all parts of equation (4.29) and (4.30) have in common are that they oscillate with respect to the time. However, each summand has a different frequency. This can be used to isolate the desired term. Therefore in the following an analysis of the different oscillation frequencies of the different terms is performed.

Equation (4.29) oscillates with a frequency of $S - \omega_p$. In equation (4.30) the frequencies which can be found are $S - n\omega_p$. As one can see from equation (4.15), which describes the single line case, it oscillates with $S - \omega_p$. Therefore the term oscillating with this frequency has to be isolated.

To split the remaining signal into their different frequencies it is necessary to do another Fourier transformation, but this time with respect to t . Unfortunately, $R_T(t)$ depends on t , but is not known. Therefore an analytical transformation is not possible. However, it is possible to Fourier transform only parts of the signal, and indicate the unknown parts by a symbol, to proceed with the analytic analysis. For this purpose the following symbols are defined,

$$\mathcal{F}(|A(t, \tau)|^2; t, \nu) = \widehat{|A|^2}(\nu), \quad (4.32)$$

$$\mathcal{F}(A(t, \tau)R_T(t); t, \nu) = \widehat{AR_T}(\nu). \quad (4.33)$$

To use them within a Fourier transformation, the Fourier-convolution theorem is used [39]. Because the transformation does not use the whole signal, which is measured at the detector, the corresponding variable to t will be called ν instead of Δ to avoid confusion with the energy spectrum.

With these, the transformation yields,

$$\mathcal{F}(\tilde{E}_{\text{Sq}}; t, \nu) = \sqrt{2\pi} \sum_{n=-\infty}^{\infty} \left[\hat{R}_{\text{T}}^*(S - n\omega_p) \hat{R}_{\text{T}}(S - (n-1)\omega_p) e^{-i\varphi_0} \left(\widehat{|A|^2} * \delta(\nu - \omega_p) \right) + \hat{R}_{\text{T}}^*(S - n\omega_p) \hat{R}_{\text{T}}(S - (n+1)\omega_p) e^{i\varphi_0} \left(\widehat{|A|^2} * \delta(\nu + \omega_p) \right) \right] \quad (4.34)$$

$$\mathcal{F}(\tilde{E}_{\text{R}}; t, \nu) = \sqrt{2\pi} \sum_{n=-\infty}^{\infty} \left[\hat{R}_{\text{T}}^*(S - n\omega_p) J_n(p) \cdot \left[\widehat{AR}_{\text{T}}(\nu) * \delta(\nu - (S - n\omega_p)) \right] \right. \\ \left. [J_{n-1}(p) e^{-i\varphi_0} + J_{n+1}(p) e^{i\varphi_0}] + \hat{R}_{\text{T}}(S - n\omega_p) J_n(p) \cdot \left[\widehat{AR}_{\text{T}}^*(\nu) * \delta(\nu + (S - n\omega_p)) \right] \right. \\ \left. [J_{n-1}(p) e^{i\varphi_0} + J_{n+1}(p) e^{-i\varphi_0}] \right]. \quad (4.35)$$

The star (*) denotes a convolution of the two functions. Therefore, in ν -space the result is a series of δ -peaks, convoluted with the Fourier transform of $|A(t, \tau)|^2$, $A(t, \tau)R_{\text{T}}(t)$ and $A(t, \tau)R_{\text{T}}^*(t)$, respectively. This is a good result, because it means that the contributions of each frequency and therefore the contributions of the different sidebands are separated in ν space.

The positions of the peaks in ν -space however, is not intuitively clear. Hence in the following, they are analyzed more thoroughly. The frequencies occurring in equation (4.34) are, $\nu = \pm\omega_p$, which are independent of n . The frequencies occurring in equation (4.35), are $\nu = \pm(S - n\omega_p)$. In the following, only frequencies up to order $n = 2$ are going to be considered. The reason for this is, that for increasing n , the peaks move closer to the edge of the spectrum in ν -space. Therefore they are not relevant for the following consideration. To sum it up in a clear way, the three, respectively six peaks, taking into account the plus and minus peak, considered now are,

1. $\nu_{\text{p1}}^{\pm} = \pm\omega_p$,
2. $\nu_{\text{p2}}^{\pm} = \pm(S - \omega_p)$ and
3. $\nu_{\text{p3}}^{\pm} = \pm(S - 2\omega_p)$,

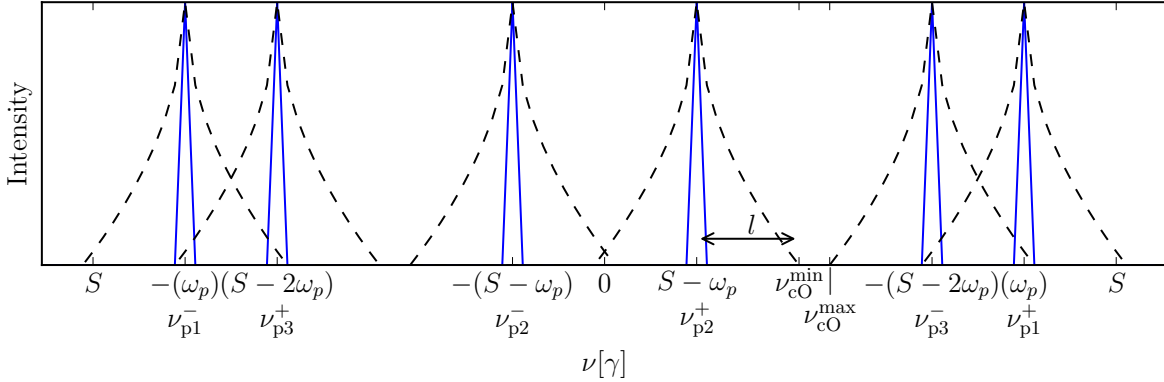


Figure 4.5.: Positions of the peaks of equation (4.35) and (4.34), up to order $n = 3$ in ν space. The broadening of the peaks due to the convolution with $|\widehat{A}|^2(\nu)$ and $\widehat{AR}_T(\nu)$, respectively, is indicated by the black dashed lines. l denotes the maximal estimated width due to the convolution. Therefore, the cutting can be done somewhere between the point where peak two became zero and the point where peak number three starts to rise. These two points are denoted by ν_{cO}^{\min} and ν_{cO}^{\max} . The subscript cO stand for “cutOff”.

where the first two peaks refer to \tilde{E}_{Sq} and the second to fourth to \tilde{E}_{Re} . The peaks are plotted in figure 4.5. From the simplified model with just one sideband, it is known that the contribution of the first sideband oscillates with a frequency of $S - \omega_p$ in time. This can be seen in equation (4.15). Therefore, the peaks ν_{p2}^{\pm} have to be isolated.

Considering only the delta peaks, they can be separated easily. However, it turned out that every peak is convoluted with the Fourier transform of $|A(t, \tau)|^2$, $A(t, \tau)R_T(t)$ and $A(t, \tau)R_T^*(t)$, respectively. The convolution leads to a broadening of the peaks, which is indicated by the dashed lines in figure 4.5 .

The problem is now, that R_T is not known. Therefore, it is not possible to give an analytical expression for the width of $\widehat{AR}_T(\nu)$. If its width is too large, this could lead to an overlap of the different peaks. As a consequence, they cannot be separated.

In a later numerical analysis it is shown that this is possible under certain conditions, which will be explained in section 4.2.

For now, it is assumed that this problem can be solved, to proceed with the analytical analysis. The actual task is to isolate the contribution of the first sideband to the signal. For this, the peaks with frequency $\pm(S - \omega_p)$ has to be identified and isolated, which means that it is kept, and the rest of the spectrum is set to zero. The term referring to the desired peaks is the part with $n = 1$ in the sum in equation (4.35). In

this analytical analysis, it is assumed, that the isolation works perfectly. For details on the corresponding numerical implementation, see section 4.2.1. Therefore all other contributions are set to zero and this part is the only one remaining in this equation. Equation (4.34) is set to zero in total, because its δ -peaks are at a frequency of $\pm(\omega_p)$. The remaining part is,

$$\begin{aligned} \mathcal{F}\left(\tilde{E}'_{\text{R}}; t, \nu\right) = & \sqrt{2\pi} \left[\hat{R}_{\text{T}}^*(S - \omega_p) J_1(p) \cdot \left[\widehat{AR}_{\text{T}}(\nu) * \delta(\nu - (S - \omega_p)) \right] \cdot \right. \\ & \left. [J_0(p)e^{-i\varphi_0} + J_2(p)e^{i\varphi_0}] + \right. \\ & \hat{R}_{\text{T}}(S - \omega_p) J_1(p) \cdot \left[\widehat{AR}_{\text{T}}^*(\nu) * \delta(\nu + (S - \omega_p)) \right] \cdot \\ & \left. [J_0(p)e^{i\varphi_0} + J_2(p)e^{-i\varphi_0}] \right]. \end{aligned} \quad (4.36)$$

The prime on \tilde{E}'_{R} indicates, that it has been truncated in ν -space. The revers transformation can be done easily now, by replacing $\delta(\nu \pm (S - \omega_p))$ with $e^{\mp i(S - \omega_p)t}$, and removing the heads on $\widehat{AR}_{\text{T}}(\nu)$ as well as the factor $\sqrt{2\pi}$. This yields for the measured signal,

$$\begin{aligned} |\tilde{E}'_{\text{D}}(t)|^2 = & \hat{R}_{\text{T}}^*(S - \omega_p) J_1(p) \cdot A(t) R_{\text{T}}(t) e^{i(S - \omega_p)t} \cdot \\ & [J_0(p)e^{-i\varphi_0} + J_2(p)e^{i\varphi_0}] + c.c. \end{aligned} \quad (4.37)$$

Writing the complex conjugated again as a real part and using $z = |z|e^{i \arg(z)}$, with z being a complex number, the equation can be written as,

$$\begin{aligned} |\tilde{E}'_{\text{D}}(t)|^2 = & 2J_1(p)A(t, \tau)|R_{\text{T}}(t)| \cdot \\ & |\hat{R}_{\text{T}}(S - \omega_p)| \cdot \text{Re} \left[e^{i(\hat{\theta}(S - \omega_p) - \theta(t) - (S - \omega_p)t)} \cdot (J_0(p)e^{-i\varphi_0} + J_2(p)e^{i\varphi_0}) \right]. \end{aligned} \quad (4.38)$$

This is now *exactly* the same equation as (4.15) at the end of the section without simplification. Therefore, with the choice of $p = p_0 = 2.4$ it can be written as well as,

$$|\tilde{E}_{\text{D}}(t)|^2 = B(t, \tau, p) \cdot C(\omega_p) \cdot \cos(\varphi_0 + a(\omega_p, t)), \quad (4.39)$$

with the abbreviations,

$$B(t, \tau, p) = 2J_2(p_0)J_1(p_0)A(t, \tau) \cdot |E_{\text{T}}(t)|, \quad (4.40)$$

$$C(\omega_p) = |\hat{R}_{\text{T}}(S - \omega_p)|, \quad (4.41)$$

$$a(t, \omega_p) = \hat{\theta}(S - \omega_p) - \theta(t) - (S - \omega_p)t. \quad (4.42)$$

This is a useful result. Because it shows that it is possible to isolate the signal originating from the first sideband of the analyzer and the target, from the signal of the whole system. In other words, the signal of the complete system can be reduced to the essential part, which contains all information needed to reconstruct the spectra and the phase of the target. This represents a powerful theoretical insight with practical potential. In order to confirm its practical and numerical feasibility, the numerical implementation is discussed in the following section.

4.2. Numerical Implementation

In the previous section a theory of the oscillation drive to reconstruct the spectrum and the phase of an unknown target have been developed. The theory was first derived for a special case of an approximated single line analyzer. Later this result could be generalized taking into account all sidebands of the analyzer. However, some of the calculations could not be performed analytically but have been sketched in the analytical analysis. Therefore, to confirm the practical feasibility of this theory, it is desired to simulate it. In this section a numerical implementation is required, which is discussed in this section.

In the following a short summary of the individual steps is given which are performed to simulate the system. These points describe the same procedure as is depicted in the flow chart in figure 4.4. The most important points will then be outlined in extra subsection.

1. As a first step, the required data which would be measured in an experiment have to be created. In an experiment time spectra of the intensity in dependency of ω_p and φ_0 are recorded. In the simulation, this is done by calculating equation (4.4) for a 3D grid of Δ , ω_p and φ_0 . Afterwards, the calculated data is numerically Fourier transformed to the time domain.
2. The absolute square of the data in the time domain is Fourier transformed with respect to φ_0 . Everything except for $f = \pm 1$ is set to zero and the back transformation is performed.
3. In an experiment it is, due to technical issues, not possible to record the first few nanoseconds of the signal. Since one of the steps in the algorithm is a Fourier-transformation in time, and the aim is to check if the method would work in an experiment as well, the first 15 ns of the simulated data are cut off. The upper time limit is set to 380 ns. This is larger than the bunch time of a synchrotron, like at PETRA III the bunch time is equal to 192 ns [58]. However, this time has been chosen, to evaluate the theoretical limits of the Oscillation-drive. In chapter 5, the Oscillation-drive is compared with the late time integration method. For this, the late time integration method uses the same time interval. Therefore, the comparison is on an equal level.
4. The cut data is Fourier transformed with respect to t . In ν -space, the peaks ν_{p2}^{\pm} , described in section 4.1.3 are isolated and back transformed. However, this demands a bit more technical effort. Therefore, it is explained with more detail in section 4.2.1.
5. The outcome of the Fourier analysis, can be described with equation (4.20) or equally with (4.39). A cosine with amplitude and phase offset is fitted to the data.

To reconstruct the spectrum and phase out of the fit data, it demands further post processing of the data. This is described in section 4.2.2.

4.2.1. Numerical Implementation of the ν -space Filter

In this section the theoretically discussed procedure to isolate the desired summand ($n = 1$) in equation (4.35), is going to be analyzed with regard to its numerical implementation (compare with section 4.1.3).

To give a short recap, starting point of this procedure is the following. From the previous analysis, there are two equations ((4.35), (4.34)), describing the measured signal. The summand $n = 1$ in equation (4.35) has to be isolated. This means that the corresponding peaks are kept, whilst the rest of the spectrum is set to zero. To achieve this the different frequencies in time of the sidebands are used. Performing a Fourier transformation in time, it is possible to separate the contribution of each sideband in ν -space. The analytical analysis shows that the spectrum in ν -space is made up of δ -peaks at known frequencies which are convoluted with contributions from the target and the analyzer. Due to the being unknown, since it is the quantity to be measured, in the analytical analysis, the assumption has been made that the convolutions do not lead to any overlap of the peaks.

By the right choice of the shift S , it can be ensured that there is no overlap and therefore, the cut off frequencies within the spectra are set correctly. To formulated these conditions is the goal of this section.

For the analysis the first peaks ($\nu_{p1/p2/p3}^{\pm}$) up to order $n = 2$ are considered, which are depicted in figure 4.5. In the following, everything refers to the positive half-plane in ν -space. Since the positions of the peaks are symmetric, it is sufficient to take the negative values of the cut off frequencies for the negative half-plane.

To know where to cut in the spectra, it is necessary to analyze the position of the peaks and to make an assumption about their widths, which arises due to the convolution with the target contribution. The positions of the peaks have been written down already, in section 4.1.3 and are depicted in figure 4.5.

The widths of the peaks can be estimated, by looking at equation (4.35) and (4.34). There, the δ -peaks are convoluted with the Fourier transform of $A(t, \tau)$, or of $A(t, \tau)R_T(t)$. This means that the width of $A(t, \tau)R_T(t)$ and $A(t, \tau)$ have to be estimated. $A(t, \tau)$, is resonantly scattered part of the analyzer without motion in the time domain. Its width in the energy domain (Δ), is γ_A , which is the linewidth of the analyzer.

$R_T(t)$ is the Fourier transform of the target. At the beginning of the chapter, the variable l has been introduced. It describes the range in which the absolute square of the target energy spectrum is different from unity. This is expressed as a formula in (4.3),

too. Therefore, its width is to be assumed to be maximal $2l$, which is a lot of larger than γ_A . Assuming $2l$ for the width is sufficient for both A and R_T .

The principle of the algorithm can be explained by looking again at figure 4.5. There, the positions of the peaks are plotted. Furthermore, the broadening due to the convolution is depicted by the dashed lines. The root of each dashed is l away from the peak. Therefore, the dashed envelope can be seen as the maximal extent of the convoluted peak. For the second peak this point is marked as $\nu_{\text{cO}}^{\text{min}}$ in the figure. The point where the third peak starts to rise again is marked with $\nu_{\text{cO}}^{\text{max}}$. The subscript cO stand for ‘‘cutOff’’. Somewhere between those two point the spectrum should be cut, and everything above this frequency hate to be set to zero.

The easiest way would be to cut the spectrum directly at $\nu_{\text{cO}}^{\text{min}}$. However, the spectrum is non zero between those two points. To illustrate this, in figure 4.6 the spectrum of an example from a simulation is plotted to show this behavior. There, the absolute of the real and the imaginary part are plotted. The dashed lines are the original spectra, the solid lines are the spectra after they have been cut. The peaks $\nu_{\text{p}2}^{\pm}$ and $\nu_{\text{p}1}^{\pm}$ are clearly visible. Furthermore, the maximal and minimal cut off frequencies are marked. One can see, that the imaginary part has a minimum between the minimal and the maximal cut off frequency. This behavior is used by the algorithm: It searches for the minimal value between the two limits. From this point, a linear interpolation from the cutting point to the edge of the spectrum is done. This is because the numerical analysis shows, that the reconstructions become better if the peaks are cut in this way.

In the following, a value for the minimal and maximal cutting point is derived. The lower limit is at the position of peak number two, plus half of the estimated width,

$$\nu_{\text{cutOff}}^{\text{min}} = S - \omega_p + l. \quad (4.43)$$

For the upper cut off limit, the position of peak number 3 and number 1 have to be investigated more closely. Since their dependency on ω_p is weighted by different factors, it have to be checked if peak number 3 is the next neighbor of peak number 2 for all values of ω_p or if this can change. For this, the distance of the other peaks, to the peak number 2 is calculated,

$$\nu_{\text{p}1}^+ - \nu_{\text{p}2}^+ = \omega_p - (S - \omega_p) = 2\omega_p - S, \quad (4.44)$$

$$\nu_{\text{p}3}^- - \nu_{\text{p}2}^+ = -(S - 2\omega_p) - (S - \omega_p) = 3\omega_p - 2S, \quad (4.45)$$

Since S is constant, the minimal distance of the peaks is reached, for the minimal value of ω_p . As it was already mentioned at the start of the chapter, ω_p lies in the range of $\omega_p \in [S - l, S + l]$. Hence, the maximal and minimal values of ω_p are,

$$\omega_p^{\text{max}} = S + l, \quad (4.46)$$

$$\omega_p^{\text{min}} = S - l. \quad (4.47)$$

Inserting ω_p^{\min} to equation (4.44) and (4.45) yields,

$$\nu_{p1}^+ - \nu_{p2}^+ = 2(S - l) - S = S - 2l, \quad (4.48)$$

$$\nu_{p3}^- - \nu_{p2}^+ = 2(S - l) - S = S - 3l. \quad (4.49)$$

Therefore, peak number 3 is the next neighbor. Hence, the upper cut off limit can be set to,

$$\nu_{\text{cutOff}}^{\max} = -(S - 2\omega_p) - l. \quad (4.50)$$

These two limits are implemented and complemented by an minimization algorithm to find the minimum between these two limits. The result of this algorithm is used as the cut off frequency. All datapoints above this limit are extrapolated linearly, decreasing from the cutting point to the edge of the spectrum. This is illustrated in figure 4.6 . This procedure is performed separately for the real and imaginary part. Note that this procedure was described for the positive frequency range only. For the negative range, the cut off frequencies can be mirrored.

From this arises a constraint on the shift S . It has to be large enough such that $\nu_{\text{cutOff}}^{\min} < \nu_{\text{cutOff}}^{\max}$ for all values of ω_p . Since the peak distance is the smallest in the case of $\omega_p = \omega_p^{\min}$, it is inserted in the formulated condition $\nu_{\text{cutOff}}^{\min} < \nu_{\text{cutOff}}^{\max}$,

$$\begin{aligned} 2\omega_p^{\min} - S - l &> S - \omega_p^{\min} + l \\ \Leftrightarrow S &> 5l. \end{aligned} \quad (4.51)$$

This condition is important for the following reason. If the chosen value of S is not large enough, this leads to a failure of the reconstruction algorithm. The reason for this is, that the peaks in the ν -space start to overlap. As a consequence, the contributions of the different sidebands can not be separated. The data remaining after the ν -space filter, cannot be describe by equation (4.16) anymore. Therefore, the try to fit a cosine to the data returns inappropriate fit parameter, which cannot be used to reconstruct the spectrum or the phase.

4.2.2. Spectral Intensity and Phase Reconstruction from the fit algorithm

In the previous section, the numerical implementation of the second filter method in 4.1.3 has been discussed. The output of this algorithm can be described by equation (4.39). The basic principle of how to reconstruct the spectrum and the phase have already described at the end of section 4.1.2. In this section, however, a more detailed analysis is given.

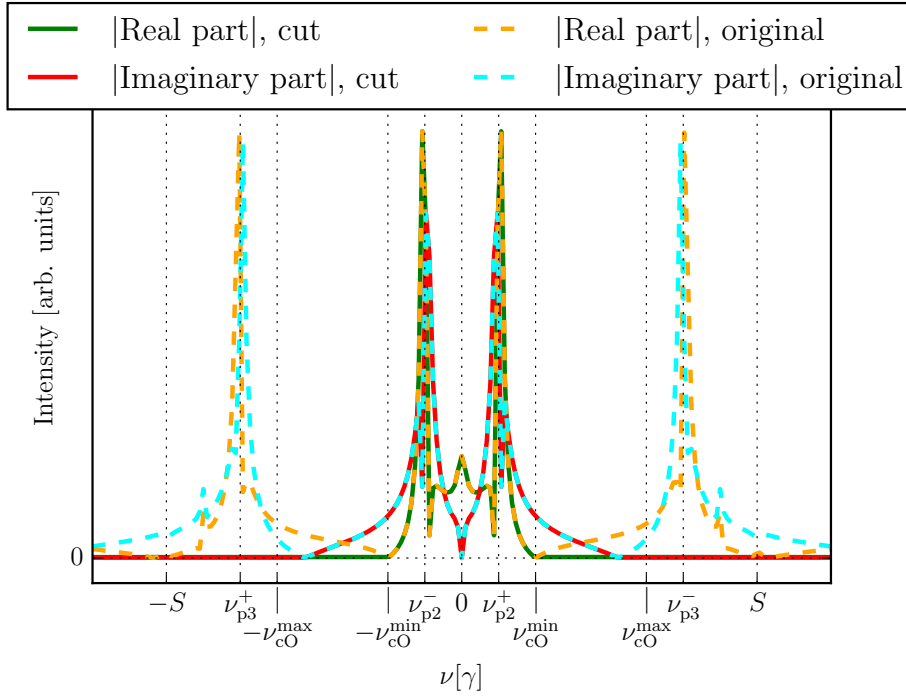


Figure 4.6.: Illustration of the cut off algorithm of spectra in ν domain. In the figure the real and imaginary part of the spectra is plotted. The dashed lines are the spectra before, the solid lines the spectra after they are cut. The peaks, ν_{p1}^{\pm} , ν_{p2}^{\pm} , are clearly visible. Furthermore, the maximal and minimal cut off frequencies are plotted. Between those two frequencies, the minimum of the spectrum is searched. At this point the spectra are cut, and linearly extrapolated until the edge.

For the reconstruction, the function,

$$f(\varphi_0) = D(\omega_p, t) \cdot \cos(\varphi_0 + a(\omega_p, t)) \quad (4.52)$$

is fitted to the data. This is done for each pair of ω_p, t . The fit parameters in dependency of ω_p and t now contain all necessary information.

Degeneracy of fit parameters One point which is really important for the analysis is to note that the fit parameters are degenerate. This means that it is possible to describe the same function with different values of the fit parameters. This is due to the periodicity of the cosine, which implied that $\cos(x \pm \pi) = -\cos(x)$ and $\cos(x + 2\pi) = \cos(x)$.

This means, that a function of the form of equation (4.52), can be written as,

$$f(\varphi_0) = D \cos(\varphi_0 - a) \quad (4.53)$$

$$= -D \cos(\varphi_0 - \underbrace{a'}_{a \pm \pi}) \quad (4.54)$$

$$= D \cos(\varphi_0 + \underbrace{a''}_{2\pi - a}). \quad (4.55)$$

Therefore, the output of the fit algorithm have to be mapped in one of these descriptions. In this thesis, the parameter are chosen as described in (4.53). This means, that the amplitude is chosen to be positive. This can be done easily by taking the absolute value. Further a' and a'' have to be converted to a by adding or subtracting π or 2π , respectively.

Reconstruction of the Spectrum

First the spectrum $|\hat{R}_T(\Delta)|$ is reconstructed using the absolute value of the amplitude D . Due to (4.16), the amplitude is equal to,

$$|D(t, \omega_p)| = 2J_2(p_0)J_1(p_0)A(t, \tau)|R_T(t)| \cdot |\hat{R}_T(S - \omega_p)|. \quad (4.56)$$

This equations has to be evaluated for every value of ω_p and t . To reconstruct the spectrum $|\hat{R}_T(\Delta)|$, t is fixed to a value t_0 , and $S - \omega_p$ takes the place of the detuning Δ . At the first glance, the reconstruction is finished now, since,

$$|D(t, \omega_p)| \propto |\hat{R}_T(S - \omega_p)|. \quad (4.57)$$

Almost all factors in (4.56), are constant for a fixed t_0 . The exception is $A(t_0, \tau)$, where τ depends of ω_p . However, this dependency is small, therefore it can be neglected. By dividing the data for a fixed t_0 through its maximum. Therefore the largest value in ω_p direction, for each fixed value of t is equal to one. This means that each reconstruction for a fixed value of t is weighted equally now.

At a first glance, the reconstruction is done now. However, the numerical analysis reveals that the reconstruction of one single time t is overlaid with a lot of oscillation. They can be smoothed by averaging the reconstructions over several values of t , described by the time interval $[t_1, t_2]$. The quality of reconstruction depends strongly on the chosen time interval, which is an important point to consider if one wants to perform a systematic reconstruction analysis. In chapter 5 a systematic analysis will be done. Therefore this point will be discussed there.

As a last step, the averaged spectrum is normed again. For this, it is used, that the range $[-l, l]$ in which the spectrum is reconstructed, is chosen in a way, that the spectrum

converges to unity at the edge. Hence, the average over the outermost few datapoints at the left and right edge of the reconstruction is taken. Next, the reconstruction is divided by this average, which normalized the reconstruction to a baseline. The reason why this is done is because there are spectra, which have a peak, which is larger than the baseline (see figure 2.4). To ensure, that the peak is reconstructed correctly, the averaged spectrum is normalized like described above. This ensures, that the baseline is at one and the peak is larger than the baseline.

Reconstruction of the Phase

The reconstruction of the phase it requires a bit more effort than the spectrum. Due to (4.16), the offset a of the fit is equal to,

$$a(t, \omega_p) = \hat{\theta}(S - \omega_p) - \theta(t) - (S - \omega_p)t \quad (4.58)$$

The reconstruction can be divided to 4 single steps. The most important steps are depicted in figure 4.7. There, data of a simulation of a single line resonance foil are used.

First step The first step is to account for the degeneracy of the fit parameters. As mentioned at the beginning of the chapter, it arises due to the periodicity of the cosine function. The output of the fit algorithm is plotted as the blue curve in figure 4.7. To map them to the range between -2π and 0 , for each value of t and ω_p , the following operations are performed,

1. if $D < 0$ and $a(\omega_p, t) > 0$, $a(\omega_p, t) = a'(\omega_p, t) - \pi$,
2. if $D < 0$ and $a(\omega_p, t) < 0$: $a(\omega_p, t) = a'(\omega_p, t) - \pi$,
3. if $D > 0$ and $a(\omega_p, t) > 0$: $a(\omega_p, t) = a''(\omega_p, t) - 2\pi$.

The outcome of this is the orange curve in figure 4.7.

It is important, that this is done as a first step. If the operations of step two and three would be done without this remapping, the red curve would have several jumps within the range of $[0, 2\pi]$.

Second step As a second step, the linear slope of the orange curve is erased, by subtracting $(S - \omega_p)t$ which yields the green curve in the figure.

Third step The third step is to use the modulo operator, to map the green curve to $[0, 2\pi]$, which is represented by the red curve.

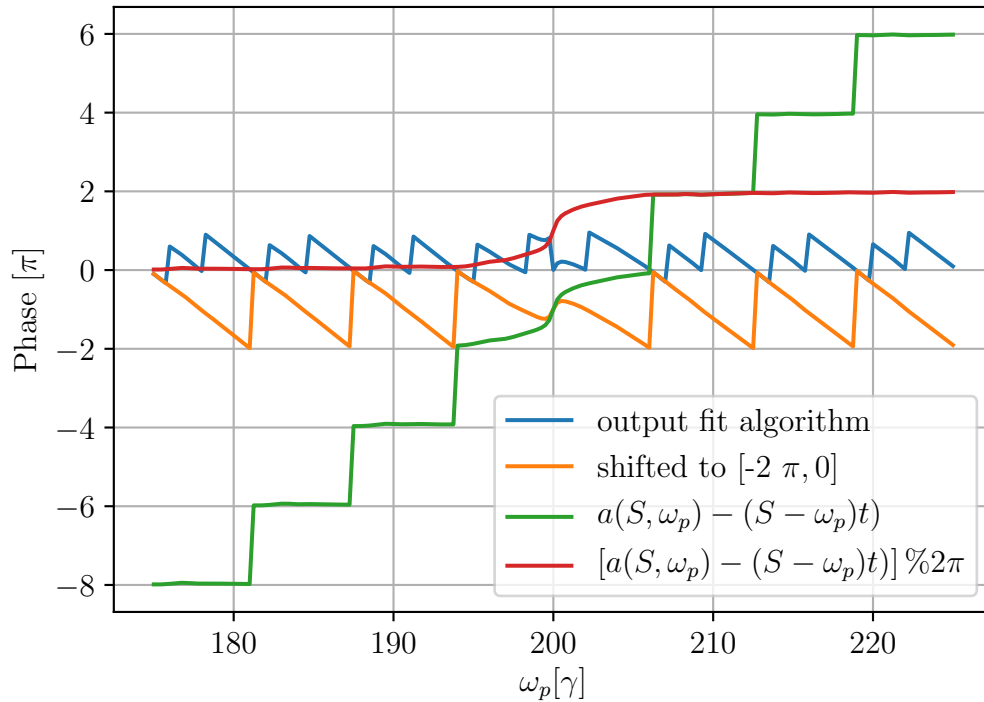


Figure 4.7.: Different steps for the reconstruction of the phase of the Single line target at time $t = 140$ ns. The blue curve shows the direct output of the fit algorithm. The orange line, shows the data mapped to the interval $[-2\pi, 0]$, taking into account the sign of the fitted amplitude. To obtain the green curve, the linear slope of $(S - \omega_p)t$ have been subtracted. The red curves shows the same data, but mapped to $[0, 2\pi]$ using the modulo operator. The mapping of the blue data to the orange data is important. If this is not done, the red curve would have several jumps in the interval of $[0, 2\pi]$.

Fourth step This is already close to the spectral phase which is intended to reconstruct. However, the phase is in the range of $[-\pi, \pi]$. Furthermore, it is assumed, that the phase becomes 0 at the edge of the data. Therefore, as a fourth step, the each datapoint of a reconstructed spectrum is remapped to $[-\pi, \pi]$, using the condition that the datapoints on the left and right edge converge to zero, and that the distance of each point to zero is minimized.

The final reconstructed phase, can be seen in the plots in section 4.3, for representative examples.

4.3. Example Calculations

So far a theoretical model to reconstruct the spectral phase of an unknown target has been developed. Furthermore the numerical implementation the reconstruction algorithm was outlined. In this section two specific example targets are investigated and the results of the spectral and phase reconstruction in each case are shown.

The first chosen example is a single resonance line absorber, whose response function $\hat{R}_T(\Delta)$ is described by,

$$\hat{R}_T^{\text{SL}}(\Delta) = e^{\frac{-ib_T}{\Delta - i\frac{\gamma_T}{2}}}, \quad (4.59)$$

with $b_T = 2$ and $\gamma_T = 1$. The SL in the superscript stands for ‘‘Single Line’’. Such a single resonance line target is one of the simplest non-trivial targets that can be considered and thus serves as an archetype system to demonstrate the reconstruction algorithm.’’

The second target used here, is a double line absorber, whose response function is,

$$\hat{R}_T^{\text{DL}}(\Delta) = e^{\frac{-ib_T}{\Delta + \delta\omega - i\frac{\gamma_T}{2}}} \cdot e^{\frac{-ib_T}{\Delta - \delta\omega - i\frac{\gamma_T}{2}}}, \quad (4.60)$$

where again $b_T = 2$ and $\gamma_T = 1$ and $\delta\omega = 5$. The DL in the superscript stands for ‘‘Double Line’’. Such a double line resonance target occurs in the case of Zeemann-splitting of the nuclei transition in a Mossbauer nuclei. This can be measured in case of α -Iron, where the electron generate a magnetic field at the position of the nucleus, which naturally leads to Zeemann-splitting.

The numerical values for the other used parameters are: $b_a = 0.5$, $\gamma_a = 0.1$, $p = 2.4$, $S = 200$, $l = 25$.

To determine the averaging time interval $[t_1, t_2]$ for the energy spectrum reconstructions, a metric which quantifies the quality of the reconstruction have been used. The lower the rating of the metric, the better the reconstruction. t_1 and t_2 are then chosen by an algorithm that minimizes the outcome of the metric. The principle of the metric is that it takes the absolute square of the difference of the reconstruction and the original spectrum. This procedure is described in more detail in chapter 5.

For the reconstruction of the phase, it is not necessary to perform a time average. The reconstruction works well already for a single point in time. However, an average over several times improves the reconstruction also in this case. This is mainly due to oscillations, which appear if a single point in time is taken (compare with the green curve in 4.8b and 4.9b). Especially at the edge, the oscillations lead to the case that the reconstructions are larger or smaller than the original spectrum. Therefore the whole spectrum can be smoothed by an average also in this case. The time interval over which the average is calculated is fixed to [130 ns, 180 ns]. There is no special reason for this

interval. However, it is mainly important that it is large enough to smooth out the oscillations. This means that the time interval for taking an average of the phase is robust.

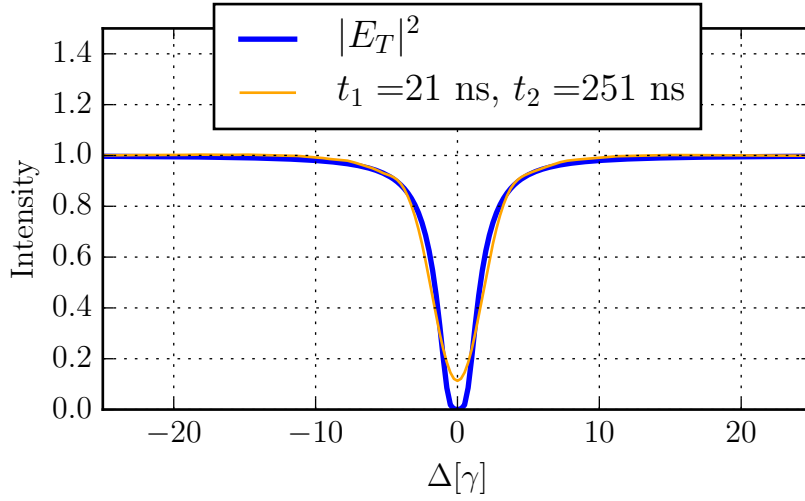
Single line target The reconstructions of the single line target are plotted in figure 4.8. The reconstruction of the energy spectrum is given in 4.8a, the one of spectral phase is shown figure 4.8b. The agreement of the reconstruction, both for the spectrum as well as for the spectral phase is are found to be very good. For the spectrum, one can see that at the minimal value of the dip, the reconstruction is not able to reproduce zero intensity. This is due to the underlying principle of the Oscillation-drive. The physical interpretation of the scanning head approximation is that the sideband of the analyzer is used to scan the target. This means that, in the ideal case of a δ -shaped analyzer, the overlap of the analyzer and the target in the energy domain, gives the value of the target at exactly the position of the analyzer. Therefore, in the case where ω_p is chosen such, that the resonance frequency of the sideband and of the target exactly match, the theory would predict a measured intensity of zero. However, due to the not finite but small linewidth of the analyzer, there will still be a signal in the time domain.

Double line target: The reconstruction of the double line target spectrum and spectral phase are plotted in figure 4.9. The reconstruction of the energy spectrum is given in 4.9a, the corresponding complex phase in figure 4.9b. Here it is found again, that the reconstruction is very good in both cases. However, the same effect as in the single line case is observed, which is that it is not possible to reconstruct the zero intensity of the minima of the target.

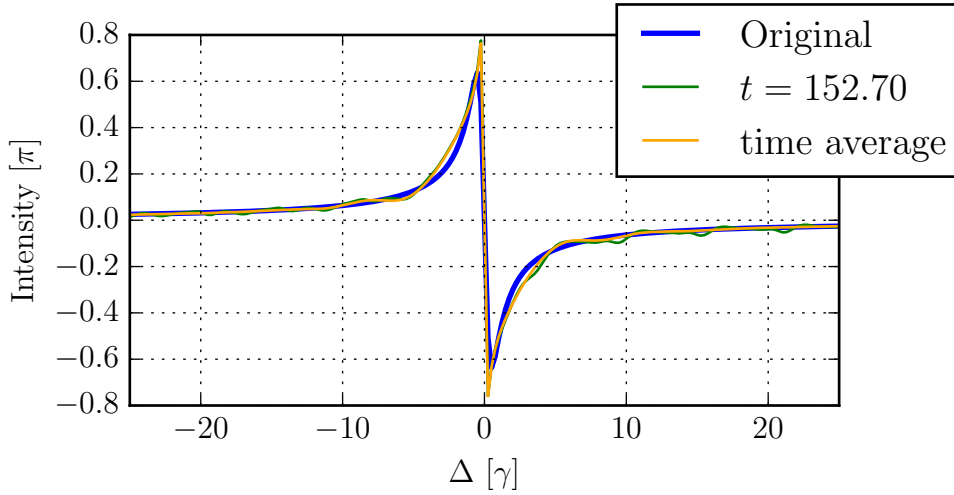
Short Summary On the basis of these two representative examples, a short summary of the Oscillation-drive is given. At the beginning of the chapter, a theory of the Oscillation drive is developed and the promising applications of this concept have been explained. In order to confirm its practical and numerical feasibility, a numerical simulation has been discussed. Finally, in this section, the Oscillation-drive have been simulated for two different representative examples. The agreement with the original phase and spectrum are really good in both cases.

Therefore, in this chapter a new method to reconstruct the energy spectrum of an unknown target has been developed. In addition to the energy spectrum, the complex phase of the energy spectrum can be reconstructed, too. The complete theoretical theory which was developed, in addition with the numerical simulation makes the Oscillation-drive an future alternative to the established methods.

However, for the spectrum there is a deviation at the dip, which originates from the small but finite linewidth of the analyzer.

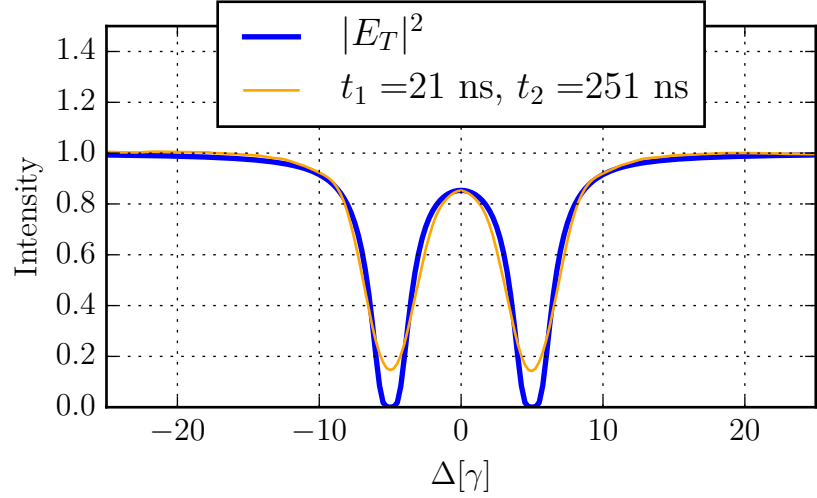


(a) Reconstruction of the energy spectrum. In blue the absolute square of the original target spectrum is plotted. In orange the reconstruction, using the Oscillation-drive and the average time interval from $t_1 = 21$ ns to $t_2 = 252$ ns.

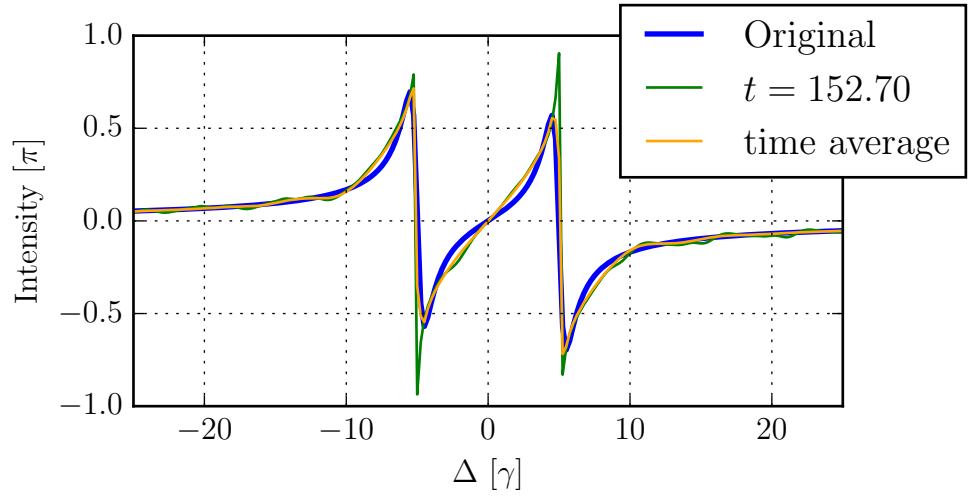


(b) Reconstruction of the complex spectral phase. In blue the complex phase of the original target spectrum, in red and green the reconstructions are plotted. For the red curve, the average over the interval $t_1 = 130$ ns to $t_2 = 180$ ns have been taken, for the green curve the data at time $t = 153$ ns.

Figure 4.8.: In this figure, the original energy spectrum and phase of a single line target are plotted as well as its reconstructions using the Oscillation-drive. In (a) the original and reconstruction of the energy spectrum, and in (b) the original and reconstructed complex spectral phase.



(a) Reconstruction of the energy spectrum. In blue the absolute square of the original target spectrum is plotted. In orange the reconstruction, using the Oscillation drive with the average time interval from $t_1 = 29$ ns to $t_2 = 254$ ns.



(b) Reconstruction of the complex spectral phase. In blue the complex phase of the original target spectrum, in red and green the reconstructions are plotted. For the red curve, the average over the interval $t_1 = 130$ ns to $t_2 = 180$ ns have been taken, for the green curve the data at time $t = 153$ ns.

Figure 4.9.: In this figure, the original energy spectrum and phase of a double line target are plotted as well as its reconstructions using the Oscillation-drive. In (a) the original and reconstruction of the energy spectrum, and in (b) the original and reconstructed complex spectral phase.

This deviation, of course reduces the quality of the reconstruction. To quantify this, it is desired to have a measure of the quality. This task is subject of the the next chapter.

5. Evaluation Of the Oscillation Drive

In chapter 4, a new method to reconstruct the absolute of the energy spectrum as well as the phase have been introduced. The agreement between our reconstructed and the original spectra is found to be good for two representative example systems. Indeed in both cases, the spectrum and the phase is reconstructed successfully.

However, to appraise the quality and the advantages of the Oscillation-drive a systematic evaluation is necessary. In particular, the dependence of the Oscillation-drive's performance, of the parameters p , γ_A and S is of special interest in order to evaluate the robustness of the reconstruction.

Furthermore, there are already existing methods to determine the energy spectrum of a target. Therefore it is important to compare the reconstruction of the energy spectrum by the Oscillation-drive with the existing methods to see if there are any advantages. And if there are any, to find out what they are. Note, that the comparison, is only made for the spectrum. This is because, the existing methods are not able to reconstruct the phase. Therefore, this advantage can't be quantified by comparison. An important method to measure the target spectrum is the late-time integration, using an analyzer foil on a Doppler-drive. This has been successfully used in [21, 56]. Therefore the Oscillation-drive's performance for the spectral intensity reconstruction is compared with this method.

To evaluate theses questions in a systematic way, it is important to evaluate the reconstructions to have a quantitative measure of the quality. For this the reconstructions are compared with the original spectrum and a number is assigned to them, using different metrics, representing the quality of the reconstruction.

As already said in chapter 4, the quality of reconstruction depends on the chosen time interval $[t_1, t_2]$, which is used to average over the data. Furthermore, one result was, that the choice of the interval influences which part of the spectrum is reconstructed. That means that for one choice of the time interval, the edge of the spectrum is reconstructed very well, whereas, for an other choice, the extrema of the target are reconstructed better.

This can be seen in figure 5.2, where the spectra for different time intervals are plotted. In 5.2a the reconstruction of the single line target is plotted. The average time interval is chosen such, that the spectrum agrees as good as possible with the dip of the spectrum. In 5.2c, in red is plotted the reconstruction using the same parameter as the red curve

in the previous case, but with a different average time interval. The times in this case are chosen such, that the accordance with the edge is the highest.

Therefore we are faced with the challenge to find a way how to choose the time interval and find metrics which take into account the different regions of the spectrum.

5.1. Metrics and Averaging Time Intervals

The need to find metrics to evaluate the reconstruction performance, and approaches to determine the average time interval is addressed in this chapter. First three different metrics are introduced. All metrics are based on the comparison of the reconstructed spectrum with the original one. Secondly three approaches to find the average time interval are presented.

5.1.1. Different Metrics for Performance Evaluation

Each of the three different metrics focus on different regions of the spectrum. For all of them it is necessary to calculate discrete values of the original spectrum. This is due to the values for ω_p discrete, too, spanning a grid. And since ω_p is used to scan the target, the reconstructed spectrum will be given at these supporting points as well. Therefore, the original target has to be evaluated at the points $S - \omega_p^i$, where ω_p^i describes the i -th point on the grid.

The discrete points of the original spectrum will be denoted by $(\hat{R}_T^O)_i$. The reconstructed points of the spectrum will be denoted by $(\hat{R}_T^R)_i$. Note, that they both represent complex quantities.

Absolute square metric This metric represents the simplest way to evaluate the reconstruction performance. Basically, the absolute square of the difference of all points of the reconstruction and the original spectrum is summed up over all grid points. Written as a formula, this gives,

$$M_{\text{AbsSq}} = \sum_i \left| \left| (\hat{R}_T^O)_i \right|^2 - \left| (\hat{R}_T^R)_i \right|^2 \right|^2. \quad (5.1)$$

Weighted absolute square with focus on the edge This metric is based on taking the absolute square as well, but with the difference that each summand is weighted with the absolute square of the target. As a consequence, at the edge, where the absolute square of the target is approximately one, the summand contributes strongly, whereas close to the dip of the target, where the absolute square decreases to almost zero, the summand contributes weakly. As a formula this reads,

$$M_{\text{W-AbsSq,edge}} = \sum_i \left| \left| \left(\hat{R}_T^{\text{O}} \right)_i \right|^2 - \left| \left(\hat{R}_T^{\text{R}} \right)_i \right|^2 \right|^2 \cdot \left| \left(\hat{R}_T^{\text{O}} \right)_i \right|^2. \quad (5.2)$$

It is important to note, that there are cases where, the metric returns a value which seems to be good, the reconstruction however, does only match on the edge but does not reproduce the extrema of the target. To ensure that this is not the case for a good rating, it can be compared, with the unrated metric. If this returns a high value, this is an indicator for the case just described.

Weighted absolute square with focus on the dips To calculate a metric which focus on the dip of a spectrum, one can use the same idea as for the previous case. But instead of multiplying each summand by $\left| \left(\hat{R}_T^{\text{O}} \right)_i \right|^2$, it is multiplied by $\left(1 - \left| \left(\hat{R}_T^{\text{O}} \right)_i \right|^2 \right)$, which has the effect that the summands on the edge of the spectrum contribute weakly, while the dips contribute strongly. As a formula this reads,

$$M_{\text{W-AbsSq,dip}} = \sum_i \left| \left| \left(\hat{R}_T^{\text{O}} \right)_i \right|^2 - \left| \left(\hat{R}_T^{\text{R}} \right)_i \right|^2 \right|^2 \cdot \left(1 - \left| \left(\hat{R}_T^{\text{O}} \right)_i \right|^2 \right). \quad (5.3)$$

For this metric it is important to note, that it focuses heavily on the dips in the spectrum. Therefore, there are cases, where the dip the reconstruction performs well in the dip region, while the remaining spectrum does not necessarily match with the original. Nevertheless there are some cases where it is good to have a measure of the dip only, for example, if one wants to fit a model function to the data, or, as later in this chapter, to gain a better possibility to compare the different methods. Hence, the ratings of this metric have to be interpreted carefully. They can be a good indicator, but there are cases as well, where this metric returns a good value, whereas the other metrics do not and the reconstruction is clearly bad if evaluated by eye. To ensure that this is not the case for a good rating, the same can be done as for the other weighted metric, and double check the unweighted metric. If this returns a high value, this is an indicator for the case just described.

5.1.2. Determination of the Average Time Interval

As already mentioned, the time interval over which the spectrum is averaged, has an influence on the quality of the reconstruction. Therefore, this time interval is important, to ensure that the result of the metrics is trustworthy. From this the question arises, how this interval can be determined. For this, there are used three different methods in this chapter, which will be introduced in the following. The first one uses the metrics which have just been introduced.

The second one, is not actually not really an method which actively determines the times, but proposes, that the same time interval is used for all parameters.

The third, uses known a convergence and symmetry of the target spectrum as criteria.

Minimize the reconstruction metric This procedure assumes, the target response function $\hat{R}_T(\Delta)$ to be known. This is of course not possible in a real experiment, where $\hat{R}_T(\Delta)$ is desired to be measured. To show the theoretical limits and chances of the Oscillation-Drive, however, this method works well.

The principle is the following. For each parameter set, the metric is taken as a two dimensional function, with the arguments t_1 and t_2 . This function is minimized using a minimization algorithm. The advantage of this method is, that for each parameter set one can find the optimal time interval which minimizes the metric. However, the disadvantage is, that in an experiment this method is not possible, because the spectral target response function $\hat{R}_T(\Delta)$ is not known. Nevertheless this is a useful tool for theoretical calculations. A possible use case can be the same as in this thesis, to use it for simulations. In combination with the different metrics, which focus on different region of the spectrum it is possible to optimize the time interval in a way to match those different regions the best.

Fixed time interval This is not really a method to determine the interval but rather the idea to use a fixed times, independently of the parameters of the simulation. What remains is the problem to find the initial time interval. The simplest method would be to simulate the spectrum and use the minimization method above for one parameter set. This method is very useful in case of a systematic parameter evaluation, to test the robustness of the reconstruction with respect to the time interval. This has been done for the parameter evaluations in this chapter.

Ab initio algorithm: symmetry and edge criteria This algorithm determines the time interval using a symmetry argument as well as the assumption that the spectrum converges to unity at the edge.

The symmetry argument assumes the energy spectrum of the target to be symmetric with respect to the center of the reconstruction range. For this the algorithm calculates

the difference of the values of the reconstruction on the support points which are vice versa, with respect to the center. Then it sums up the absolute of each calculated difference. Therefore the lower the result, the better is the symmetry.

The edge criteria assumes that the absolute square of the target energy spectrum converges to unity at the edge of the reconstruction range. Hence the algorithm takes the data points at the edge and sums up the absolute value of the difference of the data points to one. The number of data points which are used for this criteria have to be set manually. Here again, the lower the result, the better fulfilled is the criteria.

Both results are weighted with a factor and added. For the two weighting factors there is the restriction, that their sum is one. Therefore it is possible, if the response function of the target is not symmetric, to use only the edge criteria.

The advantage of this algorithm is clear: Except for the symmetry assumption, there is no need for further information of the target than the data coming from an experiment. If it is not possible to make an assumption on the symmetry of the target, the weighting factor can be used to set the symmetry criteria to zero. This makes this algorithm independent of additional information over the target. Unfortunately, this approach does not work as well as the minimization algorithm does. Nevertheless, due to its independence of informations to the target, this can be a useful tool, for future experiments.

5.2. Evaluation for Exemplary Targets

The presented metrics and methods are now applied to the two targets which have been introduced in chapter 4.3. To provide better readability of this section, not all plots of every method and target is given in the main part. The chosen contain all information, which are necessary give the conclusions of the evaluation. The chosen plots show the analysis of the single line target. The remaining plots show the same evaluation for the double line target. They are given in appendix A. They support the results of this chapter, because they show the same behaviour than the plots within the main part.

In each plot one of the methods introduced above to determine the time interval is used for one target. They consist of three subplots, which quantify the quality of the reconstruction using each of the three metrics.

5.2.1. Parameter Analysis

There are some significant features which can be found for each metric and time interval determination method in dependency of the used parameters, which are described in the following.

Clear parameter areas In figure 5.3, 5.4 and 5.5, there are clear areas and tendencies where the rating is good and where it becomes worse. A good rating is equal to a low value of the metric. The higher the ratings, the worse the reconstruction. In those figures, a low value is equal to the pink color in the figures. All ratings which are red color coded are so bad, that it is hard to recognize similarities to the original spectrum at all. In all plots, which show a dependency of γ_A , the best ratings can be found for small values of γ_A . Furthermore there are quite clear dependencies on p , which are listed in the following.

1. For values of $p \approx 2.4$, all plots show that the reconstruction is good.
2. For small p , the reconstruction becomes better as well.
3. At $p \approx 5.1$ and $p \approx 5.5$ and especially for small γ_A , pink areas can be found as well.
4. At $p \approx 1.8$ and $p \approx 5.3$ the reconstruction is bad for all values of γ_A .

Firstly the dependency on the piezo amplitude p is considered. To understand this, it is necessary to look at the theory again. The whole method of the Oscillation-drive is based on equation (4.39). For its derivation, the oscillation amplitude of the piezo has been set to $p_0 = 2.4$. This was necessary to set (4.38) $J_0(p_0) \approx 0$ in equation . As a consequence, it was possible to write the real part as a single cosine function which lead to (4.39). If p is now detuned from p_0 , the last step can not be performed in this way. Instead, equation (4.15) becomes,

$$|\tilde{E}_D(t)|^2 = 2A(t, \tau) |R_T(t)| \cdot |\hat{R}_T(S - \omega_p)| \cdot \left[J_0(p) \cos \left(\varphi_0 - (\hat{\theta}(S - \omega_p) + \theta(t) + (S - \omega_p)t) \right) + J_2(p) \cos \left(\varphi_0 + (\hat{\theta}(S - \omega_p) - \theta(t) - (S - \omega_p)t) \right) \right]. \quad (5.4)$$

Hence, the cosine term, which is used for the reconstruction is perturbed by an other cosine term. Consequently, the Oscillation-drive works well, as long as one of the Bessel-functions is zero or at least small. In figure 2.6, the Bessel-functions of the first kind are plotted for the different orders n . In the following, “Bessel-function of order n ” and “ n -th order Bessel function” are used to signify the n -th order of the Bessel function of the first kind. Therefore the following cases have to be considered:

1. As already said, for $p \approx 2.4$, $J_0(p)$ becomes zero. Furthermore, the first order Bessel-function is larger than for small p . Since the first sideband, which is weighted with the first order Bessel-function, is used to sample the target similarly to a sensing-head, one would expect the best reconstruction for this value.

2. For small p , $J_0(p)$ approaches unity, whereas, $J_2(p)$ approaches zero. Hence, high quality reconstructions are expected in this range.
3. For $p \approx 5.1$ and for $p \approx 5.5$, $J_0(p)$ and $J_2(p)$, respectively, become zero each. Furthermore, $J_1(p)$ is quite large at this values of p , therefore for these two values, one would expect also good reconstructions.
4. For the values of $p \approx 1.8$ and $p \approx 5.3$ it is, $J_2(p) \approx J_1(p)$. For these values, the reconstructions are expected to be bad, because both cosine are disturbing each other maximally.

Comparing with the plots with these predictions, they can be verified.

Now the dependency on γ_A is considered. One finds that for small γ_A , the reconstructions becomes better. This can be understood by looking at the sensing head approximation (4.6) of this method. There it is assumed that the energy spectrum of the target stays constant in the range of the width of the sideband of order $n = 1$. For increasing γ_A , this approximation becomes worse. However, for an experiment there have to be noted, that an analyzer with a small linewidth lowers the count rate. Therefore, this is a optimization between count rate an accuracy.

For the analysis of the double line target in the appendix (A.1 and A.2), one finds the same structure of good reconstructions. However, for increasing γ_A , the ratings getting worse faster than for the single line target.

Special case: first sideband is zero Quite eye-catching is the red line with high ratings of the metrics at a value of $p \approx 3.8$. The reason for this is that for this value of p the first order Bessel-function is approximately zero. Since the first order sideband, which scans the target, scales with $J_1(p)$, it becomes clear, that without this the reconstruction is not good and hence the metrics return a large value.

The reason, why for the weighted metrics and the activated optimization algorithm, the rating is not as bad, is that they only focus on one part of the spectrum. For the right choice of the integration range, the dips are not really distinct. But the edge, which is basically a constant matches very well. Yet it is clear, that an almost constant line is not a good reconstruction. The results in this case for are plotted for the single line target in figure 5.2c.

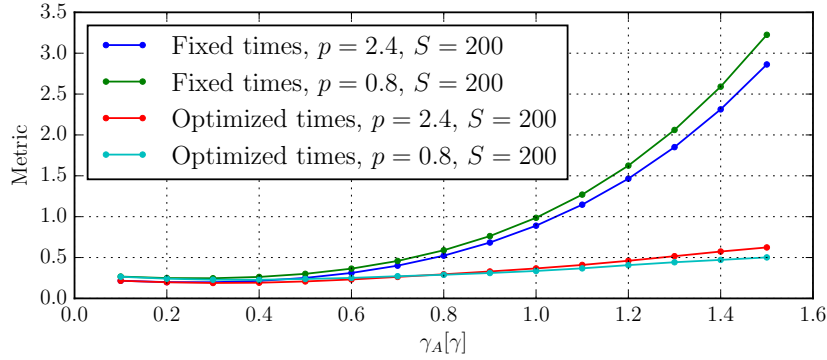
With an other choice of the average time interval, it is possible to generate large oscillations over the whole reconstruction range, which match the resonance dip very well. This can be seen in figure 5.2d. Here the same argument as before can be employed to conclude that this is a really bad reconstruction even if the weighted metric with focus on the dip does not say so. Therefore this is exactly the case described at the presentation of the metrics.

Almost no dependency on S In figure 5.3, the ratings dependent of S and p are plotted. As one can see, there is very less variation of the ratings, whilst varying S . Actually this is what one would expect: The effect of S in time domain is, that it shifts the resonance frequencies of the target and the analyzer relatively to each other. Two dips, separated by S in the energy domain, cause oscillations in the time domain with frequency S .

In ν space the oscillations result in the peaks described in section 4.1.3 and section 4.2. It has been found that the position of the peaks in ν -space is, $\nu = \pm(S - n\omega_p)$, where n stands for the n -th sideband. From this it can be seen, that S has an influence on ν -space and influences the position of the peaks.

As a short reminder, the peaks in ν -space originate from the contributions of the individual sidebands. For the evaluation of the signal, it is necessary to isolate the $n = 1$ sideband. This suggests that S should have an influence on the quality of the reconstruction, because the position of the peaks depend on it. Therefore, this could make the separation of the peaks difficult. This, in principal, is correct. However, for the value of S it the condition was formulated that it has to be larger than $5l$, where l is the relevant extension of the target, compared with equation 4.51. Since the chosen values are above this threshold, the influence of S is this small.

Dependency on average time interval The dependency on the average time interval can be seen by comparing the rating of the metric for the case of a continuous adjustment of the time interval using the metric minimization algorithm and the rating for the case of fixed times. For the analysis, one value for p is taken, even though, every other value could be chosen as well. Here $p = 2.4$ and $p = 0.8$ will be taken. To illustrate this point, in figure 5.1, the profile for the two values of p are plotted in figure 5.4 and 5.5. In blue and green, the values of the metric using a fixed time interval are plotted, in red and mint green the ratings, where the average time interval is optimized to return the best value of the metric. One can see, that for small values of γ_A , the rating for both the fixed times and the optimized times are approximately the same. For values of $\gamma_A > 0.6$ the rating using the fixed time interval increases quickly, whereas the rating with the optimized times increases slowly. This shows the influence of the average interval. To illustrate this point, the reconstruction for $p = 2.4$ and $\gamma_A = 0.1$ and $\gamma_A = 1.5$ are plotted in figure 5.1b for the case of optimized times and in figure 5.1c for the case of a fixed average time interval. For increasing γ_A , the times have to be adjusted. If this is done, the rating of the metric and therefore the deviation of the reconstruction from the original target can be kept low. However, even if, the times are fixed, there is a small range of γ_A where the times still match. However, if the parameter is changed from the original level, the reconstruction worsens if the times are kept fixed. In the figure, only the non-weighted metric is plotted. However, one can see the same behavior using the other metrics as well. This can be seen in the two contour plots (5.4 and 5.5).



(a) Ratings of the unweighted metric.

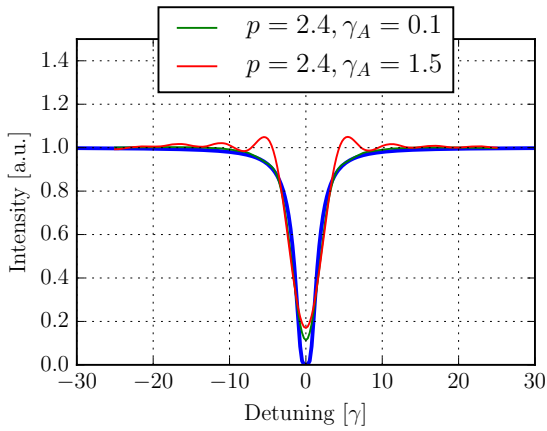
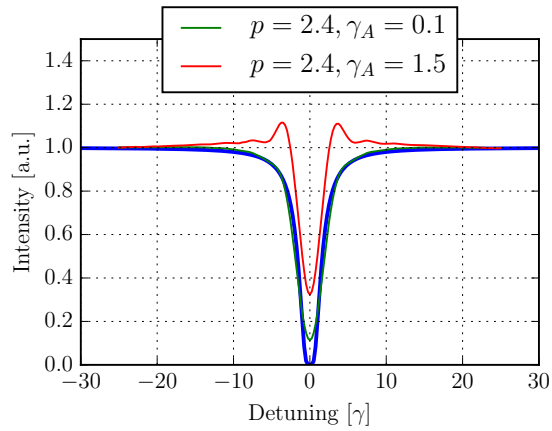

 (b) Green: $t_1 = 20.56$ ns, $t_2 = 251.74$ ns
 Red: $t_1 = 15.80$ ns, $t_2 = 159.07$ ns

 (c) Green: $t_1 = 20.56$ ns, $t_2 = 251.74$ ns
 Red: $t_1 = 20.56$ ns, $t_2 = 251.74$ ns

 Figure 5.1.: (a): Rating of the non weighted metric of a fixed average time interval (green and blue) and the case where the time interval is optimized to the metric for every value of γ_A (red and mint green).

(b) and (c): Reconstruction of the spectrum for using the parameter given in the legend.

One can see clearly that for small γ_A , the ratings are approximately the same. For larger γ_A , quality of the reconstruction becomes worse for the fixed average times, whereas for optimized times, the metric stays at a low level. This shows very clear how important the choice of the average time interval is.

5.2.2. Special Case: Average Time Interval via Symmetry and Edge Criteria

In this section, the case the results of the metric are discussed, where the average time interval was determined by the ab initio algorithm. This is plotted in figure 5.6. Because the quality of the average time finding algorithm is quite different for the single and the double line target, in this figure, both cases are plotted. The result for the single line in (a) and for the double line in (b).

At a first glance, one can see that the areas and features, discussed in the section before (5.2.1) for the other two average time methods are not as clear as before. However, especially for the Double line target, for the first two metrics, there are areas where the ratings are in the lower to midfield. These areas can be found at $p \approx 1.2, 2.4, 5.13, 5.5$, which are the same values for p where good reconstructions are predicted by the theory and which were confirmed by the other methods (see figure 5.4 and 5.5).

This means, that the ab initio algorithm to determine the average times works in principal. At the moment, however, it only produces good reconstructions in the area where the parameters are already chosen in the ideal way, such, that there are no further perturbations by other terms. (compare also with equation (5.4)). The reason why the first two metrics work better for the single line case is probably that the double line target has a larger structure, which can be used by the symmetry algorithm.

The reason, why for the single line target the rating is better for the metric with focus on the dip is that a single dip can be reconstructed more easy if the reconstruction des large oscillations, as it is shown in figure 5.2d. Furthermore, in case of the double line target the local maximum between the dips is often overrated by the reconstructions, if the times are not chosen correctly. This makes it more difficult for the algorithm to achieve a good rating for the double line in combination with the metric focusing on the dips.

Even though, the results in this plot are not as good as for the other time average algorithms, this algorithm is important and valuable because it does not need any further information or assumptions of the target, except of the convergence of the edge, which is needed anyway for the oscillation drive and is usually the case in practice. Optionally the symmetry of the spectrum can be employed. Therefore this algorithm can be used on experimental data, which makes it practically useful. This is why it is presented in this thesis.

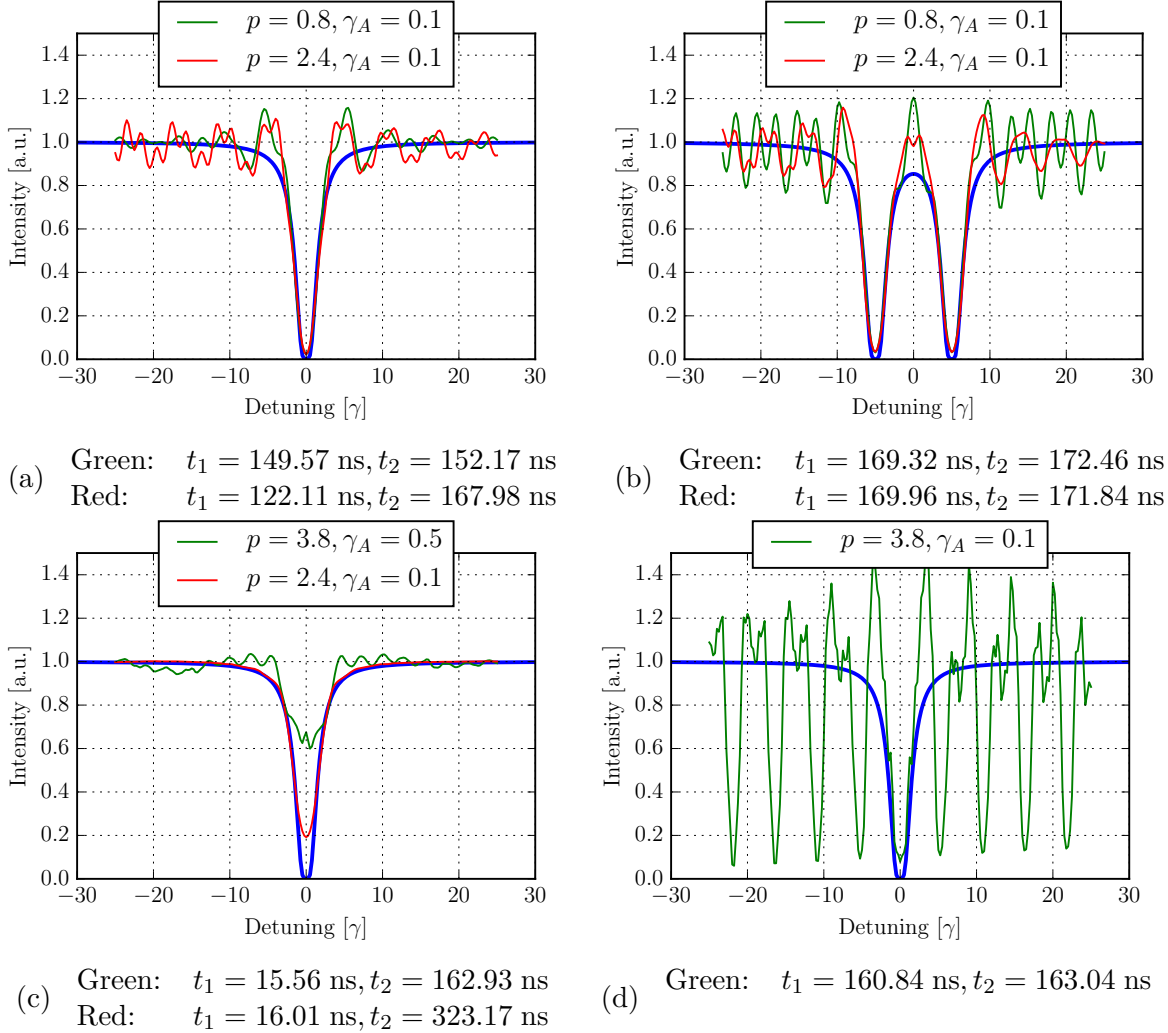


Figure 5.2.: Reconstructions of the energy spectra for different targets, choices of parameters and different average time intervals. The blue line is the absolute square of the original target. The parameters are given in the legend of the plots. For all plot the value of S is chosen to be $S = 200$. (a) and (b): times optimized for metric with focus on dip. (c): times optimized for metric with edge focus. (d): times optimized to for metric with dip focus. For $p = 3.8$ (in (c) and (d)) the first sideband, which should scan the target is approximately zero. The rating of the red curve in (c) is 0.026 which is really good.

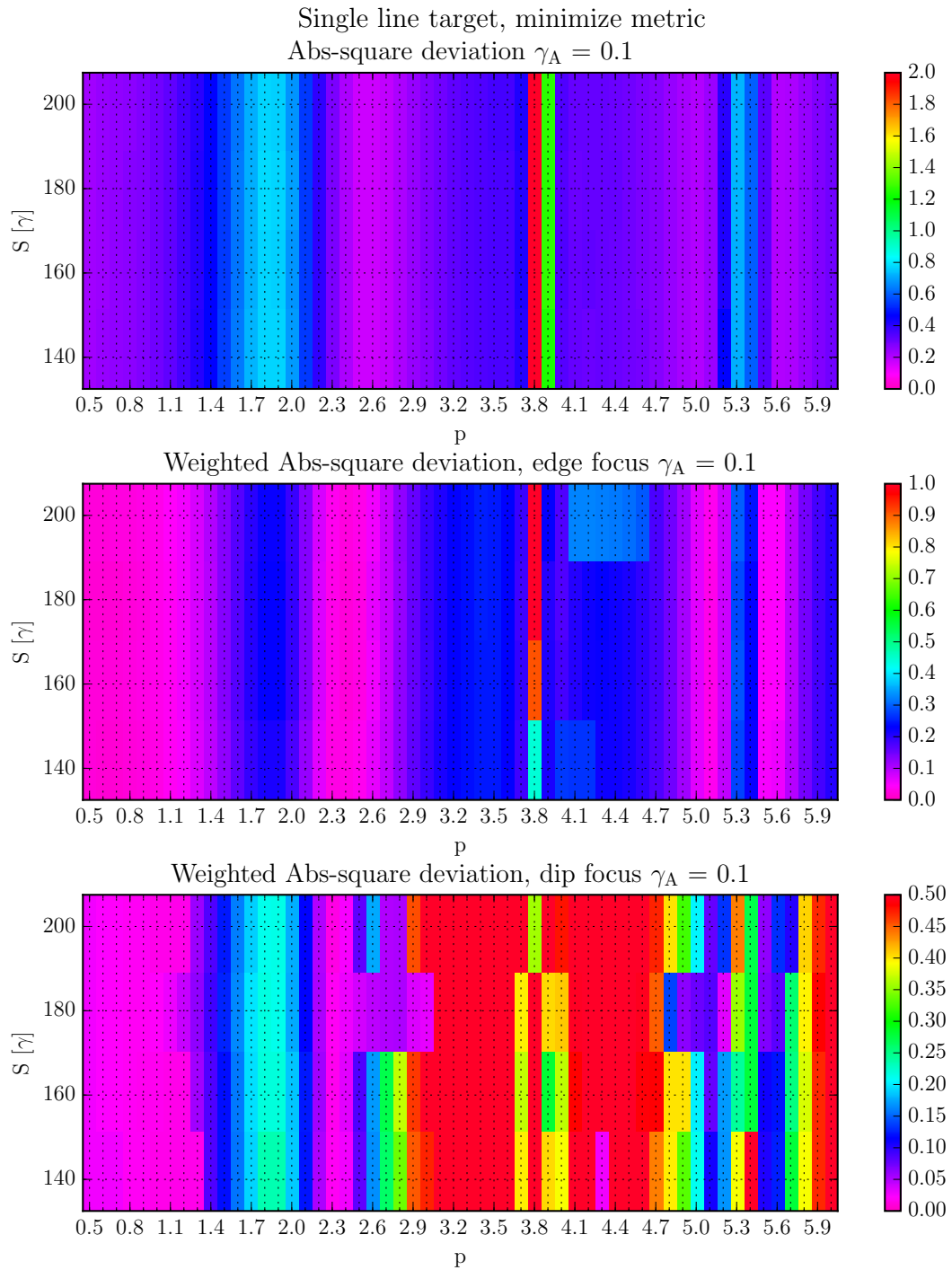


Figure 5.3.: Rating of the different metrics for the reconstruction of the energy spectrum of the single line target. The average times are optimized to minimize the rating of each metric. A lower number implies a better match of the reconstructed spectrum compared to the original spectrum. γ_A has been fixed to $\gamma_A = 0.1$. For the first two metrics there is almost no dependency on S . The dependency on p is clearly visible. For further discussion refer to the main text.

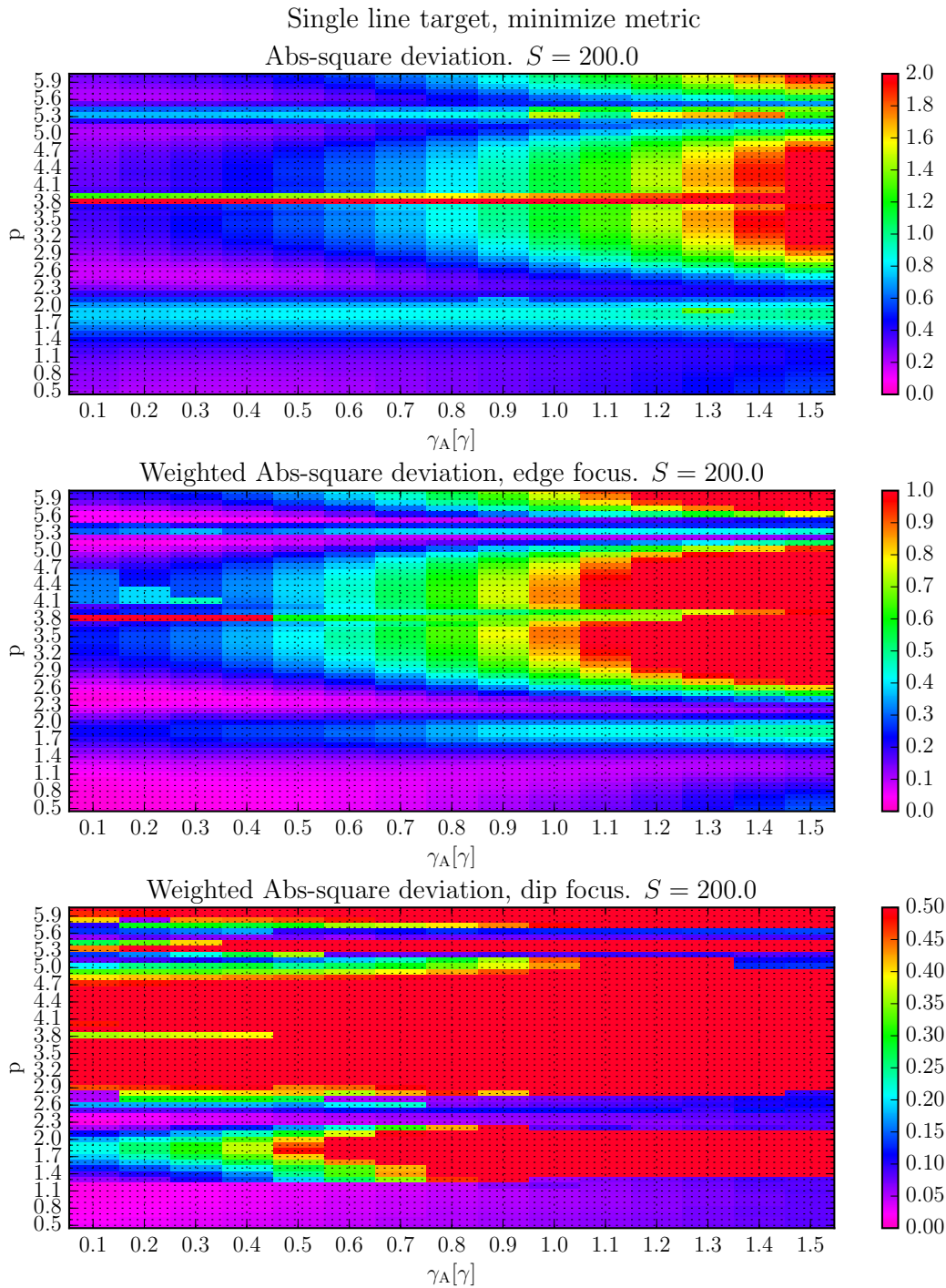


Figure 5.4.: Rating of the different metrics for the for the reconstruction of the energy spectrum of the single line target. The times are optimized to minimize the outcome of the metric. A lower number implies a better match of the reconstructed spectrum compared to the original spectrum. S has been fixed to $S = 200$. The dependencies on γ_A and p are clearly visible in clear areas, with good ratings and clear ones with bad ratings. For further discussion refer to the main text.

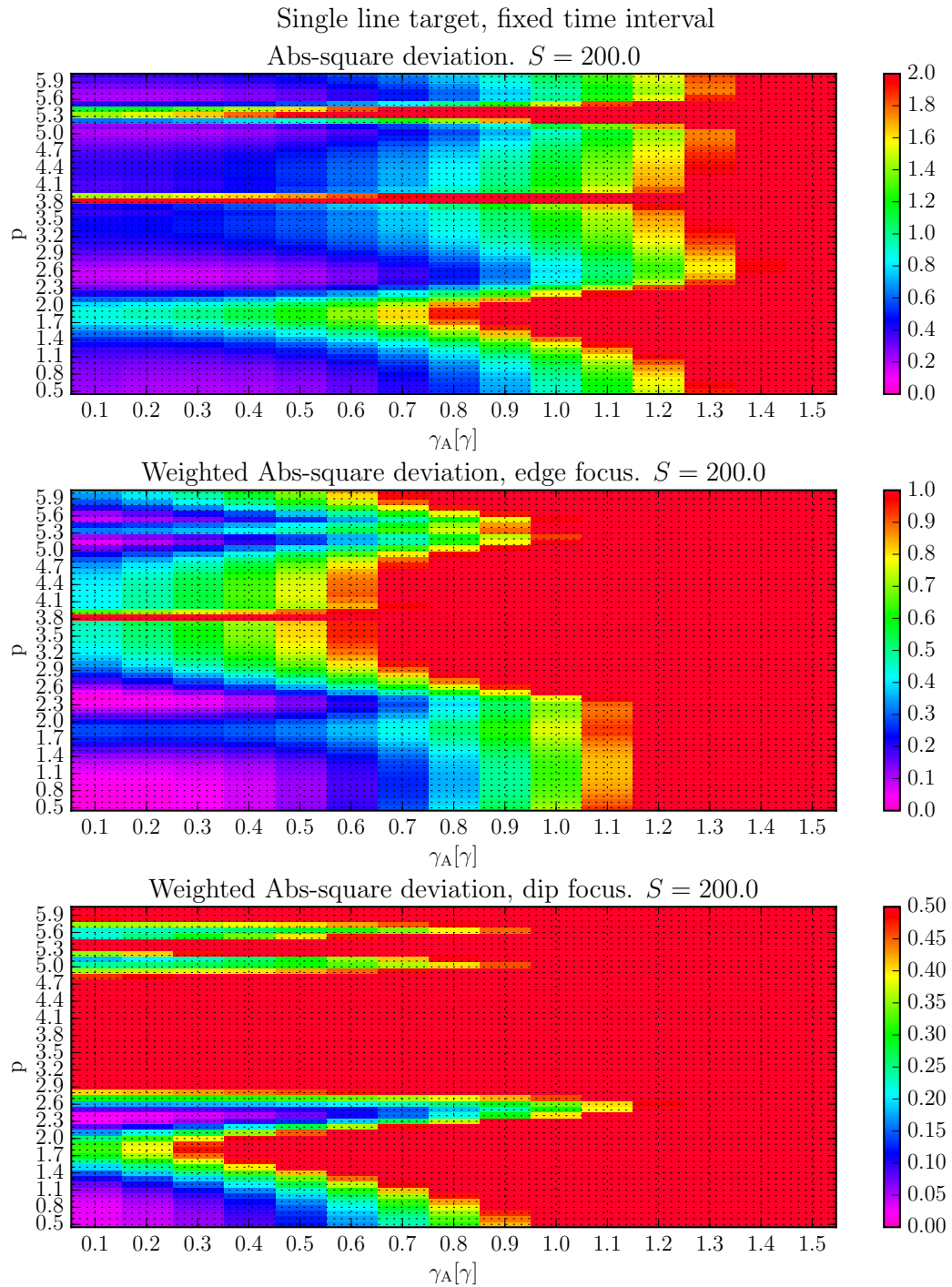
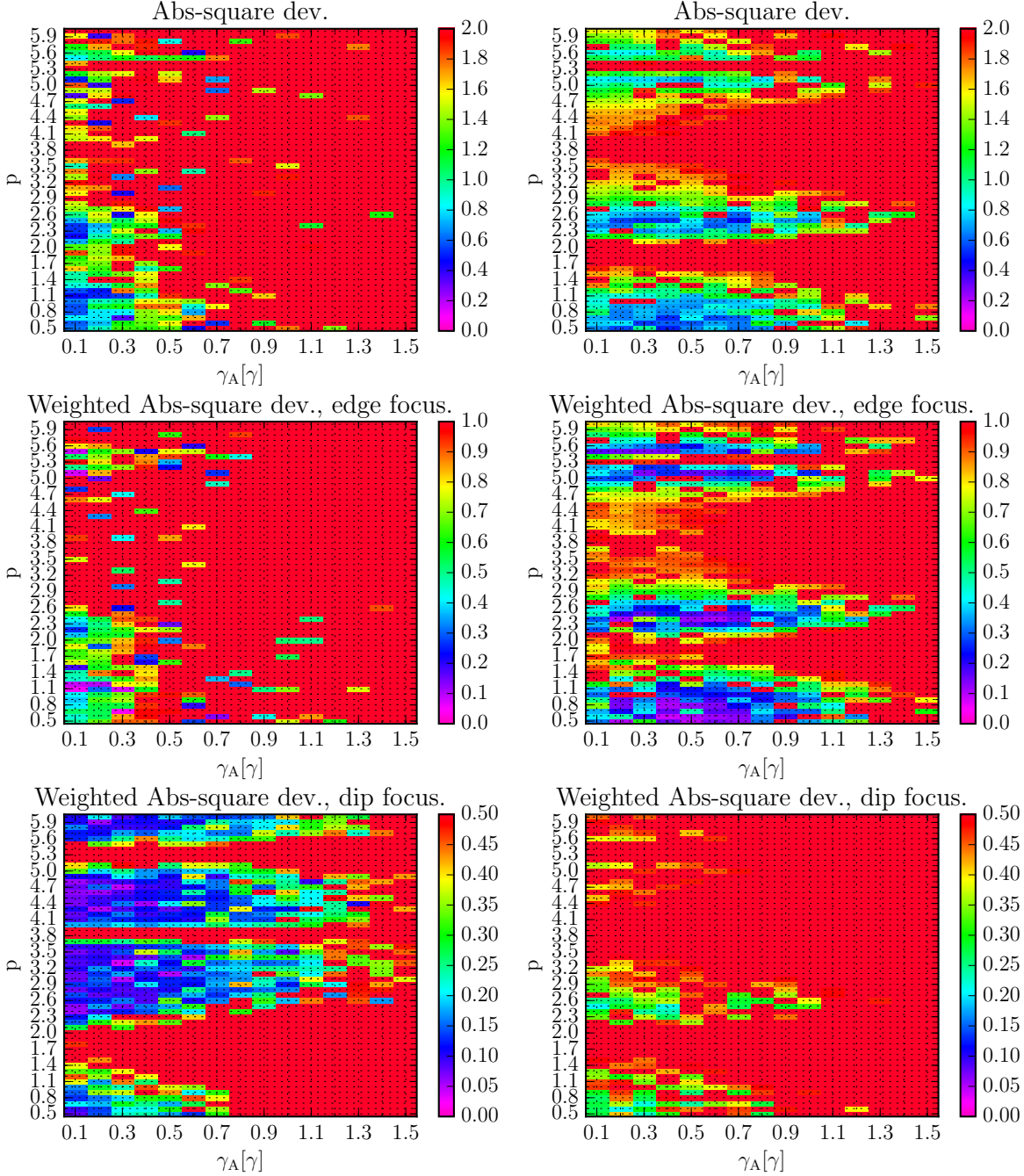


Figure 5.5.: Rating of the different metrics for the for the reconstruction of the energy spectrum of the single line target. For each metric, the average times are set to a fixed times. A lower number implies a better match of the reconstructed spectrum compared to the original spectrum. S has been fixed to $S = 200$. It is visible that there are parameter ranges for which the reconstruction works good and other ones for which it is really bad. For further discussion refer to the main text.

Single line target, symmetry and edge criteria, $S = 200.0$ Double line target, symmetry and edge criteria, $S = 200.0$



(a) Ratings for the single line target.

(b) Ratings for the double line target.

Figure 5.6.: Rating of the different metrics for the single line (a) and double line target(b). The average time interval has been determined by the ab initio algorithm. A lower number implies a better match of the reconstructed spectrum compared to the original spectrum. S has been fixed to $S = 200$. Only in a small parameter range the algorithm works well for the first two metrics. For further discussion refer to the main text.

5.2.3. Conclusions from the Parameter Analysis

So far, the Oscillation-drive have been examined systematically for two different targets. The tools for this examination are three different metrics. Each of which focus on a different part of the spectrum. One on the edge, one on the dips and one rates the whole spectrum equally.

An important point for the reconstruction is the determination of the times over which the average is taken. To find these times different methods have been developed. The first one works the best. However, it requires the knowledge of the original spectrum. Therefore, this method cannot be used in an experiment where the spectrum is supposed to be measured. However, this algorithm can be used to determine a time interval via a simulation within a robust parameter area and use these times for all other parameters in an experiment. The third presented possibility was to use a ab initio algorithm which can use the criteria that the spectra have to converge to unity at the edge. Furhtermore, if available, the symmetry of the spectrum can be taken into account as well.

The conclusions of this chapter can be divided into two parts. The first point refeers to the parameter analysis. The second refers to the choice of the average interval.

Parameter analysis For the choice of γ_a , all analysis revealed the same: The smaller γ_a compared to the target, the better is the reconstruction. For a possible experiment this means that it is desirable to choose an analyzer foil with a linewidth as small as possible.

For the choice of the piezo oscillation amplitude p , values for p which yield good ratings for all metrics and time intervals could be found. The possible values of p with a good reconstruction are, $p \in \{[0.8, 1.3], [2.3, 2.5], 5.1, 5.5\}$. However, not all of those are recommendable for an experiment, because it is desirable to select p in a range where it is not sensitive to a deviation from its optimal value, such that the reconstruction is practically robust. By this criteria $p \approx 5.1$ and $p \approx 5.5$ is not a good choice. The choice between the $p \in [0.8, 1.3]$ and $p \in [2.3, 2.5]$ is not as obvious as it might appear at a first glance. The robustness within the first range is higher than within the second range. This is very distinct in figure 5.4 and can be seen as well in 5.5, especial for the weighted criteria with focus on the edge. However, the rating is slightly better in the second interval. At $p = 2.4$ and $\gamma_A = 0.1$ the rating of the metric is 0.216. At $p = 0.8$ and $\gamma_A = 0.1$, the rating is 0.265 .

For S the constraint that $S > 5l$ have been found. It is necessary that this condition is adhered, otherwise, there is an overlap of the different contributions in ν -space.

Averaging time interval The second important conclusion from this section is about the average time interval. The rating of the metric and therefore the quality of the reconstruction depends on the interval over which the average is taken. This can be seen

by comparing figure 5.4 and figure 5.5. In figure 5.4, the areas of good reconstruction are larger than in the figure 5.5. For figure 5.4 a optimization of the integration interval, by optimizing the result of each metric, have been done, whereas for 5.5, for all parameters the same time interval have been used. This means, that which a optimized time interval, the reconstruction is more robust.

This rises the question how the optimization for each parameter could be done in an experiment. For this purpose the ab initio algorithm using edge convergence and symmetry (if available) has been developed. However, as it is apparent in figure 5.6, the ratings for the reconstruction are not good, using this algorithm. Nevertheless, it can be seen, that at around $p = 2.4$ and $p = 0.8$ for small γ_A , this algorithm returns some time intervals for which the rating are in the lower range of the rating scale. Hence, this approach can work in principle, however, some further improvement is required to allow for practical applicability.

Another method is to simulate the experiment and determine the averaging times using the algorithm which minimizes the metric. These times can then been used for the data of the experiment. As it can be seen in figure 5.5, the reconstruction is still good within the discussed parameter ranges of p and γ_A even if the times are not optimized posteriori.

To summarize, this means, that a fixed time interval so far is the best method for experimental spectral reconstruction using the oscillation drive.

If, however, the improvements to the ab initio algorithm are successful, this would be the preferred choice.

For the rest of the parameters it has been found, that γ_A is desirable to choose as small as possible. However, for an experiment there have to be noted, that an analyzer with a small linewidth lowers the count rate. Therefore, this is a optimization between count rate an accuracy. The value of S hav to be as large as possible but in any case larger than $5l$. For p , there are two parameter ranges which are good. The preferred choice is $p \in [2.3, 2.5]$ because there the best reconstructions are expected. The second choice is $p \in [0.8, 1.3]$ because there, the reconstruction is still good, and more robust to parameter variations, which makes the setup easier to adjust experimentally.

5.3. Comparison of the Oscillation-drive with the Doppler-drive

As mentioned at the beginning of the chapter, there are already well-established methods to determine the energy spectrum of a target. To show, that the Oscillation-drive can provide a practically relevant alternative to those methods, it is compared with the late time integration, using a Doppler-drive. It is important to note, that only the

reconstruction of the spectrum of the Oscillation-drive is compared with the Doppler-drive. This is, because is is not possible to reconstruct the spectral complex phase with the Doppler-drive. Therefore it cannot be compared.

5.3.1. Short Theory of Late Time Integration with Doppler-drive

The principle of the Doppler-Drive is similar to the Oscillation-drive. The target, one want to measure, is hit by the radiation firstly. After the target there is an analyzer foil. As an analyzer usually a single line absorption foil is used, as we have also considered for the Oscillation-drive. A frequently used material for ^{57}Fe experiments is a stainless steel foil enriched in ^{57}Fe [21, 56, 59]. In contrast to the Oscillation-drive, it is mounted on a Doppler-drive instead of a piezo. The Doppler-drive is a device which moves with velocity v_D . Due to the Doppler-effect, the frequencies ω of the spectrum, seen by an observer is rest, are shifted by the value Δ_D to [60],

$$\omega' = \omega \left(1 + \frac{v_D}{c}\right) = \omega + \Delta_D, \quad (5.5)$$

where c denotes the speed of light in vacuum. Denoting $\hat{R}_T(\Delta)$ as the target spectrum again and $\hat{R}_A(\Delta - \Delta_D) = \exp\left(\frac{-ib_A}{\Delta - \Delta_D + i\frac{\gamma_A}{2}}\right)$ as the analyzer spectrum, the electrical field measured at the detector is,

$$\begin{aligned} \hat{E}(\Delta, \Delta_D) &= \hat{E}_{\text{in}}(\Delta) \cdot \hat{R}_T(\Delta) \cdot \hat{R}_A(\Delta - \Delta_D) \\ &= 1 \cdot \hat{R}_T(\Delta) \cdot \left[1 + \left(\exp\left(\frac{-ib_A}{\Delta - \Delta_D + i\frac{\gamma_A}{2}}\right) - 1\right)\right]. \end{aligned} \quad (5.6)$$

In this equation, the analyzer foil has been split into its prompt part (1) and to its scattered part ($\exp(\dots) - 1$). As a consequence, its form is quite similar to equation 4.4 now, but without the sum and α_n . Similarly to the oscillation drive, the following theoretical model is based on the sensing head approximation (4.6). Applying this, it is possible to calculate the measured intensity in the time domain [45],

$$\begin{aligned} I(t, \Delta_D) \propto |E(t, \Delta_D)|^2 &= \left|R_T(t) + \hat{R}_T(\Delta_D)e^{-i\Delta_D t}A(t, \tau)\right|^2 \\ &= |R_T(t)|^2 + \left|\hat{R}_T(\Delta_D)e^{-i\Delta_D t}A(t, \tau)\right|^2 + \\ &\quad 2 \cdot \text{Re}\left(R_T^*(t)\hat{R}_T(\Delta_D)e^{-i\Delta_D t}A(t, \tau)\right), \end{aligned} \quad (5.7)$$

where $A(t, \tau) = -\sqrt{\frac{2\pi b}{t-\tau}}e^{-\frac{\gamma}{2}(t-\tau)}J_1\left(2\sqrt{b(t-\tau)}\right)\Theta(t-\tau)$. The approximation (4.6) requires the width of the target spectrum to be much larger than the relevant spectral width

of the analyzer. Since a larger width in the spectral domain implies that its associated decay rate is much faster, one can argue that $|R_T(t)|^2$ and $\text{Re} \left(R_T^*(t) \hat{R}_T(\Delta_D) e^{-i\Delta_D t} A(t, \tau) \right)$ decay much faster than $\left| \hat{R}_T(\Delta_D) e^{-i\Delta_D t} A(t, \tau) \right|^2$ due to the narrow spectral width of $\hat{R}_A(\Delta)$. For this reason, an integration over late times is approximately proportional to the absolute square of the target spectrum [45],

$$|R_T(\Delta_D)|^2 \propto \int_{t_1}^{t_2} I(t, \Delta_D) dt. \quad (5.8)$$

5.3.2. Evaluation Using the Metrics

The reconstruction of the Doppler drive method, strongly depends on the integration interval $[t_1, t_2]$, similar to the Oscillation-drive. Therefore to have an equal comparison with the oscillation drive, the times have been determined using the same approach as for the Oscillation-drive. Furthermore, the time window of the simulation has been restricted to $[15 \text{ ns}, 380 \text{ ns}]$ as well. Therefore the conditions under which the two methods are compared are exactly the same. Due to the only remaining parameter one can vary, being γ_A , the plots are 2 dimensional instead of contour plots.

In figure 5.7, ratings of the different metrics for both, the Doppler-, and the Oscillation-drive are plotted, using the algorithm which improves the time interval to the best outcome of every metric (see section 5.1.2). This is done for the single line and for the double line target. One can see, that for small values of γ_A , implying a small width of the analyzer in the frequency domain, the Doppler-drive is comparable to the Oscillation-drive. However, as γ_A rises, the reconstructions of the Doppler-drive get worse much faster than the reconstructions of the Oscillation-drive do. Interestingly, considering a single line target, the ratings of the weighted metric with focus on the dip, of Oscillation-drive are comparable with the one of the Doppler drive. Considering a double line target, the ratings of the Doppler-drive are better.

In figure 5.8, the same analysis has been performed, but the time interval has been fixed for all values of γ_A . The observations are similar to the case of optimized times. For the metric without weighting and for the metric with focus on the edge, for small γ_A the ratings for the Oscillation-drive are similar to the ratings of the Doppler-Drive. For an increasing value of γ_A , the ratings of the Doppler-Drive increases more quickly than the one of the Oscillation-Drive.

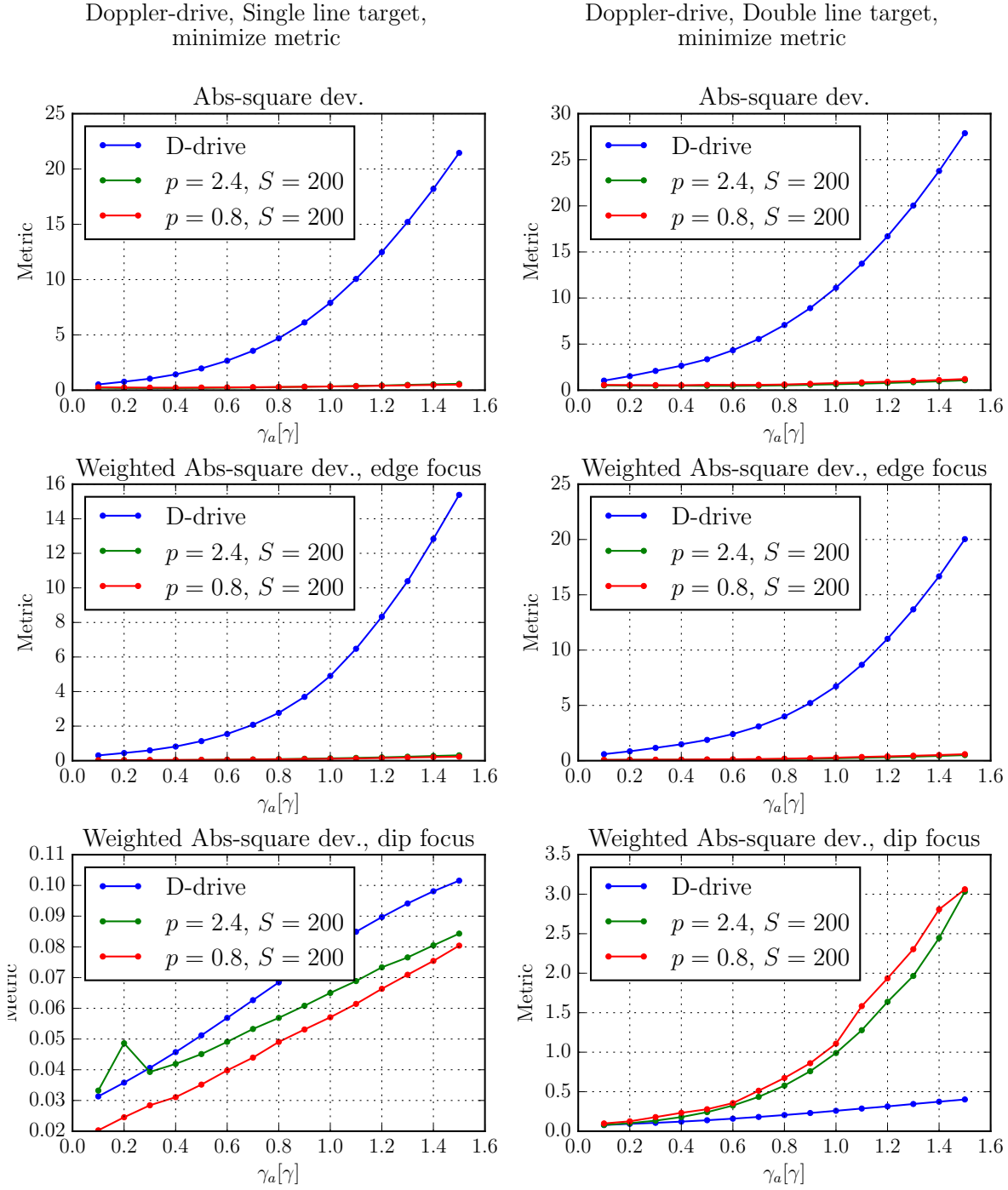
However, for the metric with focus on the dips, this changes. For small γ_A both methods are comparable, whereas, the Doppler-drive is better the larger γ_A . This can be illustrated by, comparing the reconstructions of both methods. In figure 5.10b, the reconstruction of the Doppler-drive is plotted. The green curve is generated using the times which have been optimized by the metric minimization algorithm to give the best

reconstruction. In figure 5.1b, the red curve is analogous, but reconstructed with the Oscillation-drive.

In figure 5.9, the ab initio algorithm which uses the convergence at the edge and the symmetry, is used to determine the average times. In this case, the Doppler-drive is worse in every case. This is not surprising if the results of the cases before are taken into account. They revealed, that the Doppler-drive is good for reconstruction of the dip but not at the edge of the spectrum. However, the ab initio algorithm is partly based on the convergence at the edge. If the convergence is not given there, it is quite difficult for the algorithm to work properly.

The summary of this analysis is that the Oscillation-drive is better than the Doppler-Drive if the whole spectrum is weighted equally and if the focus of the reconstruction is on the edge of the spectrum. Especially, if γ_A is increased, the Oscillation drive, works better. If, however, the reconstruction of the dip is mainly taken into account to rate the quality of the reconstruction, the Doppler-drive becomes better, and is more robust, if γ_A is increased. To get a intuition, of how the reconstructed spectrum looks like, if the the weighted metric with dip focus returns a good value, the reconstructions of the Doppler-drive are plotted in figure 5.10. In (b), it can seen quite good, why the metric with focus on the dip returns a low rating, whilst the others do not. However, if such a reconstruction was the result of an experiment, it would be impossible to make a reliable statement about the unknown target.

5.3. Comparison of the Oscillation-drive with the Doppler-drive



(a) Use of the single line target.

(b) Use of the double line target.

Figure 5.7.: Comparison of the rating of the metrics for the Doppler-drive (blue curve) and the Oscillation drive (green and red curve). The average time interval for the Oscillation drive have been chosen to minimize each metric. For larger values of γ_A the Oscillation drive is better than optimal Doppler-drive for the first two metrics. For the last metric, the Doppler-drive is better.

5. Evaluation Of the Oscillation Drive

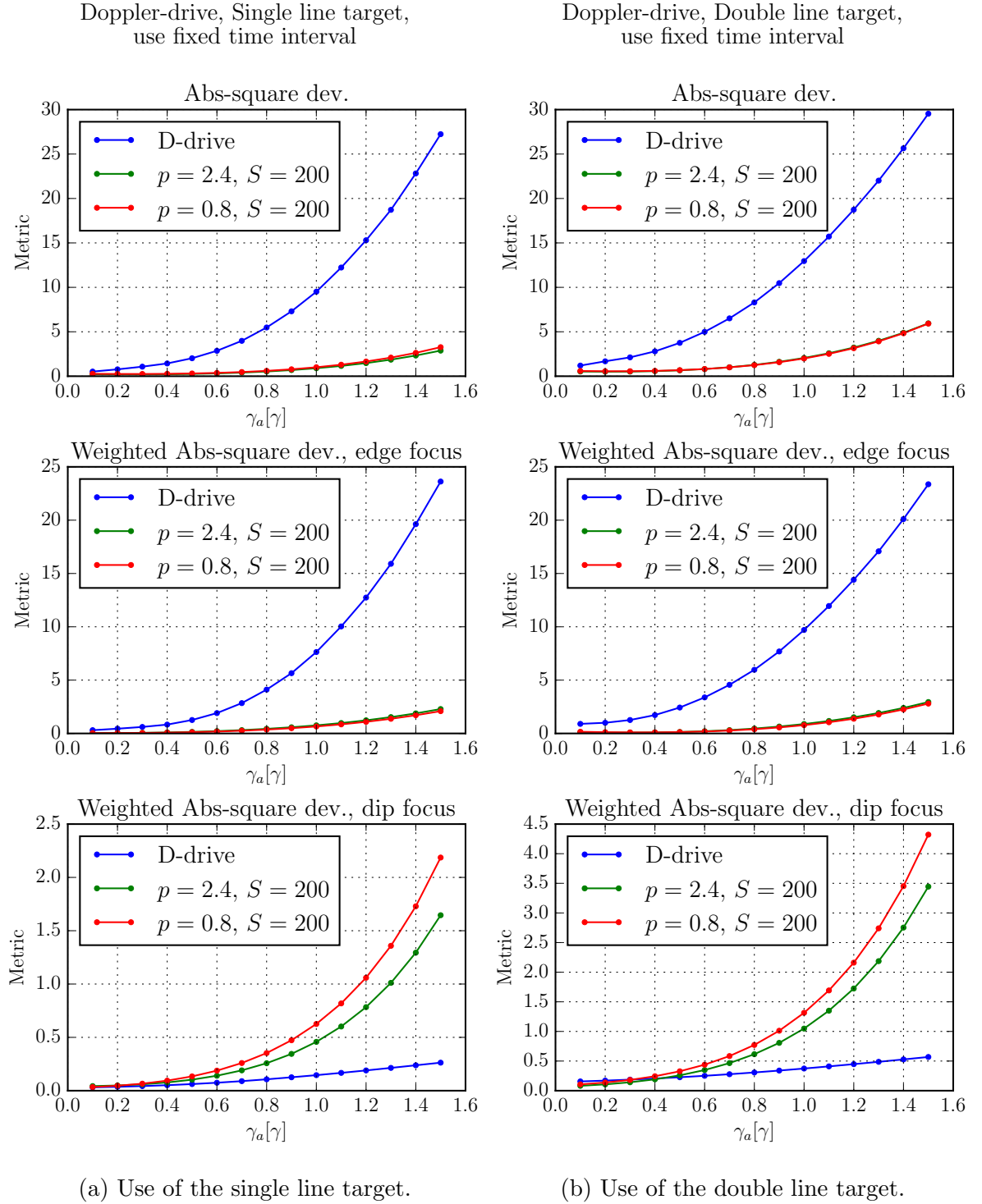


Figure 5.8.: Comparison of the rating of the metrics for the Doppler-drive (blue curve) and the Oscillation drive (green and red curve). The average time interval for have been fixed for all values of γ_A . For larger values of γ_A the Oscillation drive is better than optimal Doppler-drive for the first two metrics. For the last metric, the Doppler-drive is better.

5.3. Comparison of the Oscillation-drive with the Doppler-drive

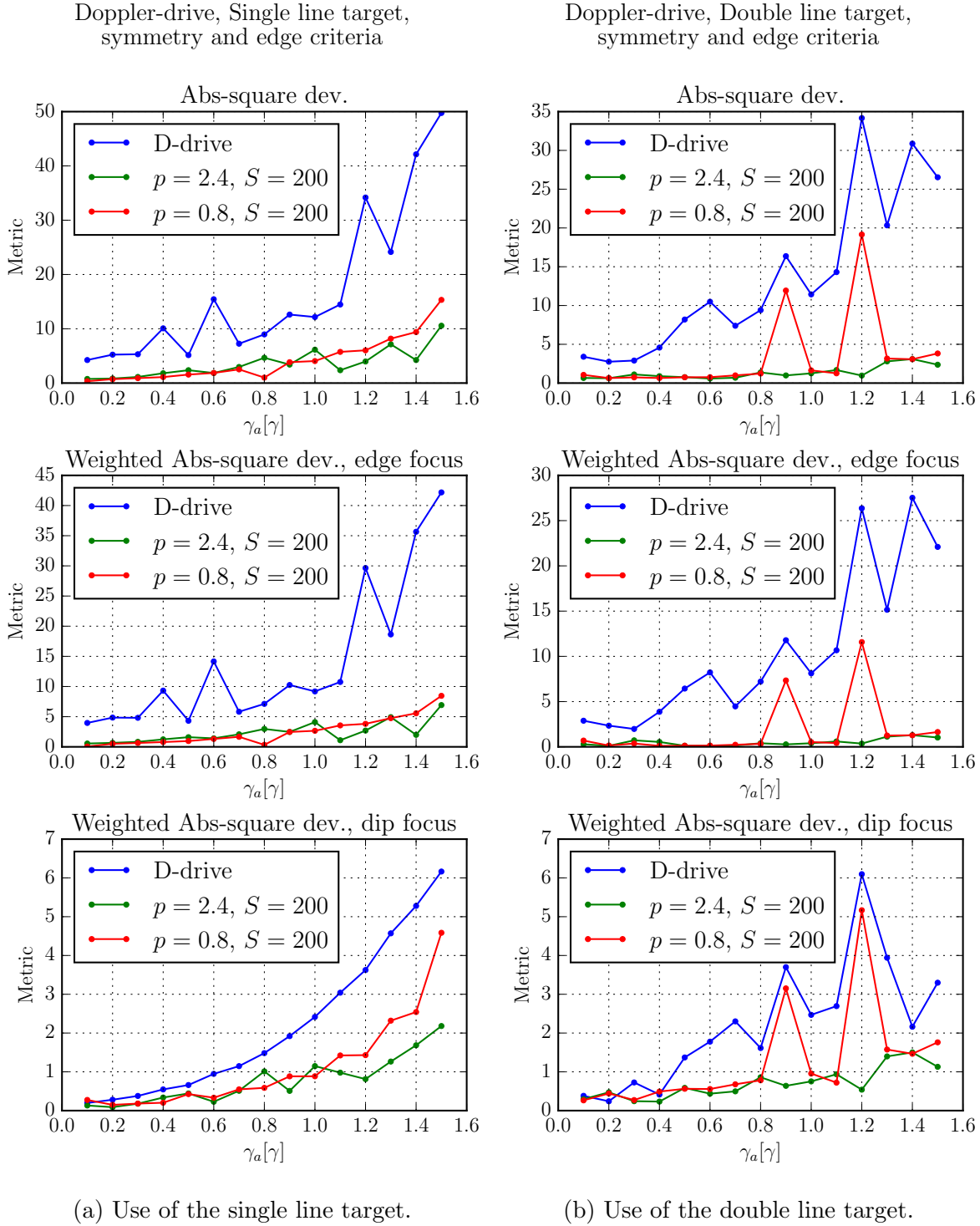


Figure 5.9.: Comparison of the rating of the metrics for the Doppler-drive (blue curve) and the Oscillation drive (green and red curve). The average time interval was calculated by the ab initio algorithm.

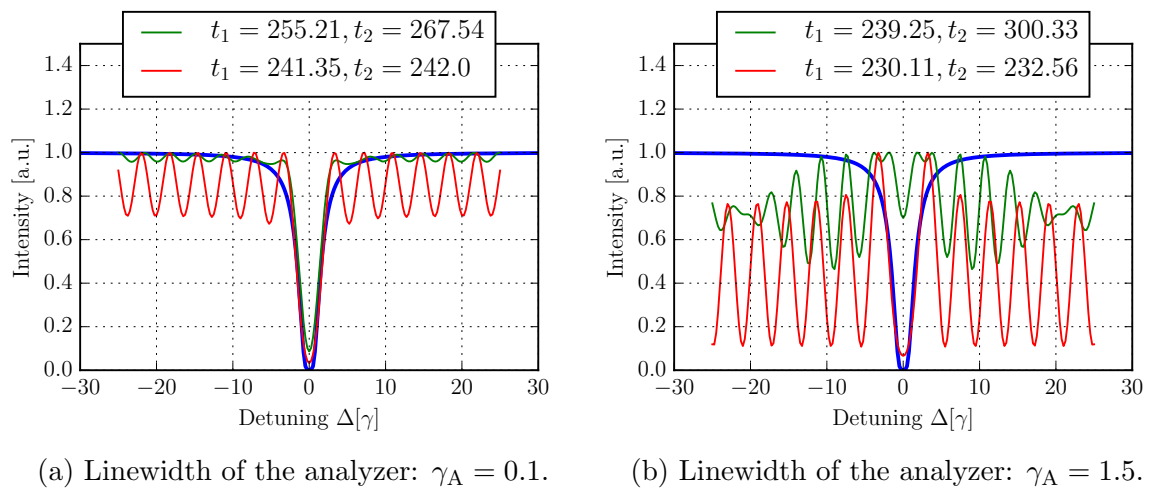


Figure 5.10.: Reconstructions of the Doppler drive, for the case of two different linewidth for the analyzer. The blue curve is equal to $|\hat{R}_T|^2$. The time interval for the green curve is determined by the metric minimization algorithm using the metric without focus. The times of the red curve have been determined using the same algorithm but using weighted norm focusing on the dip. In case (b) it is difficult to see any similarities with the original spectrum.

5.4. Theoretical Optimum of the Doppler-drive: Convolution Theorem

The analysis of the Doppler-drive showed that the quality of reconstruction depends strongly on the integration time interval similar to the Oscillation-drive. Furthermore, it was shown that the quality of reconstruction strongly depends on the chosen time interval. From this the question arises, what would happen if the whole time spectrum from $t_1 = 0$ ns to $t_2 = \infty$ ns was available. If the complete signal was available, this would be the theoretical optimum for the Doppler-Drive method, as it uses as much information, as theoretically are available. As already said, in an experiment there is the technical limitation to measure the first few ns, because the APDs are overloaded by the non-resonant scattered photons. For the upper limit there is the restriction that the signal rate decreases exponentially, which has the consequence that the probability to count a photon at late times gets very small. Acquiring enough statistics at such late times would lead to a enormous increase in the measuring time.

In the following theoretical analysis of the optimal case these practical limitations will be ignored.

For this theoretical analysis, first a analytical calculation is made. The result is then verified by an numerical calculation. For this, the same setup as for the Doppler-drive in section 5.3 is used. Hence, a system of two foils in a row is assumed.

Analytical analysis. The first foil is the target, whose energy spectrum $\hat{R}_T(\Delta)$ shall be measured. The second foil is the analyzer foil, mounted on a Doppler-drive. The Doppler-drive shifts its resonance frequency, for an observer at rest, by Δ_D . Its complex response function will be denoted as $\hat{R}_A(\Delta - \Delta_D)$. The analyzer is described by a single line absorption foil (2.34). Therefore the intensity at the detector in time domain can be written as,

$$I(t, \Delta_D) \propto |E_D(t, \Delta_D)|^2 = \left| \int_{-\infty}^{\infty} \frac{d\Delta}{\sqrt{2\pi}} \hat{R}_T(\Delta) \hat{R}_A(\Delta - \Delta_D) e^{-i\Delta t} \right|^2. \quad (5.9)$$

Usually, in the case of late time integration the intensity is integrated between two finite time limits, t_1 to t_2 . In the ideal case considered here the range is extended to the interval $t_1 = 0$ to $t_2 = \infty$,

$$\int_0^{\infty} I(t, \Delta_D) dt \propto \int_0^{\infty} |E_D(t, \Delta_D)|^2 dt. \quad (5.10)$$

Since for negative times, the signal is zero, it is possible to extend the integration range to the interval $t_1 = -\infty$ to $t_2 = \infty$. With this, Parsevals theorem can be employed [39], which says that the integration from $-\infty$ to ∞ of the absolute square of a complex

signal in time domain is equal to the integration of the absolute square in the frequency domain. This is equal to the statement, that the total energy in the time and the frequency domain is the same. Using this, equation (5.10) becomes,

$$\int_{-\infty}^{\infty} |E_D(t, \Delta_D)|^2 dt = \int_{-\infty}^{\infty} |\hat{E}_D(\Delta, \Delta_D)|^2 d\Delta = \int_{-\infty}^{\infty} |\hat{R}_T(\Delta) \hat{R}_A(\Delta - \Delta_D)|^2 d\Delta. \quad (5.11)$$

For the following the response of the analyzer foil is split in its prompt part and in the scattered part, denoted as $\hat{R}_{AS}(\Delta - \Delta_D)$, similarly to equation (5.6). In the energy domain this is equal to subtract the baseline, which originates from the prompt pulse, and adding it manually, again. Hence the absolute square in the integrand can be rewritten as,

$$\begin{aligned} \int_{-\infty}^{\infty} |E_D(t, \Delta_D)|^2 dt &= \int_{-\infty}^{\infty} \left| \hat{R}_T(\Delta) \right|^2 \cdot \left| 1 + \underbrace{\left(\hat{R}_A(\Delta - \Delta_D) - 1 \right)}_{\hat{R}_{AS}(\Delta - \Delta_D)} \right|^2 d\Delta \quad (5.12) \\ &= \int_{-\infty}^{\infty} \left[\left| \hat{R}_T(\Delta) \right|^2 + \right. \\ &\quad \left. \left| \hat{R}_T(\Delta) \right|^2 \left| \hat{R}_{AS}(\Delta - \Delta_D) \right|^2 + \right. \\ &\quad \left. 2 \left| \hat{R}_T(\Delta) \right|^2 \operatorname{Re} \left(\hat{R}_{AS}(\Delta - \Delta_D) \right) \right] d\Delta. \quad (5.13) \end{aligned}$$

Equation (5.13) can be split into three integrals, equal to the three lines. The first one gives a constant C , due to a finite energy range of the target. The second and the third part are basically convolutions [39]. Therefore the integral can be rewritten as,

$$\begin{aligned} \int_{-\infty}^{\infty} |E_D(t, \Delta_D)|^2 dt &= C + \left(\left| \hat{R}_T \right|^2 * \left| \hat{R}_{AS} \right|^2 \right) (\Delta_D) + \\ &\quad 2 \cdot \left(\left| \hat{R}_T \right|^2 * \operatorname{Re} \left(\hat{R}_{AS} \right) \right) (\Delta_D). \quad (5.14) \end{aligned}$$

From this it can be seen, that for an infinite integration range, one would get the addition of two convolutions. The first is a convolution of the absolute square of the target with the absolute square of the resonant scattered part of the analyzer. The second is a convolution of the real part of resonant scattered part with the absolute square of the target.

Assuming now a narrow analyzer, in the ideal case, the analyzer is a δ -peak, the result of the convolution is exactly the the absolute square of the target spectrum, since a convolution of an arbitrary function with an δ -peak returns the function again. Therefore, for small values of γ_A , good reconstructions are expected.

Numerical calculation To check the results of the analytical calculation the convolution of equation (5.14) have been calculated numerically. Furthermore, the system has been simulated. This means, that equation (5.9), is calculated for a grid of Δ_D . For each Δ_D , the outcome is Fourier transformed to time domain. There, the integration over the whole time range is performed, which is numerically equal to the average over the whole available time grid.

For both cases the following parameters have been used. The target foil is described by equation (4.60) with $b_T = 2$ and $\gamma_T = 1$ and $\delta\omega = 5$. The analyzer is described by (2.34) with $b_A = 0.5$ and $\gamma_A = 0.1$.

The results of the simulation as well as of the numerical convolutions are plotted in figure 5.11. The two convolutions are plotted in blue and green respectively. The red curve is equal to $|\hat{R}_T|^2 * |\hat{R}_{AS}|^2 + 2 \cdot |\hat{R}_T|^2 * \text{Re}(\hat{R}_{AS})$, which is basically equation 5.14 without the addition of C .

To compare the data of the simulation and of the numerically calculated convolutions, they have to be normalized. This is done by shifting both in such a way, that their minimal value is equal to zero. After this, they are both divided by their maximal value.

The result of the normalized simulation data is plotted as the dashed pink curve. The normed version of the red curve is plotted in mint green. Both curves show excellent agreement.

To compare the simulation data with the absolute square of the target, it is necessary to mirror the normed data and add the baseline. This have been done in figure 5.12. One can see, that the agreement is good.

To summarize, in the theoretically optimal case, where the signal from $t_1 = 0$ to $t_2 = \infty$ is available, the integration over the time interval $[t_1, t_2]$ results in a curve which matches the absolute square of the target energy spectrum very well. In this case, the maximum of information is available within the framework of the Doppler-drive method. Therefore, one can say, that this method gives the best result which could be achieved using a Doppler-drive. From this insight the question arises, how this ideal Doppler-drive behaves compared to the Oscillation-drive, which has been investigated including the consideration of experimental limits. This will be examined in the next section.

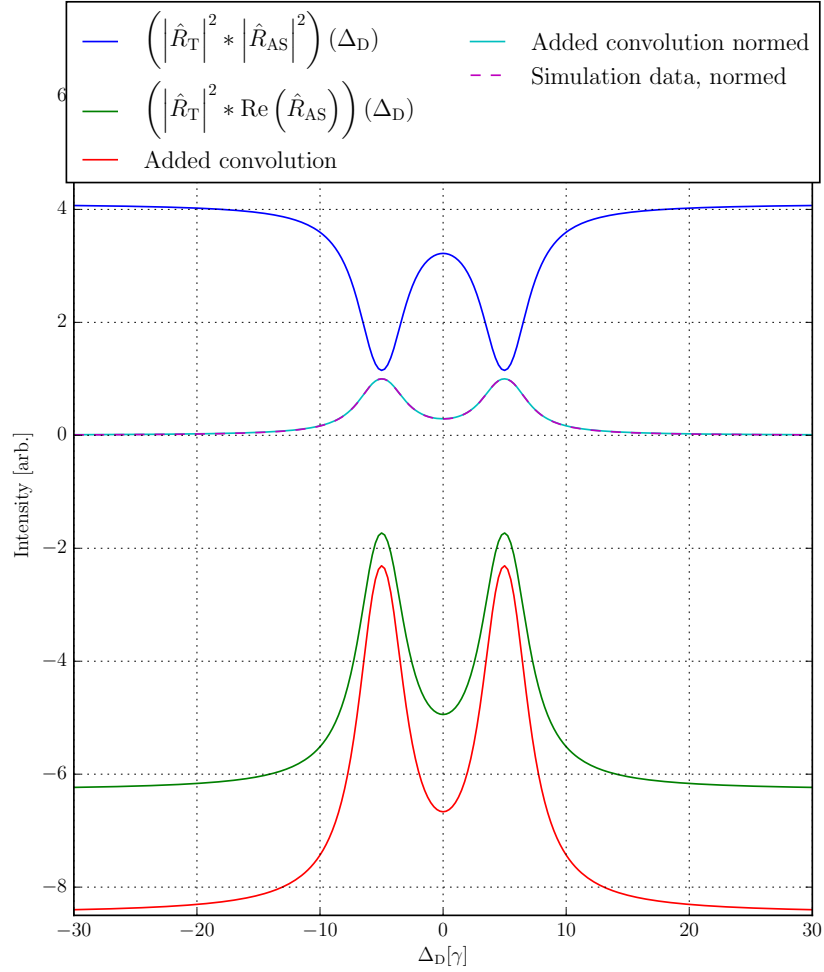


Figure 5.11.: Numerical implementation of the convolutions in equation 5.14. The double line target as well as the analyzer of chapter 4.2 have been implemented and the convolutions have been performed numerically.

The blue and the green curve show the numerically calculated convolutions. The red curve shows the addition of the two convolutions, $|\hat{R}_T|^2 * |\hat{R}_{AS}|^2 + 2 \cdot |\hat{R}_T|^2 * \text{Re}(\hat{R}_{AS})$. The red curve is normalized to unity, which is plotted as the mint green curve. Furthermore the system have been simulated and normed again. The simulation is plotted with the dashed curve. The agreement of simulation and numerical calculation is exact. To reconstruct the spectrum, using the mint green, or the dashed line, the data have to be mirrored, which means multiplied by -1 and then shifted by $+1$ to match the baseline. This is done in figure 5.12.

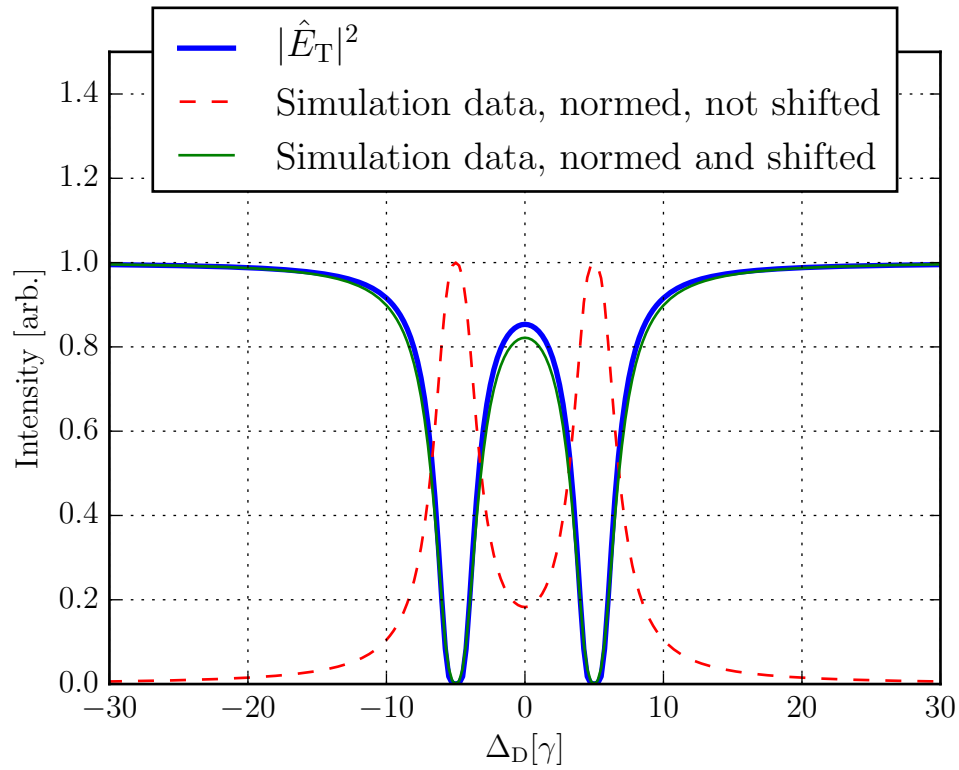


Figure 5.12.: Comparison of the simulation of the convolution theorem with the absolute square of the energy spectrum of the double line target. The dashed curve, is the same as the dashed curve in figure 5.11. It is multiplied with -1 and shifted by $+1$. This is plotted in green. The blue line is equal to the absolute square of the target energy spectrum. As one can see, the agreement is excellent.

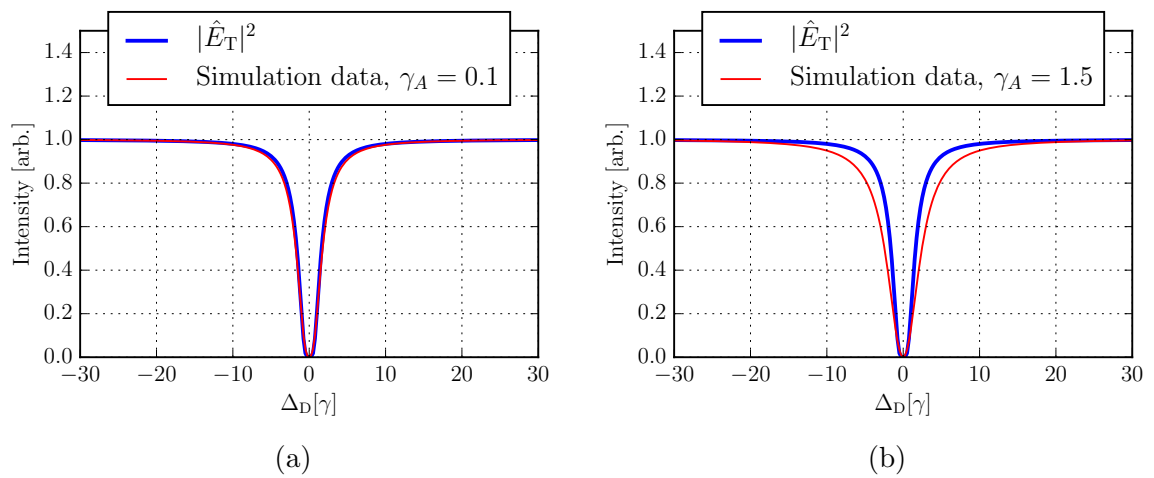


Figure 5.13.: Reconstructions of the ideal Doppler-drive for a single line target and different linewidth of the analyzer. For the larger linewidth (b), the reconstruction is more erode. This leads to a higher rating of the metrics (see figure 5.14). In 5.1b, the reconstruction of the Oscillation-drive using the same analyzer linewidth is plotted (red curve). One can see, that by the naked eye that the deviation is smaller.

5.4.1. Comparison with the Oscillation-drive

In the previous section a theory of the Doppler-drive assuming the availability of the whole time spectrum from $t_1 = 0$ to $t_2 = \infty$ has been developed and numerically tested. It has been showed, that the reconstruction matches with the absolute square of the original spectrum extremely well.

In this section, this theoretical optimum is compared to the Oscillation-drive. Hereby the Oscillation-drive is treated *including* the experimental limitation that the first few ns can not be measured. Furthermore the upper limit is restricted to 380 ns. The theoretically idealized case of the oscillation drive is thus compared to an experimentally feasible scenario of the Oscillation-drive, which provides a strong benchmark for the capabilities of the latter.

The results are plotted in figures 5.14 to 5.16, where the same procedure as in section 5.3.2 has been performed. For this, the three different metrics are calculated for each outcome of the ideal Doppler-drive for different values of γ_A , which is the linewidth of the analyzer foil. In contrast to the procedure in section 5.3.2, the time interval for the Doppler-drive is fixed the theoretically ideal case of running from 0 to ∞ . In the numerical case this means to integrate over the whole time array, which ends at 1500 ns.

Each of the figures differ from each other by the method of how the average time interval for the Oscillation-drive has been determined.

In figure 5.14, the average time interval is determined by the metric minimization algorithm. Therefore in this plots, the best possible time interval for each metric is chosen. As a short reminder, the lower the rating of the metric, the better the reconstruction. For the non-weighted metric, the Doppler-drive is better for small values of γ_A . However, if γ_A increases, the rating for the Doppler-drive increase as well. The same behavior can be seen for the ratings of the Oscillation-drive but the ratings increase not this fast as for the Doppler-drive. Hence, for larger γ_A , the Oscillation-drive can return a reconstruction of the spectrum, with less deviation, from the original spectrum.

For the metric with focus on the edge, the Oscillation-drive is better or equal for all values of γ_A . For the metric with focus on the dips, the Oscillation-drive is worse in the single line case, but better again for larger γ_A .

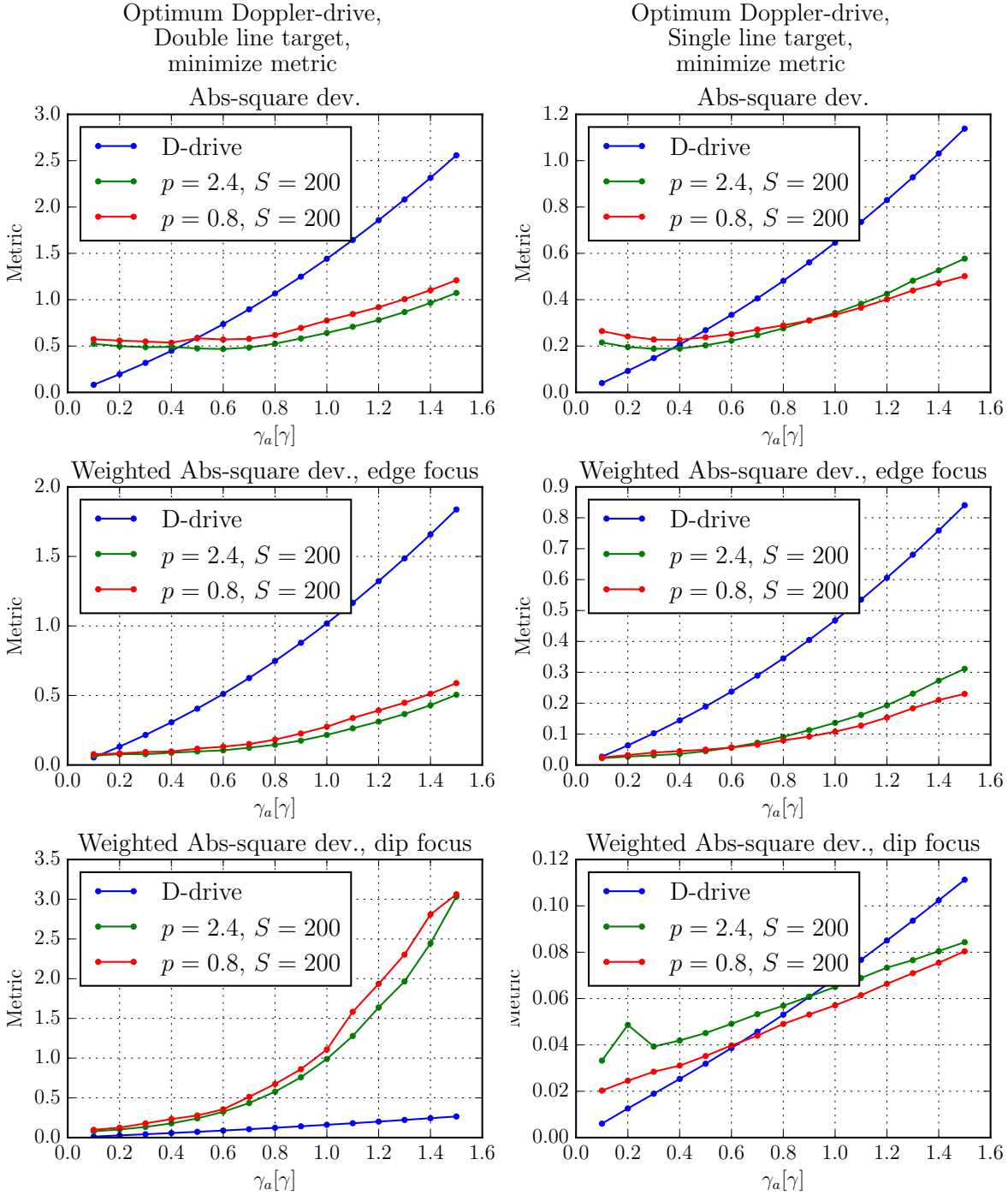
This shows, that the Oscillation-drive can compete with the ideal Doppler-Drive. Especially the less strong dependency of γ_A of the Oscillation-drive is to point out. This can be seen by the comparison of the reconstructions of both methods for large values of γ_A . In figure 5.13 the reconstruction of the optimal Doppler-drive is plotted and in 5.1b the one of the Oscillation-drive. The less deviation from the original target, can be seen with the naked eye.

In figure 5.15 the same analysis is done but with a fixed time interval for the Oscillation-drive. There, the ratings of the Oscillation-drive a almost everywhere higher than the

one of the Doppler-drive. Especially the case of the absolute square metric is interesting. For small γ_A it shows the same behavior like in figure 5.14. However, at $\gamma_A = 0.6$ it starts to raise strongly, whereas in the case, where the time interval is readjusted, it does not raise this fast. This shows again, the dependency of the Oscillation-drive on the averaging time interval. If it is not adjusted, it can't compete this good with the optimal Doppler-Drive.

The main result of this analysis so far ist that the Oscillation-drive can compete with the ideal Doppler-drive, if the integration times are optimized for each value of γ_A .

This shows again, that it is important to have a possibility to determine the averaging time interval. For this purpose, the ab initio algorithm has been developed. The comparison with this method is plotted in figure ???. It can be seen, that for the double line target, this algorithm is good enough, that the results of the Oscillation-drive are comparable with the Doppler-drive and for the weighted metric with focus on the edge, they are even better. The two exceptional peaks for $p = 0.8$ are due to numerical issues, where the algorithm did not converge. Unfortunately, for the single line target, the ab initio algorithm is not as good. However, the double line case shows that it works in principle.



(a) Use of the double line target.

(b) Use of the single line target.

Figure 5.14.: Comparison of the rating of the metrics for the optimal Doppler-drive and the Oscillation drive. The green and the red curve belong to the Oscillation drive, the blue to the Doppler drive. The average time interval for the Oscillation drive have been determined by the algorithm which minimizes the metric. For larger values of γ the Oscillation drive is almost in every case better than optimal Doppler-drive.

5. Evaluation Of the Oscillation Drive

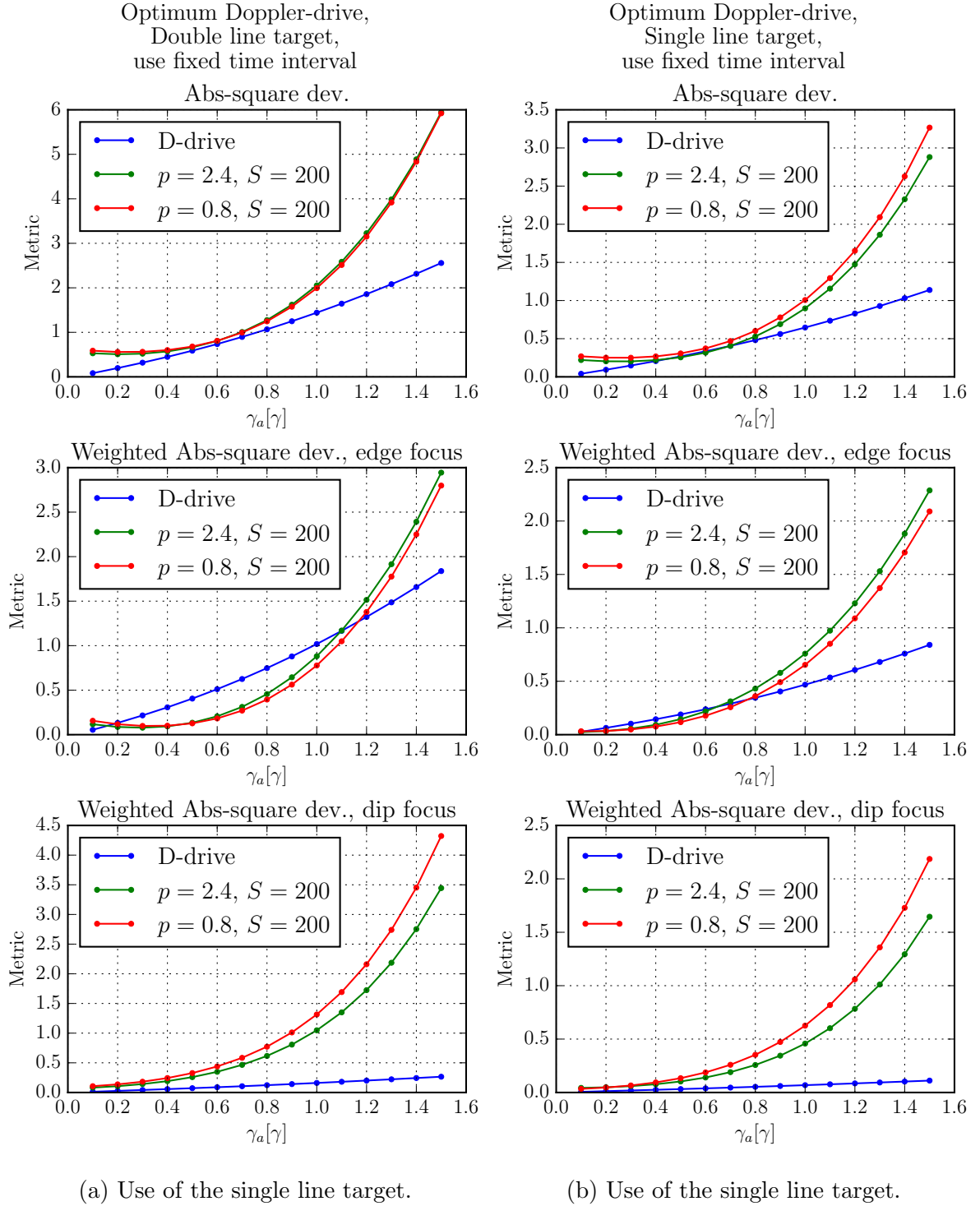
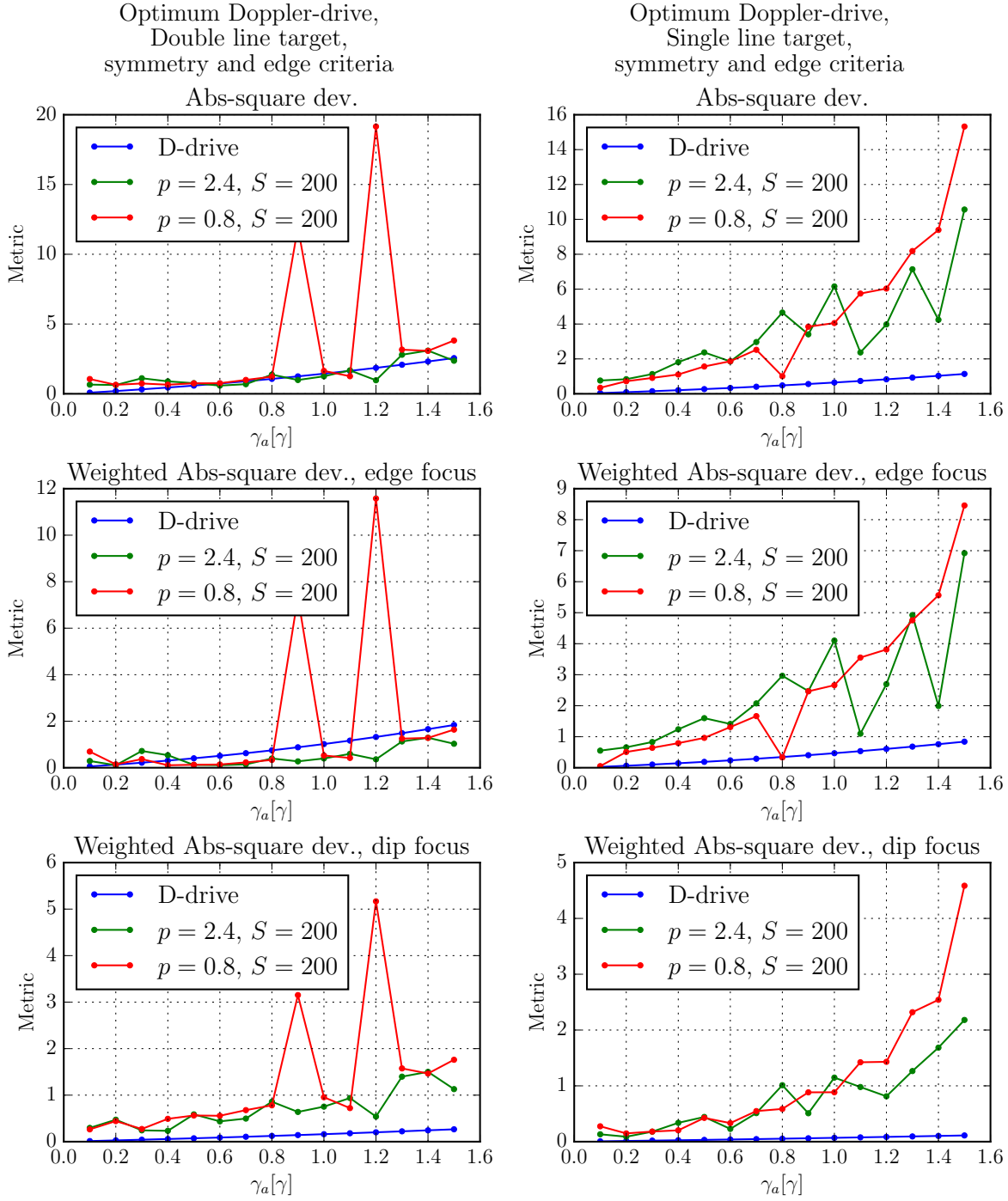


Figure 5.15.: Comparison of the rating of the different metrics for the optimal Doppler-drive and the oscillation drive. The average time for the Oscillation-drive is fixed for all values of γ_A , S and p .



(a) Use of the single line target.

(b) Use of the single line target.

Figure 5.16.: Comparison of the rating of the different metrics for the optimal Doppler-drive and the oscillation drive. The average time for the Oscillation-drive have been determined by the ab initio algorithm using edge convergence and symmetry.

5.5. Evaluation of the Phase

So far the reconstruction of the energy spectrum was discussed in detail. However, an important advantage of the Oscillation-drive is that it can reconstruct not only the spectrum but also provides access to the spectral complex phase of the target. The oscillation drive is particularly interesting in this regard, because no extra effort in the data acquisition or in the analysis of the data is necessary, compared to the case of spectral intensity reconstruction using the oscillation drive. This means that the phase is given for free. It is to note at this point, that, compared to the Doppler-drive, the Oscillation-drive needs to scan the parameter φ_0 additional.

So far the spectral intensity has been discussed and compared in detail with the Doppler-drive. This could lead to the impression, that the phase is not this important and a just by-product. This is not the case. On the contrary, the reason, why the phase has not been discussed above is that all existing methods to determine the spectrum are not able to reconstructed the phase. Therefore the spectral phase reconstruction simply cannot be compared to existing methods.

In the following section, an analysis of the quality of the reconstructed phase in dependency of the parameter γ_A and p is made .

Like it can be seen in figure 4.8b and 4.9b for the reconstruction of the phase it is not explicitly necessary to average over a time interval. Thus, there is no need to use any algorithm or methods to determine a time interval. As a consequence, the unweighted metric, is sufficient to rate the reconstruction.

As already said in section 4.3, the result becomes better, if it is averaged over a time interval. The reason for this is, that for a single point in time, there are small and fast oscillations superimposing the spectra. The position of the maxima with respect to ω_p changes for different times. Therefore it is possible to smooth those oscillations by taking the average over a time interval. Hence, in the following there is an analysis of both targets for a fixed time and for a time average. The fixed time is chosen at $t = 153$ ns, the time interval for the average is [130 ns, 180 ns].

In figure 5.17 the ratings of the metric for the single line target for a fixed time and a average over the time interval [130 ns, 180 ns] are plotted. In figure 5.18 the same is plotted, but for the double line target.

For both targets the reconstruction is good in the same parameter areas as for the spectra. To explain this, the same argument can be used for reconstruction of the the as for the reconstruction of the spectral intensity: They are both based on equation (4.39). To derive this, it is necessary to choose $p = p_0$ such, that $J_0(p_0) \approx 0$ or $J_2(p_0) \approx 0$. The areas of good reconstruction are at those values of p , where one of those conditions is fulfilled. If p is chosen in a way, that this condition is not fulfilled anymore, equation

5.18 turns to (5.4). If function (4.52) is fitted to this function, the outcome of the fit parameters no longer satisfy equation (4.56) and (4.58).

Even though the mechanism is the same for the phase and the spectrum, the reconstruction of the phase is more sensitive to a change of p than the one of the spectral intensity. This can be explained by equation (5.4). For the reconstruction of the phase the offset of the cosine term is needed, whereas for the spectrum the amplitude is used. To get a feeling, of how the addition of two cosines with opposite offset looks, an addition theorem [39] for the case of $J_2(p) = J_0(p)$ can be used,

$$\cos(x + a) + \cos(x - a) = 2 \cos(a) \cos(x). \quad (5.15)$$

The amplitude varies with the offset. But due to the fact, that the amplitude is normalized to unity before the average is taken, the influence of the second cosine to the reconstruction of the spectrum is smaller than for the phase. In contrast to this, for the offset, the second cosine has a big influence.

However, taking the average over a few time sets can cushion this effect. Therefore, for the average, there are larger parameter ranges of good reconstructions.

5.6. Summary of the Oscillation-drive

The Oscillation-drive offers the exciting possibility, to reconstruct the spectrum *and* the phase of an unknown target in energy space at hard X-ray energies with the spectral resolution required for Mössbauer experiments. The main principle of the device is that the first sideband, created by an oscillating foil, is used to scan the target. This is a similar principle to the one employed in the conventional Doppler drive.

The main difference is, however, that in the case of the Oscillation-drive, the oscillation offset φ_0 can be used as an additional and controllable degree of freedom. In this chapter, the reconstructed spectrum have been compared with the reconstruction using a Doppler-drive. The result of this was, that for a narrow banded analyzer, the reconstruction of the Doppler-drive is of similar quality to the one of the Oscillation-drive. For increasing γ_A , the Oscillation-drive returns better reconstructions than the Doppler-drive does.

Since the Doppler-drive depends on several parameters it is important to find out, how theses parameters have to be chosen to give the best result. It has been shown, that for the reconstruction of the phase as well as for the spectrum, the same parameter ranges return good values: The oscillation amplitude p can be chosen within an interval of $p \in [2.3, 2.5]$ or $p \in [0.8, 1.3]$. The linewidth of the analyzer γ_A should be chosen as small as possible. For the shift S , there is the constraint, that it have to be larger than $5l$, where l is half of the range in which the absolute square of the target transmission in energy space deviates from unity.

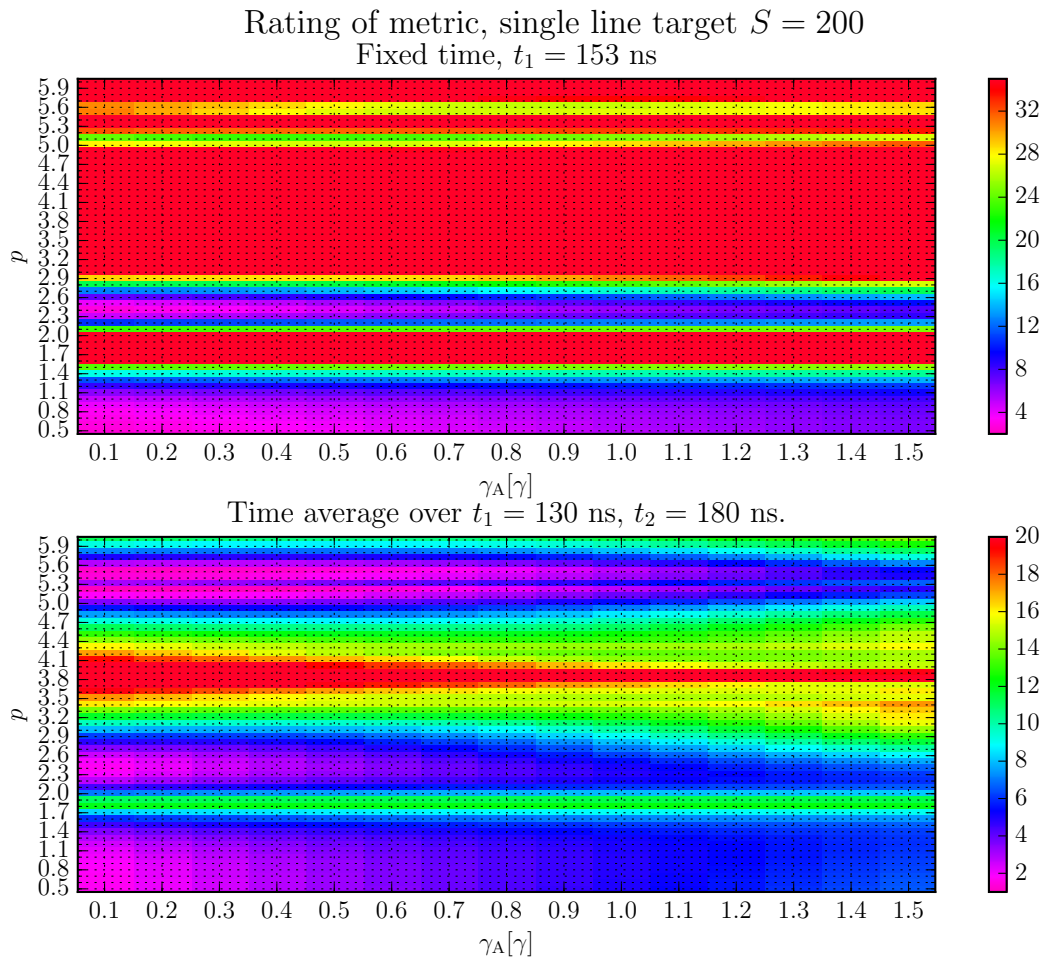


Figure 5.17.: Ratings of the metric for the complex phase of the single line target. One can see the same areas where the reconstruction is good than for the spectrum. However, the quality of reconstruction is more sensible to a change of p . If one averages over time, the areas of good reconstruction become larger.

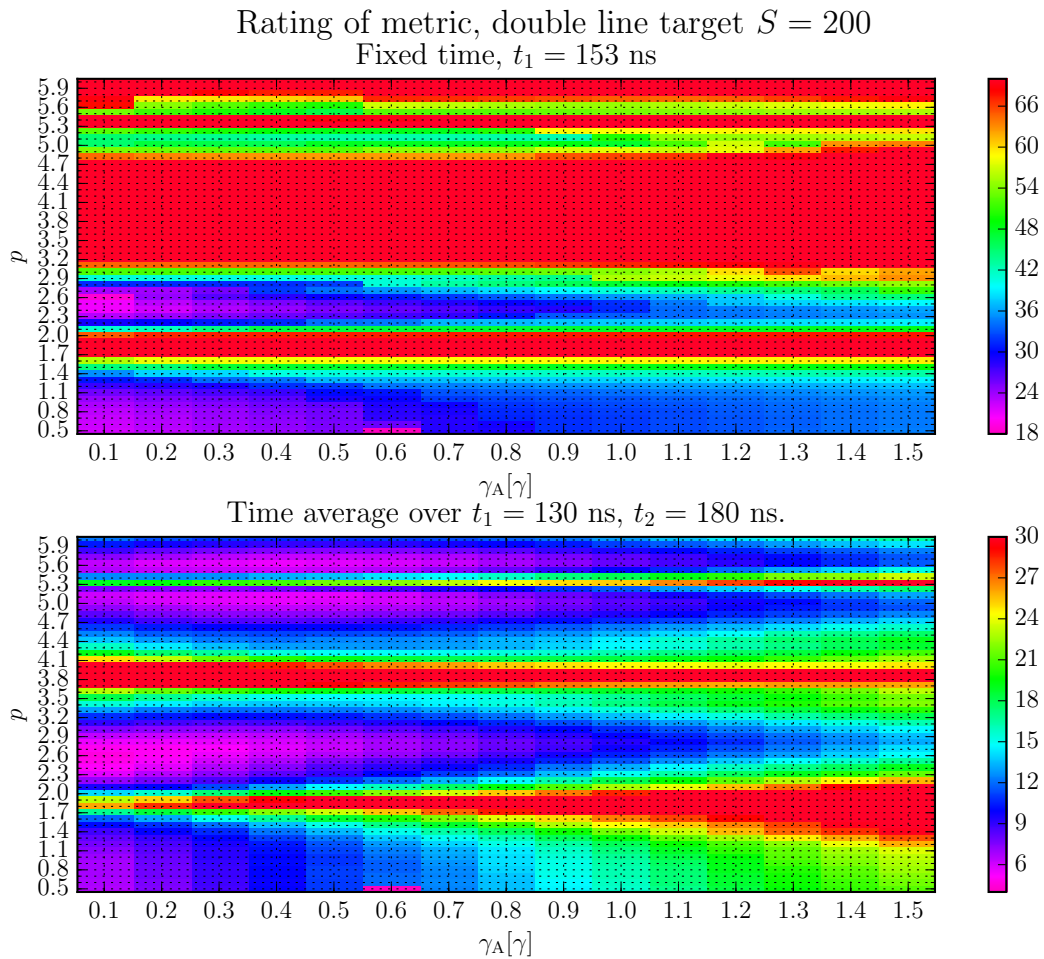


Figure 5.18.: Ratings of the metric for the complex phase of the double line target. One can see the same areas where the reconstruction is good than for the spectrum. However, the quality of reconstruction is more sensible to a change of p . If one averages over time, the areas of good reconstruction become larger.

6. Summary and Outlook

Summary

In this thesis, the Oscillation-drive, a new method to determine the energy spectrum and the complex spectral phase of an unknown target, which is irradiated by X-rays originating from a synchrotron source is developed theoretically. It is based on the exploitation of an additional phase, induced by mechanical motion, in the case of nuclear forward scattering.

The necessary background and the derivation of the most important formulas was done in chapter 2. First, the basic formula to describe the response function of the target to nuclear forward scattering has been derived. An important mechanism in the context of this thesis, the possibility to induce an additional phase to the response function, via mechanical motion of the target, was introduced subsequently. Further, two different motion pattern, an instantaneous phase jump and an oscillation of the target. Both pattern have contain a parameter φ_0 , which describes the additional phase at time $t = 0$, where the radiation hits the target. This parameter plays a central conceptual role for the theory of the Oscillation-drive.

The formula were firstly applied in chapter 3. In experiments using nuclear forward scattering, most measurements record the intensity of the radiation over time. Therefore, the influence of the additional phase in the case of two targets in a row, was examined. A special focus in this analysis was placed on the influence of φ_0 . The first result was, that the value of φ_0 can be used to control the position of minima which occur at the time spectra. Furthermore, it is known that φ_0 has an influence on the energy spectrum of a target. Consequently, the result of this examination was, that in combination with the new result, φ_0 can be used to control the response of the target simultaneously in the energy an in the time domain. Furthermore, the influence of φ_0 can be measured in time domain, which means, that it can provide a connection between the measured signal in the time domain and in frequency domain.

Motivated by this result, the influence of φ_0 in the energy domain is examined more thoroughly. The result of this was, that, for certain values, the real and the imaginary part of the energy spectrum are exchanged. This gives a hint, that it is possible to extract information about the phase by the variation of φ_0 .

This potential, offered by φ_0 to make a connection between the energy and the time domain, was investigated in chapter 4. It was used to develop a new method to determine the spectrum and the phase of a target in the energy domain.

The main principle is based on a already known method, which uses a foil mounted on a Doppler-drive as an analyzer. For the Oscillation-drive, the Doppler-drive was replaced by an oscillating piezo.

The main advantage of this is, that it is possible to use φ_0 to get more information about the target, than it is possible with the Doppler-drive. The reason for this is that φ_0 , which is provided by the oscillations, can be used as a additional and controllable degree of freedom. This resulted in the possibility to not only reconstruct the energy spectrum, but the spectral phase, too.

However, one disadvantage of the oscillation is, that it results in the creation of sidebands in the energy domain, which causes fast oscillations in the time domain. These oscillations cause difficulties for the reconstructions. To solve this problem, a method was developed to filter out the relevant part and set the unwanted perturbations to zero. This is done by using a Fourier transformation and the different frequencies of the relevant part and the perturbations. After applying this filter, the remaining part can be used to reconstruct the energy spectrum and the spectra complex phase of the target. To verify the theoretical results, a numerical simulation have been performed. The test with two different target, showed, that the reconstruction shows really good agreement with the original data.

In chapter number 5 an evaluation of the potential applicability and practical performance of the Oscillation-drive have been done. For this it was necessary to have a method, which gives a quantitative measure of the quality of the reconstruction. For the reconstruction of the spectrum, it is necessary, to average over a certain time interval. The quality of the reconstruction depends on the choice of this interval. Furthermore, dependent on this time interval, the reconstruction shows a better performance in the vicinity of the dip or at the edge of the spectrum. For this, three different metrics were developed, two of which focus on the edge or the dip of the target, respectively, and one does not discriminate between parts of the spectrum.

To determine the time interval for the average, two methods were developed. The first takes the value of a metric as a function of the time interval. This reduces the problem to a two dimensional optimization problem which was solved numerically. Using this, a parameter analysis have been performed in order to optimize parameters such as the linewidth of the analyzer or the oscillation amplitude of the piezo. The analysis was performed for the phase as well as for the spectrum. In this analysis, two parameter ranges were found, where the reconstructions work good and are robust within this range. The values of the parameter match with the predictions of the theory.

However, one disadvantage of the first algorithm to determine the average time interval is, that the original target has to be known in order to evaluate the metric. In an experiment, this would not be the possible. Therefore a second algorithm was implemented,

which uses the convergence at the edge of the energy spectrum to unity as a criteria. Furthermore, for targets with a known symmetry of the energy spectrum, this can be used as a criteria as well. Unfortunately, was found to show poor performance for one of the targets used to test the simulation. For the other the performance was not this good than the minimization algorithm, but it showed that it works in principal.

Next, the results of the reconstruction of the spectrum were compared with the corresponding Doppler drive results. The Doppler-drive performs equally well as than the Oscillation-drive, if a small linewidth for the analyzer is considered. If the linewidth increases, the results of the Doppler-drive become worse much faster than the one of the Oscillation-drive. Furthermore, a theory for the Doppler-Drive was developed, which uses the whole time range from 0 to ∞ , what is the maximum in informations which can be used. Therefore, this could be seen as the maximal possible resolution, which can be achieved using the Doppler-drive. The comparison with the Oscillation-drive showed the same behavior as for the realistic Doppler-drive: For a large linewidth of the analyzer, the Oscillation-drive performed better than the optimal Doppler-drive. Even though the difference between both methods was smaller than considering a restricted time interval for the Doppler-drive.

Moreover, the Oscillation-drive has an outstanding advantage compared to the Doppler-drive: it is able to reconstruct not only the energy spectrum of a target but in addition to that, the spectral phase of the target as well.

Outlook

In this thesis, a new method was presented to determine the energy spectrum as well as the spectral complex phase of a target. While the methods performance was tested for various realistic scenarios and compared to a standard method conventionally used in experiments, it has only been applied to simulated numerical examples so far. For a good practical performance, some further theoretical improvements to the method could be achieved in order to account for known experimental difficulties and boundary conditions. In the following, possible ways of improving the method in this direction are suggested. The upper time limit which was used for the simulation was taken to be 380 ns. This was chosen for the purpose of evaluating the principal possibilities of the method. However, the time intervall between two pulses at a synchrotron is normally shorter. At PETRA III, for example, it is 192 ns [58]. Therefore, it would be good to do the parameter analysis of chapter 5 again with the adjusted upper time limit and investigate possible adjustments for shorter acquisition times which hinder the access to late time spectral information. In this context, an other experimental effect have to be taken into account. Due to the short measuring period between two X-ray pulses of 192 ns, the effect occurs, that the detector measures a photon of the previous pulse in

the range of the current pulse. This effect can be taken into account, by mapping the signal at $t > 192$ ns to the range of 0 – 192 ns.

The quality of the reconstruction strongly depends on the time interval which is used to take the average over. To determine the optimal choice for this interval, an algorithm was developed, which optimizes this time interval, using the convergence of the spectrum at the edge, and if available the symmetry of the spectrum. This algorithm works in principal, however, to employ it experimentally, a further improvement is needed.

An interesting feature can be found in equation (4.58), which describes the connection between the offset of the fit a and the physical quantities. So far, it has been used to reconstruct $\hat{\theta}(S - \omega_p)$. For this, within the data the time has been fixed to t_0 , and ω_p is taken as variable. From this the phase $\hat{\theta}(S - \omega_p)$ can be reconstructed. However, it is possible to do the same, but fix the frequency to ω_p^0 and let the time vary. From the resulting dataset it is possible to reconstruct the phase of the target in the time domain, $\theta(t)$. This is very useful considering the following: The absolute value of the time spectrum of the target can be measured easily by irradiating the target on its own with X-rays. The measured signal is then proportional to the absolute square of the time spectrum.

This means, that it is possible now to measure the phase and the absolute value of the spectrum of a target in the time *and* in the energy domain.

This can be used now for a spin off project: Once the complex time and energy spectra are known it is possible to use them for consistency checks.

Using a numerical Fourier transformation it is possible to transform the time spectrum to energy domain or vice versa. By comparing the transformed and the measured spectrum, it is possible to check the consistency. If there are large deviations, one could adapt one of the spectra and do a back transformation. There the transformed, adapted spectrum is compared with the measured data, if necessary adapted and transformed back again, and so on. If this procedure is implemented using a intelligent, adaptive algorithm, this could be done several times until the back and forth transformations are consistent with each other and are optimized to deviate as little as possible from the measured data in time as well as in the energy domain. This would bring the importance of this method to a new level. By such an algorithm, a target could be characterized more precisely.

A. Additional plots to chapter 5

The essential results of chapter 5 could be described using only the plots of the single line target. However, to give the reader a better insight to the result, the plots for the double line target are given here.

Oscillation-drive In figure A.1, the ratings of the metrics for the case of optimized time intervals are plotted. The used target is the double line target.

In figure A.2, the ratings of the metrics for the case of fixed time intervals are plotted, the used target is the double line target. In both cases the structure is the same as for the single line target. However, by increasing γ_A , the ratings getting worse faster than for the single line target.

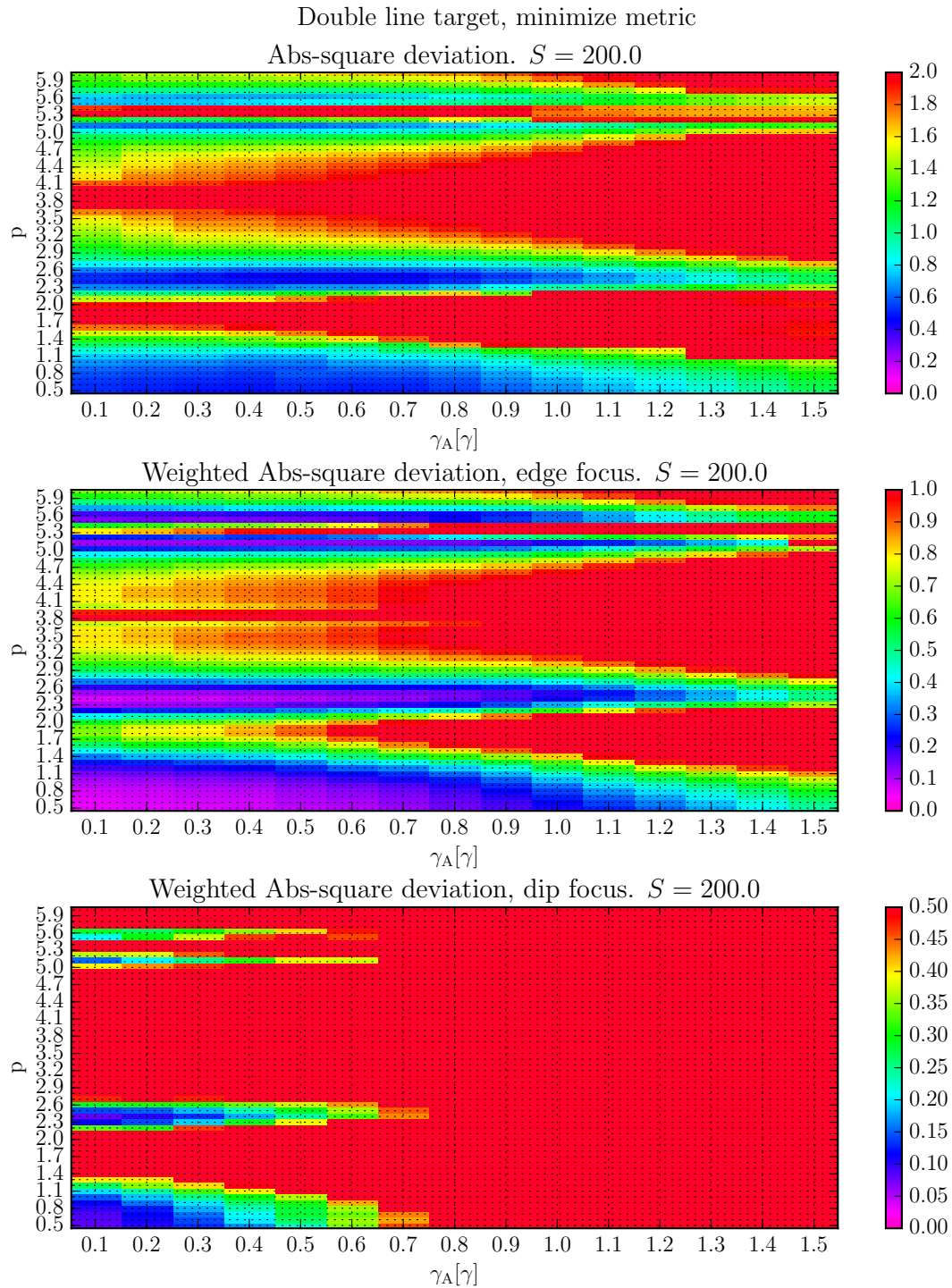


Figure A.1.: Rating of the different metrics for the double line target and optimized times to minimize the outcome of the metric. The higher the number, the worse the match with the original spectrum. γ_A has been fixed to $\gamma_A = 0.1$. The dependency on γ_A and p is clearly visible. For further discussion see in the main text.

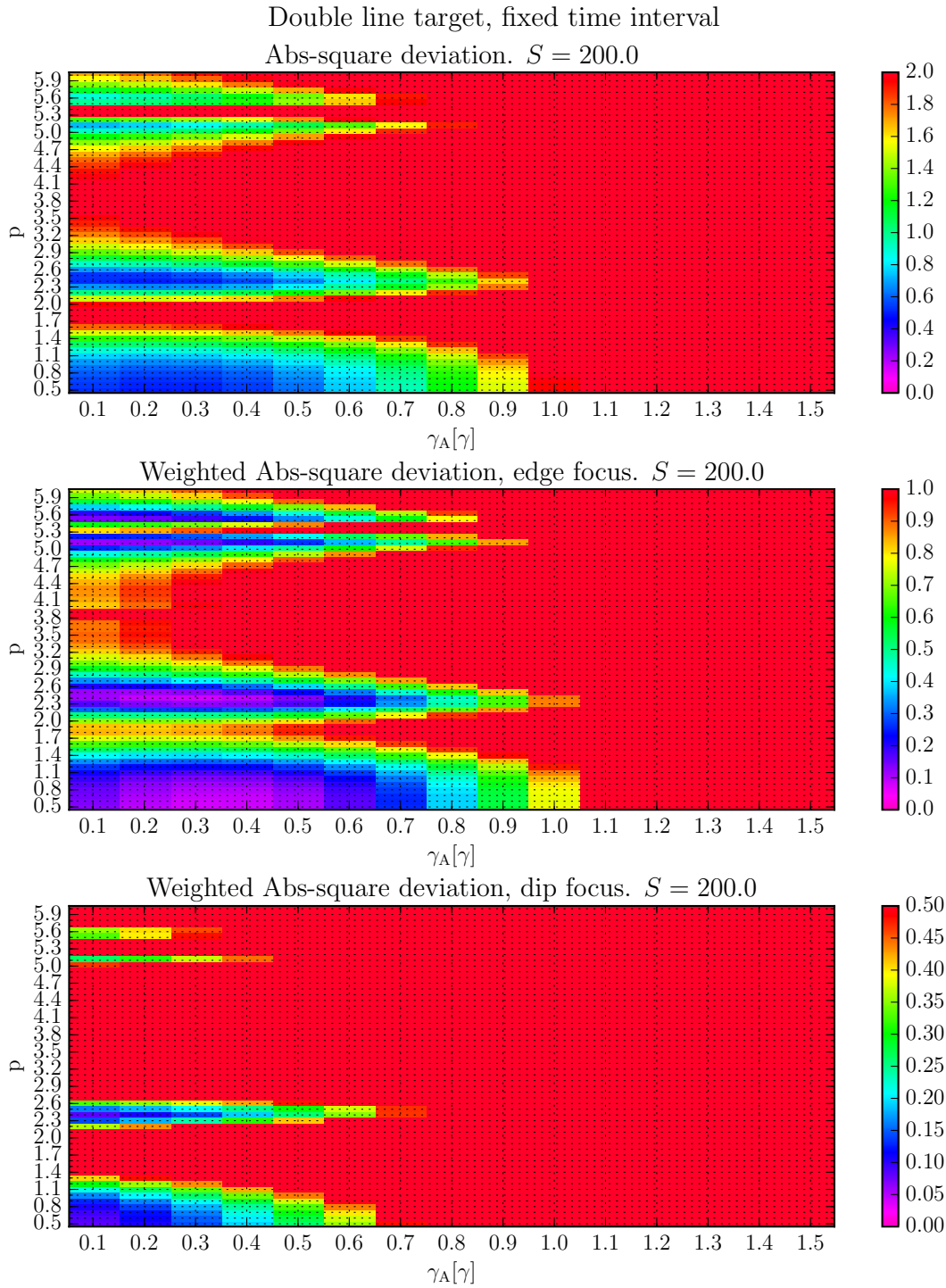


Figure A.2.: Rating of the different metrics for the double line target. For each metric, the average time interval is set to a fixed time interval. The higher the number, the worse the match with the original spectrum. S has been fixed to $S = 200$. Here, it is quite good visible that there are parameter ranges for which the reconstruction works good and other ones for which it is really bad. For further discussion see in the main text.

Bibliography

- [1] A. Einstein. Über einen die Erzeugung und Verwandlung des Lichtes betreffenden heuristischen Gesichtspunkt [AdP 17, 132 (1905)]. *Annalen der Physik* 14, 164–181 (2005).
- [2] Marlan O. Scully and M. Suhail Zubairy. *Quantum Optics*. Cambridge University Press (1997).
- [3] M. Orszag. *Quantum Optics: Including Noise Reduction, Trapped Ions, Quantum Trajectories, and Decoherence*. Springer International Publishing (2016).
- [4] P. Meystre and M. Sargent. *Elements of Quantum Optics*. Springer Berlin Heidelberg (2013).
- [5] Pierre Meystre and Murray Sargent. *Field Quantization*, pp. 299–325. Springer Berlin Heidelberg, Berlin, Heidelberg (2007).
- [6] K.-J. Boller, A. Imamoglu, and S. E. Harris. Observation of electromagnetically induced transparency. *Phys. Rev. Lett.* 66, 2593–2596 (1991).
- [7] Alessandro Zavatta, Silvia Viciani, and Marco Bellini. Quantum-to-Classical Transition with Single-Photon-Added Coherent States of Light. *Science* 306, 660–662 (2004).
- [8] R. Hanbury Brown and R. Q. Twiss. A Test of a New Type of Stellar Interferometer on Sirius. *Nature* 178, 1046–1048 (1956).
- [9] Giovanna Morigi, Jürgen Eschner, and Christoph H. Keitel. Ground State Laser Cooling Using Electromagnetically Induced Transparency. *Phys. Rev. Lett.* 85, 4458–4461 (2000).
- [10] Lisa Barsotti, Jan Harms, and Roman Schnabel. Squeezed vacuum states of light for gravitational wave detectors. *Reports on Progress in Physics* 82, 016905 (2018).
- [11] Donald H Bilderback, Pascal Elleaume, and Edgar Weckert. Review of third and next generation synchrotron light sources. *Journal of Physics B: Atomic, Molecular and Optical Physics* 38, S773–S797 (2005).
- [12] Rudolf Ruffer and Aleksandr I. Chumakov. Nuclear Resonance Beamline at ESRF. *Hyperfine Interactions* 97, 589–604 (1996).

- [13] Bernhard W. Adams, Christian Buth, Stefano M. Cavaletto, Jörg Evers, Zoltán Harman, Christoph H. Keitel, Adriana Pálffy, Antonio Picón, Ralf Röhlsberger, Yuri Rostovtsev, and Kenji Tamasaku. X-ray quantum optics. *Journal of Modern Optics* 60, 2–21 (2013).
- [14] Rudolf L. Mössbauer. Kernresonanzfluoreszenz von Gammastrahlung in Ir191. *Zeitschrift für Physik* 151, 124–143 (1958).
- [15] L. R. Walker, G. K. Wertheim, and V. Jaccarino. Interpretation of the Fe⁵⁷ Isomer Shift. *Phys. Rev. Lett.* 6, 98–101 (1961).
- [16] G. Shirane, D. E. Cox, and S. L. Ruby. Mössbauer Study of Isomer Shift, Quadrupole Interaction, and Hyperfine Field in Several Oxides Containing Fe⁵⁷. *Phys. Rev.* 125, 1158–1165 (1962).
- [17] H. J. Hay, J. P. Schiffer, T. E. Cranshaw, and P. A. Egelstaff. Measurement of the Red Shift in an Accelerated System Using the Mössbauer Effect in Fe⁵⁷. *Phys. Rev. Lett.* 4, 165–166 (1960).
- [18] R. V. Pound and G. A. Rebka. Gravitational Red-Shift in Nuclear Resonance. *Phys. Rev. Lett.* 3, 439–441 (1959).
- [19] Wen-Te Liao and Sven Ahrens. Gravitational and relativistic deflection of X-ray superradiance. *Nature Photonics* 9, 169 EP – (2015).
- [20] Yu. V. Shvyd’ko, T. Hertrich, U. van Bürck, E. Gerdau, O. Leupold, J. Metge, H. D. Rüter, S. Schwendy, G. V. Smirnov, W. Potzel, and P. Schindelmann. Storage of Nuclear Excitation Energy through Magnetic Switching. *Phys. Rev. Lett.* 77, 3232–3235 (1996).
- [21] Ralf Röhlsberger, Kai Schlage, Balaram Sahoo, Sebastien Couet, and Rudolf Ruffer. Collective Lamb Shift in Single-Photon Superradiance. *Science* 328, 1248–1251 (2010).
- [22] Ralf Röhlsberger, Hans-Christian Wille, Kai Schlage, and Balaram Sahoo. Electromagnetically induced transparency with resonant nuclei in a cavity. *Nature* 482, 199–203 (2012).
- [23] K. P. Heeg, C. Ott, D. Schumacher, H.-C. Wille, R. Röhlsberger, T. Pfeifer, and J. Evers. Interferometric phase detection at x-ray energies via Fano resonance control. *Phys. Rev. Lett.* 114, 207401 (2015).
- [24] Farit Vagizov, Vladimir Antonov, YV Radeonychev, RN Shakhmuratov, and Olga Kocharovskaya. Coherent control of the waveforms of recoilless γ -ray photons. *Nature* 508, 80 (2014).

-
- [25] K. P. Heeg, A. Kaldun, C. Strohm, P. Reiser, C. Ott, R. Subramanian, D. Lentrodt, J. Haber, H.-C. Wille, S. Goerttler, R. Ruffer, C. H. Keitel, R. Röhlsberger, T. Pfeifer, and J. Evers. Spectral narrowing of x-ray pulses for precision spectroscopy with nuclear resonances. *Science* 357, 375–378 (2017).
- [26] Vasily Potapkin, Aleksandr I. Chumakov, Gennadii V. Smirnov, Jean-Philippe Celse, Rudolf Ruffer, Catherine McCammon, and Leonid Dubrovinsky. The ^{57}Fe Synchrotron Mössbauer Source at the ESRF. *Journal of Synchrotron Radiation* 19, 559–569 (2012).
- [27] Werner Triftshäuser and Paul P. Craig. Time Dependence of Recoil-Free Resonance following Electron Capture in Co^{57} . *Phys. Rev.* 162, 274–285 (1967).
- [28] Ralf Röhlsberger. *General Aspects of Nuclear Resonant Scattering*, pp. 7–36. Springer Berlin Heidelberg, Berlin, Heidelberg (2004).
- [29] F. J. Lynch, R. E. Holland, and M. Hamermesh. Time Dependence of Resonantly Filtered Gamma Rays from Fe^{57} . *Phys. Rev.* 120, 513–520 (1960).
- [30] Samuel M. Harris. Quantum Mechanical Calculation of Mössbauer Transmission. *Phys. Rev.* 124, 1178–1185 (1961).
- [31] J. P. Hannon and G. T. Trammell. Mössbauer Diffraction. I. Quantum Theory of Gamma-Ray and X-Ray Optics. *Phys. Rev.* 169, 315–329 (1968).
- [32] J. P. Hannon and G. T. Trammell. Mössbauer Diffraction. II. Dynamical Theory of Mössbauer Optics. *Phys. Rev.* 186, 306–325 (1969).
- [33] Ralf Röhlsberger. *Coherent Elastic Nuclear Resonant Scattering*, pp. 67–180. Springer Berlin Heidelberg, Berlin, Heidelberg (2004).
- [34] W.t. Su, B. Li, D. q. Liu, and F. s. Zhang. The determination of infrared optical constants of rare earth fluorides by classical Lorentz oscillator model. *Journal of Physics D: Applied Physics* 40, 3343–3347 (2007).
- [35] Matthias Merz, Johannes Eisenmenger, Bernd Heinz, and Paul Ziemann. Tailoring optical properties of WO_3 films in the visible to infrared range by ion bombardment and its description by an oscillator model. *Phys. Rev. B* 66, 184102 (2002).
- [36] Yifu Zhu, Daniel J. Gauthier, S. E. Morin, Qilin Wu, H. J. Carmichael, and T. W. Mossberg. Vacuum Rabi splitting as a feature of linear-dispersion theory: Analysis and experimental observations. *Phys. Rev. Lett.* 64, 2499–2502 (1990).
- [37] Bahaa Saleh and Malvin Teich. *Fundamentals of Photonics, 2nd Edition* (2006).
- [38] Wolfgang Demtröder. *Elektromagnetische Wellen in Materie*, pp. 219–259. Springer Berlin Heidelberg, Berlin, Heidelberg (2013).

- [39] E. Zeidler, W. Hackbusch, J. Hromkovic, B. Luderer, H.R. Schwarz, J. Blath, A. Schied, S. Dempe, G. Wanka, and S. Gottwald. *Springer-Taschenbuch der Mathematik: Begründet von I.N. Bronstein und K.A. Semendjaew Weitergeführt von G. Grosche, V. Ziegler und D. Ziegler Herausgegeben von E. Zeidler*. SpringerLink : Bücher. Springer Fachmedien Wiesbaden (2012).
- [40] *Elektrodynamik*, pp. 199–368. Springer Berlin Heidelberg, Berlin, Heidelberg (2004).
- [41] Melvin Lax. Multiple Scattering of Waves. *Rev. Mod. Phys.* 23, 287–310 (1951).
- [42] Hermann Haken and Hans Christoph Wolf. *Atome im Magnetfeld, Experimente und deren halbklassische Beschreibung*, pp. 189–204. Springer Berlin Heidelberg, Berlin, Heidelberg (1983).
- [43] J. P. Hannon, G. T. Trammell, M. Blume, and Doon Gibbs. X-Ray Resonance Exchange Scattering. *Phys. Rev. Lett.* 61, 1245–1248 (1988).
- [44] Ralf Röhlsberger, Hans-Christian Wille, Kai Schlage, and Balaram Sahoo. Electromagnetically induced transparency with resonant nuclei in a cavity. *Nature* 482, 199–203 (2012).
- [45] Kilian P. Heeg. *X-Ray Quantum Optics With Mössbauer Nuclei In Thin-Film Cavities*. Dissertation, University of Heidelberg (2014).
- [46] Peter Furlan. *Gelbes Rechenbuch 3*. Verlag Martina Furlan, Dortmund (2010).
- [47] R. N. Shakhmuratov, F. Vagizov, and O. Kocharovskaya. Radiation burst from a single γ -photon field. *Phys. Rev. A* 84, 043820 (2011).
- [48] G.V. Smirnov and W. Potzel. Perturbation of nuclear excitons by ultrasound. *Hyperfine Interactions* 123, 633–663 (1999).
- [49] P. Schindermann, U. van Bürck, W. Potzel, G. V. Smirnov, S. L. Popov, E. Gerdau, Yu. V. Shvyd’ko, J. Jäschke, H. D. Rüter, A. I. Chumakov, and R. Ruffer. Radiative decoupling and coupling of nuclear oscillators by stepwise Doppler-energy shifts. *Phys. Rev. A* 65, 023804 (2002).
- [50] G. V. Smirnov, U. van Bürck, J. Arthur, S. L. Popov, A. Q. R. Baron, A. I. Chumakov, S. L. Ruby, W. Potzel, and G. S. Brown. Nuclear Exciton Echo Produced by Ultrasound in Forward Scattering of Synchrotron Radiation. *Phys. Rev. Lett.* 77, 183–186 (1996).
- [51] Patrick Reiser. *Time Domain Control of X-Ray Quantum Dynamics*. Masterthesis, University of Heidelberg (2014).

-
- [52] DESY. P01 Nuclear Resonant Scattering at DESY. http://photon-science.desy.de/facilities/petra_iii/beamlines/p01_dynamics/nuclear_resonant_scattering_station/index_eng.html (2019). [Online; accessed 11-October-2019].
- [53] Ralf Röhlsberger. *Methods and Instrumentation*, pp. 37–65. Springer Berlin Heidelberg, Berlin, Heidelberg (2004).
- [54] G.V. Smirnov and W. Potzel. Perturbation of nuclear excitons by ultrasound. *Hyperfine Interactions* 123, 633–663 (1999).
- [55] J.P. Hannon and G.T. Trammell. Coherent γ -ray optics. *Hyperfine Interactions* 123, 127–274 (1999).
- [56] Kilian P. Heeg, Hans-Christian Wille, Kai Schlage, Tatyana Guryeva, Daniel Schumacher, Ingo Uschmann, Kai S. Schulze, Berit Marx, Tino Kämpfer, Gerhard G. Paulus, Ralf Röhlsberger, and Jörg Evers. Vacuum-Assisted Generation and Control of Atomic Coherences at X-Ray Energies. *Phys. Rev. Lett.* 111, 073601 (2013).
- [57] A. V. Oppenheim and J. S. Lim. The importance of phase in signals. *Proceedings of the IEEE* 69, 529–541 (1981).
- [58] DESY. Machine Parameters PETRA III. http://photon-science.desy.de/facilities/petra_iii/machine/parameters/index_eng.html (2019). [Online; accessed 30-October-2019].
- [59] Ralf Röhlsberger. The collective Lamb shift in nuclear γ -ray superradiance. *Journal of Modern Optics* 57, 1979–1992 (2010).
- [60] Wolfgang Demtröder. *Mechanische Schwingungen und Wellen*, pp. 325–384. Springer Berlin Heidelberg, Berlin, Heidelberg (2013).

Acknowledgment

Als erstes geht mein Dank an Jörg Evers, der mich bei dieser Masterarbeit betreut hat. Danke für die vielen Diskussionen und die vielen Nachfragen, die immer dazu beigetragen haben, dass noch offene Punkte aufkamen und sich das Verständnis bei schon verstandenen Problemen vertiefen konnte.

Ein weitere Dank geht an Prof. Keitel, in dessen Abteilung diese Arbeit zustande kam und es mir ermöglichte an der DPG-Tagung sowie an einer Beamtime in Hamburg dabei zu sein.

Ein herzlicher Dank geht an meine Kollegen in der Arbeitsgruppe, Dominik Lentrodt, Kilian Heeg und Miriam Gerharz. Danke euch, für die entspannte Atmosphäre im Büro, bei der DPG oder bei der Beamtime.

Ein großes Dankeschön geht noch an meinen Bruder Clemens, sowie an Dominik, die große Teile der Arbeit gelesen und mir mit vielen ausführlichen Kommentaren und Anmerkungen zurück gegeben haben und mir so wertvolle Hinweise für die Ausformulierung der Arbeit lieferten.

Zuletzt ein großes Danke von Herzen an Kerstin. Danke für deine Geduld mit mir, danke für deine ständige Unterstützung, danke fürs an mich glauben, danke für die viele kleine Zettel und Briefchen. Danke fürs zurückstecken und für mich da sein!

Erklärung

Ich versichere,

- dass ich diese Arbeit selbständig verfasst habe,
- dass ich keine anderen als die angegebenen Quellen und Hilfsmitteln benutzt habe

Heidelberg, den 15th of November 2019

Benedikt Herkommer